Fall 12-17-2011

Investigating the Thermal Stability and Cation Ordering in Layered Cathode LixMO2 (x ≤ 1; M = Co, Mn, Ni) Materials for Li-ion Rechargeable Batteries and Studying the Ferroelectric Properties of LiNbO3 Nanoparticles

Debasish Mohanty
University of New Orleans

Investigating the Thermal Stability and Cation Ordering in Layered Cathode Li_xMO_2 ($x \leq 1$; M = Co, Mn, Ni) Materials for Li-ion Rechargeable Batteries and Studying the Ferroelectric Properties of $LiNbO_3$ Nanoparticles

A Dissertation

Submitted to the Graduate Faculty of the
University of New Orleans
in partial fulfillment of the
requirements for the degree of

Doctor of Philosophy
in
Chemistry

By

Debasish Mohanty

B.S., Berhampur University, 2002
M.S., Berhampur University, 2005
M.S., University of New Orleans, 2011

December, 2011

Dedicated to My Parents...

Acknowledgments

This is to express my gratitude to all of them whom I consider truly responsible for the completion of my PhD research project. It would not have been possible without the support of many people.

I want to express my deepest gratitude to my advisor, Prof. John B. Wiley who was extravagantly helpful and offered me invaluable assistance, support and guidance, and constant encouragement. He has really been an excellent advisor; I thank him for sharing his experience in scientific knowledge, and human values. Thank you also for your patience, your "pep talks", and for always having time whenever I needed you for a conversation. His insightful research discussions have always motivated me in my research. He is “the best” advisor one can have in his/her research career.

Sincere gratitude is also for my previous research advisor, Dr. Heike B. Gabrisch for her constant support and teaching. Dr. Heike’s enthusiasm and insights were constant inspirations during my course of study.

I want to thank my supervisory committee, Dr. Gabriel Caruntu, Dr. Ferdinand Poudeu, Dr. David Mobley, and Dr. Leszek Malkinski for their suggestion during my research. Without whose knowledge and assistance this study would not have been successful.

The financial support by the Department of Defense through DARPA (Grant HR 0011-09-1-0047) and Louisiana Board of Regents, Grant No. LEQSF (2007012)-ENH-PKSFI-PRS-04, and College of Science, University of New Orleans are also gratefully acknowledged.

I want to thank Amin and Shiva from Dr. Caruntu’s group for their immense help and valuable time for collecting Piezoresponse force microscopy data and Raman data respectively.

Special thanks to all of my present group members; “Girija ji”, Jin-Hee, Elisha, Jianxia, Yuan, Dariush, Piku, Léa, Stephan, Aisa, and previous group members; “CJ” and Sanjaya for sharing the literature and invaluable assistance during my study. I also thank you all for being there always with me during my good and bad times. You guys are the best friends who always have been there to be my support and also to share my feelings.

I want to thank Dr. Baobao Cao for helping me with the technical things in Transmission Electron Microscopy and for the fun times at work.

I am sincerely grateful to “Srinu Sir”, Prof. R.K. Panda, and Dr. Bidhu Bhusan Das for introducing me to the world of Chemistry, teaching me the “symbols and formulae” in Chemistry, and motivating me to take “Chemistry” as major in my career.

I want to thank my Parents “Bapabou” for their blessings, motivation, moral support, and endless love throughout my life, and showing me the right direction. I also want to thank my brother “Sibun”, sister “Mamun” for their constant love and support which helps me believe more in myself. I want to thank each of my family members for their belief in me. My sincere thank goes to my in-laws parents “Babamaa”, for their encouragement throughout the duration of my PhD studies. Special thanks to my brother-in law; “Ravi Bhaya”, sister in-law “Bhavna Didi”, and “Siwani Didi” for their best wishes, and support in my life. Finally yet, importantly, I want to thank my beloved wife Gayatri from the bottom of my heart for her love, patience, dedication, rays of sunshine and the motivation she has given me throughout my PhD studies.

Table of Contents

List of Tables

List of Figures

Abstract

In recent years, transition metal oxides have drawn extensive attention because of their wide application in electronic, memory, battery, informatics, and optoelectronics devices. In this dissertation, we have studied two different types of oxide materials which are technologically important: $LiMO_2$ (M = Co, Mn, Ni), has served as cathode materials in the rechargeable battery, and $LiNbO_3$, has wide application in ferroelectric devices such as electronics, non-volatile memories, and thin film capacitors. $LiMO_2$ was synthesized and characterized to understand the correlation between capacity fading and thermal stability relating to the microstructures. Our results showed that delithiated (charged) $LiCoO_2$, forms a metastable $LiCo_2O_4$ spinel phase during the ageing process, and eventually decomposes to Co_3O_4 over time. These two phases were identified from their magnetic responses. Paramagnetic behavior is observed in the starting material without indication of any magnetic ordering prior to heat treatment. Heat treatment of delithiated materials progressively changes the magnetic nature of the compounds. After short term heat treatment of delithiated $LiCoO_2$, spin-glass-like or geometrically frustrated behavior is observed that suggests the formation of metastable spinel phase $LiCo_2O_4$ in the lattice. After long-term annealing, pronounced strong antiferromagnetic (AFM) ordering is observed consistent with the formation of Co_3O_4. The thermal stability of $LiCoO_2$ was compared with $LiMn_{1/3}Ni_{1/3}Co_{1/3}O_2$. The result showed that, unlike $LiCoO_2$, $LiMn_{1/3}Ni_{1/3}Co_{1/3}O_2$ does not decompose. However, selected area electron diffraction (SAED) and the bright field images from transmission electron microscopy studies revealed significant microstructure changes in the delithiated material and thermally aged products. In another system, $Li[Ni_{1-x}Mn_x]O_2$ (x = 0.3, 0.5, 0.7), the cation ordering was successfully monitored to understand the Li/Ni disorder for

different compositions. This eventually determines the electrochemical capacity of these cathodes. The results on the starting materials revealed that the manganese-rich composition has more Li/Ni disorder compared to the other compositions. The Li/Ni disorder was detected by powder X-ray Diffraction, magnetic studies, as well as SAED studies. From the SAED studies, it was found that Li/Ni disorder creates $\sqrt{3}$ x $\sqrt{3}$ R30º type cation ordering in the transition metal layers. For delithiated materials this ordering was found to be suppressed indicating that the extraction of lithium occurs from the transition metal layer rather from the lithium layer.

In another study, the ferroelectric properties of $LiNbO_3$ nanoparticles were studied as a function of shape. By employing a solvothermal method, cube- and sphere-like ferroelectric $LiNbO_3$ nanoparticles were prepared by decomposition of the single-source precursor, $LiNb(O\text{-}Et)_6$, in the absence of surfactants. X -ray diffraction showed that the $LiNbO_3$ nanoparticles were rhombohedral (*R*3*c*) with a = 5.145(3) Å, c = 13.867(3) Å for nanocubes and a = 5.139(3) Å, c = 13.855(3) Å for nanospheres. Ferroelectric properties for these nanoparticles were also confirmed by piezoresponse force microscopy (PFM) and Raman spectroscopy. From PFM measurements, it was observed that both sets of particles exhibited polarization switching at room temperature with static d_{33} coefficient values of 17 pm/V for cube-like and 12 pm/V for spherical LN nanoparticles.

Chapter 1
Introduction and background

1.1 Lithium ion rechargeable batteries

Rechargeable lithium-ion batteries (LIBs) are essential power sources for consumer electronic devices such as cellular telephones, digital cameras, camcorders, and laptop computers [1]. Because of their high energy density, relative low weight, and high capacity, lithium batteries are also being used in energy storage devices for electric and hybrid electric vehicles (HEVs), electric vehicles (EVs), biomedicine, and space [1-3]. Mankind's total power consumption is currently 14 TW and is projected to roughly triple by 2050 [4, 5]. At present, oil represents 34% of the world's total primary energy source. It accounts for 40% of the total CO_2 emission and is a major cause of geopolitical instability. Since the majority of oil is used for automobile applications, a transition to an electrified road transportation system should be a prominent replacement [6]. The invention of hybrid Evs has been significant, and this will be accelerated as plug-in hybrid vehicles are converted to pure EVs [2.6]. A major technical hurdle for the complete electrification of road transportation is the insufficient storage capacity of current batteries, severely limiting the range of practical EVs. It has been found that, the EVs can reduce the daily consumption of gasoline by one fourth, which eventually will reduce the United State's dependency on the foreign oil to a greater extent [6]. Due to the high storage capacity, LIBs are the perfect candidate to be used in HEVs and EVs. Despite their success, lithium ion batteries are still under investigation with the aim to improve safety, increasing the energy density and life span while reducing costs [7]. Designing batteries with higher specific energy, higher capacity, and longer lifetime requires deeper understanding of the relationship between materials properties and performance in an electrochemical cell. The working principle of Li-ion

batteries involves Li ions extraction from and insertion into intercalation compounds at both electrodes [1, 2]. The layered $LiMO_2$ (M = transition metal ions) is the current leading cathode material although there are other cathode materials being used for LIBs, such as $LiFePO_4$ (olivine structure) [8]. Additionally graphitic carbon, for an example, is the material of choice for the anode. After a certain number of charge discharge cycles the layered structure of the cathode material is ($LiMO_2$) compromised, which prevents the movement of Li ions [9]. In the charge-discharge cycles, there is always a possibility of degradation of the cathode material in a variety of ways, such as fracture on the material surfaces, and significant microstructure changes. These structural instabilities decrease the capacity of the electrode and thereby limit the lifetime of the battery. With respect to battery safety, chemical processes that produce heat or result in irreversible phase transformations are important and need to be well studied. These problems need to be completely resolved in order to have a high energy density, greater safety, and longer life span for LIBs application in HEVs and EVs. Therefore, a better understanding of structure-property-relationships within cathode materials is critical to improve the properties of rechargeable batteries.

1.2 Working principle of LIBs

LIBs are the electrochemical power sources that convert chemical energy into electrical energy. These are secondary cells or accumulators, which are rechargeable several times, unlike the single-use primary cells [1]. The characteristic feature of an electrochemical cell is its use for generating electric current. This current is the movement of electrons in the external circuit, which is generated by the electrochemical processes at the two different electrodes, cathodes and anodes. In addition to the electronic current, the charge is transported between the positive and negative electrode by ions. A schematic showing the working unit of LIBs is given in Figure 1.1.

Typically the smallest working unit in a battery is the electrochemical cell, consisting of a cathode and an anode separated by an electrolyte and a separator. The electrolyte conducts ions but is an insulator to electrons. The cathode is generally a metal oxide $LiMO_2$ (where M = Co, Mn, Ni) and the anode is graphite. In the charged state, the anode contains a high concentration of intercalated lithium ions while the cathode is depleted of lithium. In an alternative way, when the LIB is charged by using an external current source, the lithium ions present in the $LiMO_2$ cathode move to the anode by diffusing thru the electrolyte. This makes the $LiMO_2$ cathode lithium deficient and anode as lithium rich. This process is also called as delithiation [1, 2, 10] since lithium is extracted from the cathode. At cathode, the chemical reaction can be written as:

$$LiMO_2 \rightarrow Li_{1-x}MO_2 + x\,Li^+ + x\,e^- \,(x < 1)$$

During the discharge, lithium ions leave the anode and migrate through the electrolyte to the $LiMO_2$ cathode, while its associated electron is collected by the current collector to power an electric device. This process is called lithiation [1, 2, 10] since the cathode gains lithium ions. The chemical reaction at the anode during discharging can be written as:

$$LiC_6 \rightarrow Li^+ + e^- + C_6$$

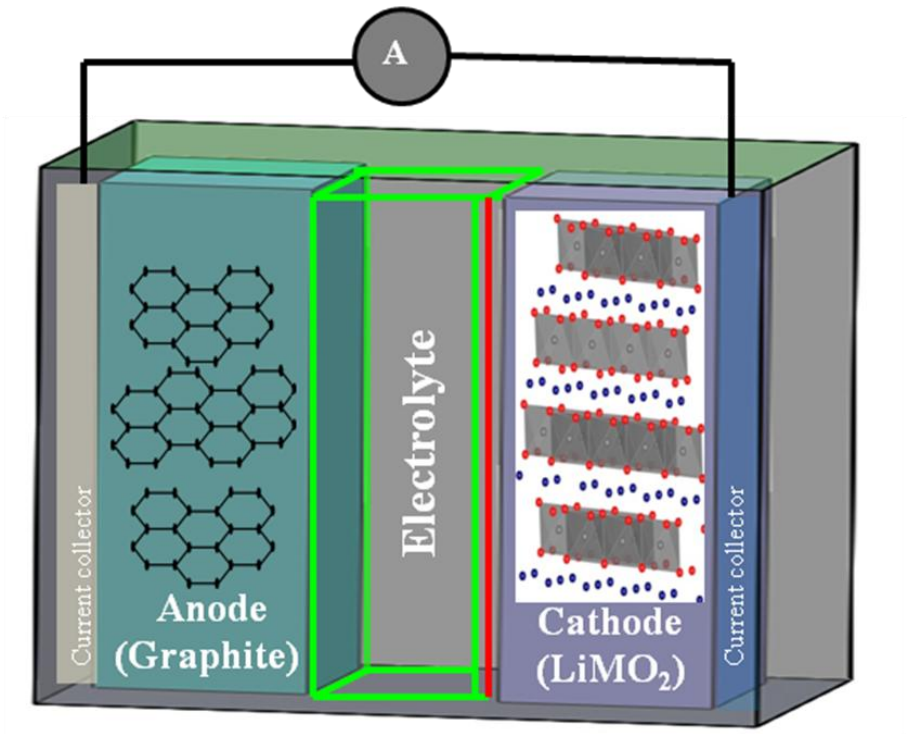

Figure 1.1 Schematic of a state-of-the art lithium ion battery (the separator, shown as a red line, separates metal oxide cathodes and graphite anode).

1.3 Cathodes for LIBs

Cathode materials for LIBs include lithium-metal oxides such as $LiCoO_2$, $LiMn_2O_4$, and $Li(Ni_xMn_yCo_z)O_2$, vanadium oxides, olivines such as $LiFePO_4$. Layered oxides containing cobalt and nickel are the most studied materials for lithium-ion batteries. They show a high stability in the high-voltage range, but cobalt has limited availability in nature and is toxic, which is a tremendous drawback for mass manufacturing. Manganese offers a low-cost substitution with a high thermal threshold and excellent rate capabilities but limited cycling behavior because of the dissolution of manganese during charge discharge processes. Therefore, mixtures of cobalt, nickel, and manganese are often used to combine the best properties and minimize the drawbacks. Vanadium oxides have a large capacity and excellent kinetics, however, due to lithium insertion and extraction, the material tends to become amorphous, which limits the

cycling behavior. Olivines are nontoxic and have a moderate capacity with low fade due to cycling, but their conductivity is low.

Since layered cathode materials ($LiMO_2$) are the more promising cathode materials for LIBs, our research has focused on this particular type cathode material. Cathode materials are an important aspect of battery research, since 50% of the production cost for a lithium ion cell depends on the cathode material processing (see Figure 1.2) [6]. The cathode materials under investigation include $LiCoO_2$, binary compounds in the system $LiNiO_2$-$LiMnO_2$ [$LiNi_{1-x}Mn_xO_2$ (x= 0.3, 0.5, 0.7)] and ternary $LiMn_{1/3}Ni_{1/3}Co_{1/3}O_2$. In the following section we will describe the crystal structures of these three different types of cathode materials.

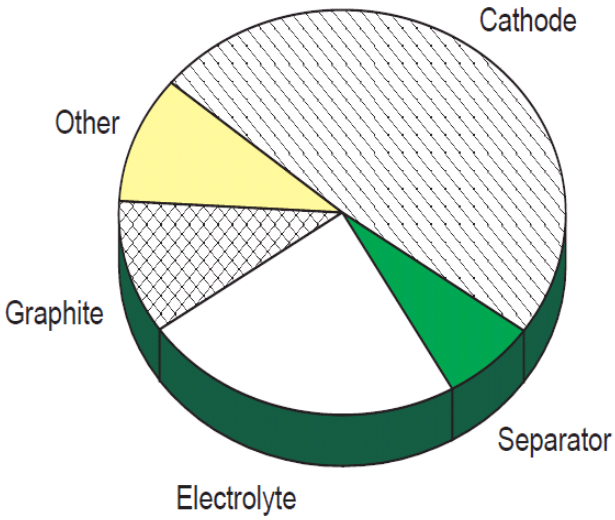

Figure 1.2 Pie chart of the battery manufacture cost

1.3.1 $LiCoO_2$ as a cathode material

$LiCoO_2$ is the most used active cathode material for commercial lithium ion batteries. It has been first suggested as intercalation compound for rechargeable Li-ion batteries by Mizushima *et al*. [11, 12]. Depending on synthesis temperature, two crystallographic forms of $LiCoO_2$ are observed: at low temperatures around 350 °C a cubic spinel structure is formed that converts to a trigonal layered lattice around 750 °C (space group 166, $R\bar{3}m$ also called hexagonal form). The layered lattice shows better electrochemical performance compared to the material with the cubic spinel lattice. The crystal structure of layered $LiCoO_2$ is similar to the α-$NaFeO_2$ type structure which can be described by space group $R\bar{3}m$ with lithium and cobalt ions in octahedral 3a and 3b sites respectively, separated by layers of cubic close packed oxygen ions [13]. The unit cell of the layered form consists of three slabs of edge sharing CoO_6 octahedra separated by interstitial layers of Li (Figure 1.3). The unit cell of $LiCoO_2$ is hexagonal and the phase is called the O3 phase. The O3 phase represents; the alkali metal ion which is Li resides in the octahedral interstitial sites and there is …ABC…ABC… stacking arrangement of the layers. This arrangement is shown in the Figure 1.4.

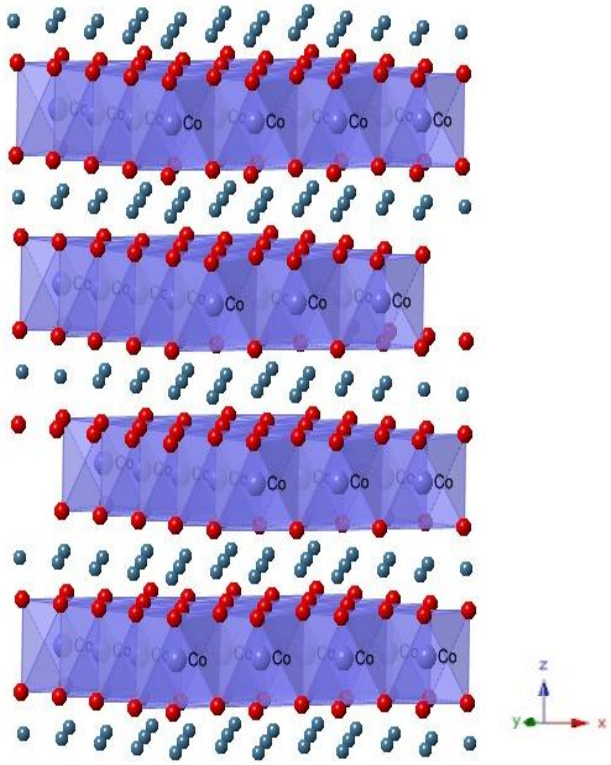

Figure 1.3 Crystal structure of $LiCoO_2$ where lithium ions (indigo spheres) are present in between CoO_6 octahedra.

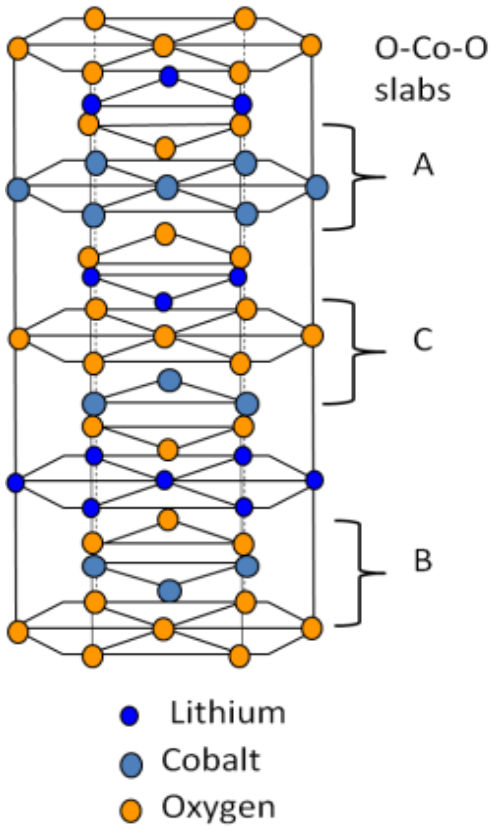

Figure 1.4 ABC arrangements in the $LiCoO_2$ hexagonal unit cell.

In the fully lithiated state $LiCoO_2$ remains in layered structures with hexagonal unit cell. With removal of Li from the layered crystal lattice (during charging) nonstoichiometric $Li_{1-x}CoO_2$ compounds are formed that take on different crystallographic structures depending on Li-content. After 50% of lithium removed from the parent structure the structure changes from hexagonal to monoclinic [14]. This reduces the experimental electrochemical capacity (maximum achievable is 140 mAh/g) of $LiCoO_2$ compared to the theoretical capacity (280 mAh/g). Structural considerations limit the amount of Li removed from the hexagonal lattice to 0.5, which in turn limits the achievable capacity to 140 mA/g compared to the theoretical capacity of 270 mAh/g.

Despite this drawback, $LiCoO_2$ has still been considered one of the most promising cathode materials for LIBs.

1.3.2 $LiCo_{0.33}Mn_{0.33}Ni_{0.33}O_2$ as a cathode material

Over the last few years the ternary transition metal oxide $LiNi_{1/3}Mn_{1/3}Co_{1/3}O_2$ has developed into a strong candidate for applications in high power rechargeable LIBs, due to its superior thermal stability and reversible capacity compared to its $LiCoO_2$ counterpart [15, 16, 17]. It has a high reversible capacity of 160 mAh/g in the cut-off voltage range of 2.5-4.4V and 200 mAh/g in 2.8-4.6V which makes this material a very promising cathode for high power and high energy Li-ion batteries to be used in HEVs [18]. $LiNi_{1/3}Mn_{1/3}Co_{1/3}O_2$ is iso-structural to $LiCoO_2$. It crystallizes in $R\bar{3}m$ space group with lithium ions in the 3a site and Co, Mn and Ni in the 3b sites. The unit cell is hexagonal with lithium ions present in between the octahedra of the transition metal ions (Figure 1.5). Since in $LiNi_{1/3}Mn_{1/3}Co_{1/3}O_2$ there are three transition metal ions in the transition metal layers in contrast to the single transition metal ion of $LiCoO_2$, cation ordering among the transition metal ions can cause changes in the parent structure of $LiNi_{1/3}Mn_{1/3}Co_{1/3}O_2$ [19]. This ordering happens when there is an interchange between Li^+ and Ni^{+2} in between their respective crystallographic sites. Since the radius of Li^+ is very similar to that of Ni^{+2} there is always a chance of Li^+/Ni^{+2} interchange [20]. This is also termed as Li/Ni disorder. This disorder always decreases electrochemical activity and opens up the possibility of different cation orderings. This cation ordering can be visible as superstructures in X-ray diffraction and in selected area electron diffraction patterns. The crystal and the electronic structures of $LiNi_{1/3}Mn_{1/3}Co_{1/3}O_2$ have been investigated by theoretical and experimental methods in order to understand the formation of superstructures. One of the most well studied superstructures is $\sqrt{3}$ x $\sqrt{3}$ $R30^o$ in plane ordering. Experimental evidence for in-plane ordering

has been observed by Yabuuchi *et al*, [18] who reported superlattice reflections in the pristine material corresponding to $\sqrt{3}$ x $\sqrt{3}$ R30^{o} in plane unit cell with a P3$_1$12 space group. This ordering can be seen when one cation is surrounded by two other cations in the transition metal layers. In this case the Co, Ni, Mn cations are a $\sqrt{3}a_{hex}$ distance from each other. This ordering decreases the electrochemical activity since the diffusion of Li ions occurs easily.

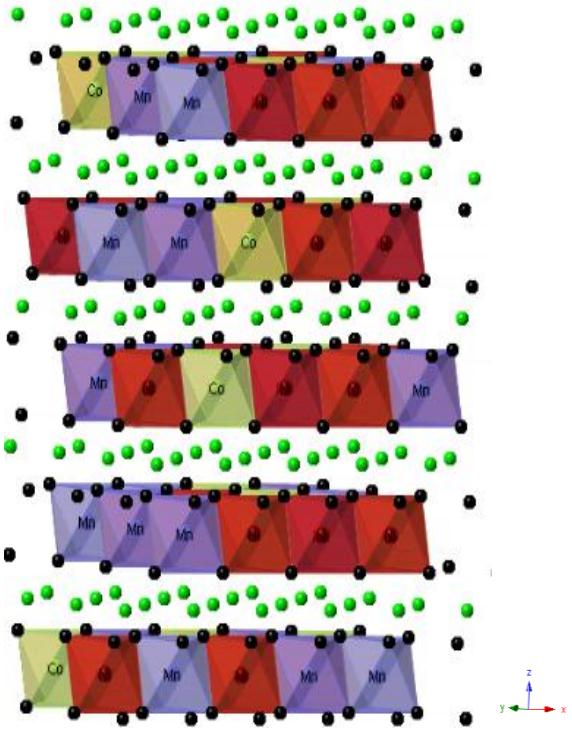

Figure 1.5 Crystal structure of $LiCo_{1/3}Mn_{1/3}Ni_{1/3}O_2$ where lithium ions (green) are present in the layers of octahedra of transition metal ions (Co, Mn, Ni are randomly oriented)

1.3.3 $LiNi_{1-x}Mn_xO_2$ as a cathode material

Over the past few years layered lithium-insertion cathode materials have been investigated to find alternatives to $LiCoO_2$ in order to compensate for its structural instability in

the extensively charged state ($Li_{1-x}CoO_2$; $x \geq 0.5$) [21-23]. Layered $LiNiO_2$, which is isostructural with $LiCoO_2$, was investigated as possible replacement. Although $LiNiO_2$ is cheaper than $LiCoO_2$ and has high rechargeable capacity, it is difficult to reproduce $LiNiO_2$ batches with the ideal $R\bar{3}m$ layered structure. In this material the presence of Li ions in the TM layers lowers the electrochemical activity of the cathode material and its poor thermal stability in the charged state prohibits its practical use [24]. It has been seen that doping of manganese ions in the parent $LiNiO_2$ structure dramatically increases the thermal stability of cathode material in the composition $LiNi_{1-x}Mn_xO_2$ ($x = 0.5$). The $LiNi_{0.5}Mn_{0.5}O_2$ is a promising, inexpensive and nontoxic alternative to $LiCoO_2$ and $LiNiO_2$. This material forms a solid solution between $LiNiO_2$ and $LiMnO_2$ to produce an ideal layered structure when the ratio between Ni and Mn is exactly 1:1. The layered compound adopts the α-$NaFeO_2$ structure with space group $R\bar{3}m$. In this lattice where Li ions resides in the 3a position and transition metal ions present at 3b sites in a random order with cubic closed packed oxygen layers [25]. First principle calculations and X-ray absorption near-edge fine structure (XANES) results on $LiNi_{0.5}Mn_{0.5}O_2$ shows that Ni ion is in +2 state, which is electrochemically active ion, and Mn ion remains +4 during the whole electrochemical reaction and this contributes to the stability of this compound [26]. However due to very similar ionic radius of Ni^{+2} and Li^+ ions there is always possibility of interchanging of nickel and lithium ions between their crystallographic sites. The exchange of lithium ions with the transition metal ions in the trigonal lattice creates two distinct crystallographic α and β site, leading to the a $\sqrt{3}a_{hex}$ x $\sqrt{3}a_{hex}$ supercell [27, 28]. This introduces long range in-plane ordering among the transition metal ions in the transition metal layers. The evidence of this ordering was reported from electron diffraction analysis and can be categorized in two types. Those are in the hexagonal ($\sqrt{3}a_{hex}$ x $\sqrt{3}a_{hex}$ R30° type ordering) and monoclinic unit cell (C2/m ordering). Long

range order within the TM layer can be observed when 2 or more species are present. In the case of Li_2MnO_3 ($Li[Li_{1/3}Mn_{2/3}]O_2$), a honeycomb structure is formed that has been described in literature as C2/m. Here superlattice reflections divide the distance between fundamental reflections into three, corresponding to a threefold increase of the unit cell dimensions with respect to distances between oxygen atoms in the O3 structure. The large difference in atomic scattering factors between Li and Mn leads to strong superlattice reflections. Similarly superlattice reflections corresponding to a threefold increase of the in-plane unit cell can be observed when the three cation species are ordered in a regular arrangement within the transition metal layer as described by Ohzuku *et al.* [29] in a trigonal lattice ($P3_112$). Here the small difference in atomic scattering factor should result in lower intensity of the observed superlattice reflections. In the case of $LiNi_{0.5}Mn_{0.5}O_2$ the $\sqrt{3}a_{hex}$ x $\sqrt{3}a_{hex}$ $R30^o$ in plane ordering results from Li/Ni exchange where the replacement of some Ni with Li in the TM layer introduces local variations of cations arrangement as described by Meng *et al.* [28]. The two crystal structures are often used to describe how the cation arrangements differ in the oxygen stacking. If the structure constitutes a trigonal lattice ($P3_112$), there is abc.. abc… stacking and the superstructure can be termed as $\sqrt{3}a_{hex}$ x $\sqrt{3}a_{hex}$ $R30^o$ ordering and if the structure constitutes a monoclinic lattice (C2/m), there is ab.. ab.. stacking present and the reflections can be identified by monoclinic reflections. The difference between these two stacking sequences is shown in Figure 1.6.

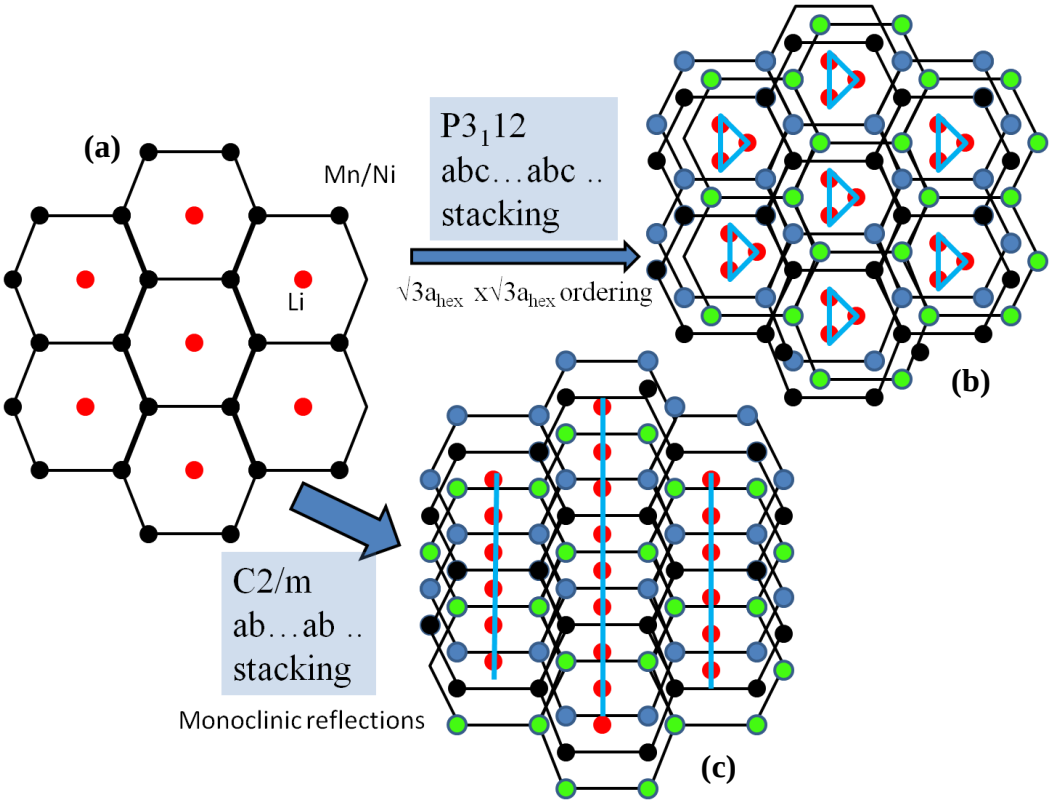

Figure 1.6 Difference between the monoclinic reflections and the $\sqrt{3}a_{hex}$ x $\sqrt{3}a_{hex}$ R30^{o} ordering based on their stacking sequences. The triangle in (b) shows the three fold symmetry and the line in (c) shows the mirror plane symmetry.

The first principle calculations [27], which show the phase diagram of $LiCoO_2$-$LiNiO_2$-$LiMnO_2$, indicate that the nickel rich phases in $LiNi_{1-x}Mn_xO_2$ are a solid solution of layered $LiNiO_2$ and $LiNi_{0.5}Mn_{0.5}O_s$ whereas the manganese-rich phases may be considered as a solid solution of layered $LiNi_{0.5}Mn_{0.5}O_2$ and rhombohedral $LiMnO_2$. These systems have been studied in order to understand the structural changes in this composition range and to predict the ordering among the cations present in the TM layers. It has been reported that a change in the ratio between nickel and manganese ion changes the oxidation state of the nickel and manganese and that this plays an important role in cation ordering in the transition metal layers.

1.4 Multiferroic materials.

The quest for fabricating various multifunctional devices still remains a challenging issue among the scientific community. These devices are particularly important in various electronics, memory devices, informatics, optoelectronics, etc. One group of important multifunctional materials is the multiferroics [30]. According to the original definition put forward by Schmid, multiferroics are materials that are simultaneously (ferro)magnetic and ferroelectric, and/or ferroelastic [31]. These materials attract attention not only because of the interesting fundamental physical phenomena in these but also their promise for applications in advanced practical multifunctional materials [32]. Ferromagnetic materials have been used for a long time for data storage and magnetic field sensors because of their spontaneous magnetization, on the other hand, ferroelectric materials have been used in computer random access memory, medical ultrasound machines, high quality infrared cameras, fire sensors, etc. because of their spontaneous electrical polarization, which can be switched by the application of electric field. In case of multiferroics, both of these properties can be experienced by a single material system due to the coupling between the spin (ferromagnetic) and the charge (ferroelectric) [33]. This connection between magnetism and electricity has a tremendous impact on the technology when the materials are in nanoscale. The most recent breakthrough is the invention of spintronics devices, where changes in conductivity can be experienced by the change in spin state of a material (discovery of giant magnetoresistance). In the case of multiferroics, the magnetic properties of a material can be tuned by the application of electric field or vice-versa [34]. This class of materials has many potential applications such as in multiple state memory elements, in which data is stored both in electric and magnetic polarizations. In the past several decades there have been extensive studies involving multiferroics that contain well-studied $BaTiO_3$ as a ferroelectric material [35]. Besides $BaTiO_3$ there are other ferroelectric materials under

investigation. In this present research, we wish to investigate the ferroelectric properties of $LiNbO_3$, a well-known ferroelectric material with a spontaneous polarization of 70 $\mu C/cm^2$ having high Curie temperature of 1483 K [36, 37]. $LiNbO_3$, with its distorted perovskite structure, has been widely used in modulators, wave guides, high-density storage and second harmonic generators. Even though there are more reports investigating the physical properties of $LiNbO_3$, not many reports can be found on the study of synthesis and ferroelectric properties of this material in the nanoscale.

1.5 $LiNbO_3$ as a ferroelectric material

A ferroelectric is an insulating system with two or more discrete stable or metastable states of different nonzero electric polarization within zero applied electric field; this is referred to as "spontaneous" polarization. For a system to be considered ferroelectric, it must be possible to switch between these states with an applied electric field (E), which changes the relative energy of the states through the coupling of the field to the polarization (P). Another way to define a ferroelectric material is one that undergoes the high-temperature phase change from a dielectric to a ferroelectric. The defining property of ferroelectricity is the switching between different metastable states by the application and removal of an electric field [38]. The mechanism of switching is understood to take place on scales longer than a unit-cell, and generally to require the growth and shrinking of domains through the motion of domain walls. Ferroelectric materials have domains and show a hysteretic response of both polarization and electric displacement to an applied electric field. As a result, they can find applications in data storage. They can also find applications as capacitors because their concentration of electric flux density results in high dielectric permeabilities. Ferroelectric materials are also used in electromechanical transducers and actuators [38].

Early work on ferroelectric materials focused primarily on Rochelle salt, $KNa(C_4H_4O_6)\cdot 4H_2O$ [39, 40]. Although studies of Rochelle salt were pivotal in establishing many of the basic properties of ferroelectric materials, the complex structure and large number of ions per unit cell made it difficult to elucidate a coherent theory of ferroelectricity from the results of experiments on this material. The most widely studied and widely used ferroelectrics today are perovskite-based oxides, ABO_3. The cubic perovskite structure consists of a small cation, B, at the center of an octahedron of oxygen anions, with large cations, A, at the unit cell corners. Below the Curie temperature, there is a structural distortion to a lower-symmetry phase accompanied by the shift off-center of the small cation [33, 38]. The spontaneous polarization derives largely from the electric dipole moment created by this shift. The comparatively simple perovskite structure and the small number of atoms per unit cell have made detailed theoretical studies of perovskite ferroelectrics possible and resulted in a good understanding of the fundamentals of ferroelectricity.

Any lattice of oppositely signed point charges is inherently unstable. Ionic materials are stable because of short-range repulsions between adjacent electron clouds. The existence or absence of ferroelectricity is determined by a balance between these short-range repulsions, which favor the non-ferroelectric symmetric structure, and additional bonding considerations, which might stabilize the ferroelectric phase. Even in ferroelectric materials, the short-range repulsions dominate at high temperature, resulting in the symmetric, unpolarized state. As the temperature is decreased, the stabilizing forces associated with the polarization of the ions as they are displaced become stronger than the short-range repulsive ionic interactions, and the polarized state becomes stable, even in the absence of an applied field.

$LiNbO_3$ and related materials are ferroelectric oxides with a trigonal paraelectric structure. While this structure can, in principle, be obtained through a distortion of the cubic perovskite structure, the necessary distortion is quite large, so that these compounds do not revert to the cubic perovskite phase at high temperatures, and the cubic perovskite structure is not an appropriate high-symmetry reference structure. Thus, it is often not considered a perovskite, though it is crystallographically the same as *R*3*c* $BiFeO_3$ differing only in the values of the structural parameters. As for the perovskites, the *R*3*c* structure is composed of oxygen octahedra containing the Nb atoms and surrounded by the Li atoms. However, relative to the perovskite structure, the oxygen octahedra have been rotated around [111], so that the Li atoms only have 6 oxygen first neighbors, rather than twelve as in the cubic perovskite structure [41]. The low-temperature *R*3*c* ferroelectric phase is obtained from the paraelectric *R*3*c* phase by displacements of the cations along the [111] direction, breaking the mirror-plane symmetry and resulting in a nonzero spontaneous polarization. For $LiNbO_3$, the paraelectric–ferroelectric transition occurs at 1483 K, with a spontaneous polarization of 71 $\mu C/cm^2$ at room temperature [36, 37]. The crystal structure of LiNbO3 is shown in Figure 1.7

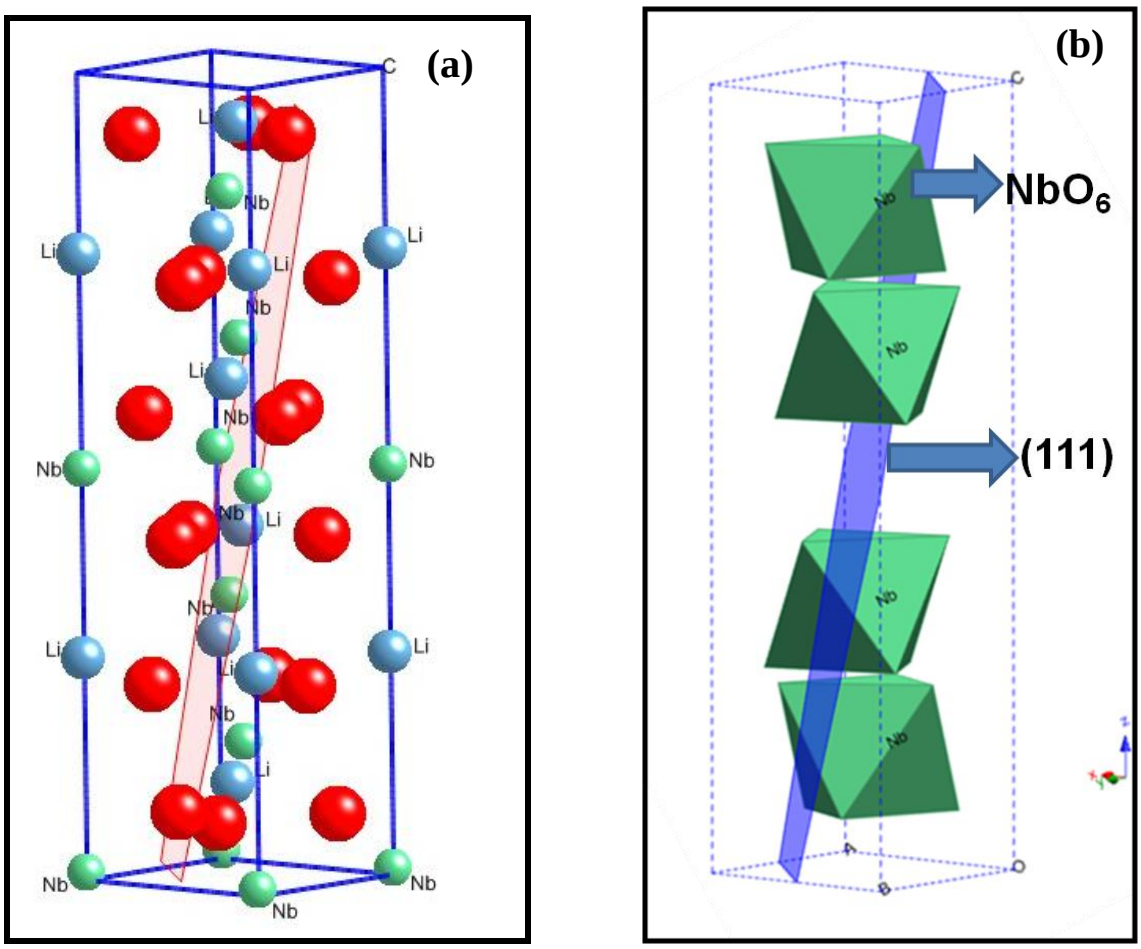

Figure 1.7 Crystal structure of $LiNbO_3$ (a and b). In b the distorted NbO_6 octahedra along [111] direction is shown which is the cause of generation of ferroelectricity in $LiNbO_3$

1.6 Transmission electron microscopy

In 1931, while conducting research for his masters at the Technical College of Berlin, Ernst Ruska and Max Knoll design the first Transmission Electron Microscope (TEM) [42]. The initial designs were able to magnify specimens up to seventeen times greater than that of a light microscope. One of the major historical limitations of TEM was that electrons were largely unable to pass through thick specimens; until the diamond knife and ultra-microtome were designed in 1951 it was largely impossible to utilize this instrument to full capacity. While the theoretical upper limit of the transmission electron microscope is estimated to be as high as 10,000 times that of a light microscope, limitations in the equipment used lowers the real limit. Combined with difficulty in preparing specimens, it is realistically only possible to resolve an object to about 0.025nm. A transmission electron microscope is similar in design to an ordinary light microscope with one key difference: instead of using light, it uses *electrons*. Using a cathode ray tube or filament (a source to generate highly excited electrons) in a vacuum, electrons are accelerated toward a given specimen by creating a potential difference. A series of magnets and metal apertures are used to focus this steam of electrons into a monochromatic beam, which allow the electrons to collide with the specimen, interact depending on the density and charge of the material, and form the image by following the simple ray optics theory. The detail of image formation and obtaining electron diffraction will be discussed in the following section.

1.6.1 Formation of image by Transmission electron microscope

As discussed, the TEM is constructed similarly in principle to the light microscopes. In case of TEM these are composed of various magnetic lenses. A cathode, called the source, is heated by applying high voltage and this leads to the emission of electrons. These electrons are then accelerated by an anode. The electron beam is diverged and focused exactly on the

specimen material by a lens called a condenser lens. Two condenser lenses are present in a TEM. The purpose of having two condenser lenses is to focus the electron beam to a very small spot of 3 - 5 μm in a diameter. This is the essential condition for formation of high intensity in a TEM. The electron beam from the specimen passes through the objective aperture and the image is formed by this objective lens. The total magnification of the image is obtained by multiplication of the individual enlargements of series of all lenses. While collecting an image, one can encounter various lens defects such as astigmatism, chromatic aberration and spherical aberration. If astigmatism is present, then the point will not be imaged as a point but as a small line. The astigmatism can be corrected by using stigmators, which are present in the form of auxiliary coil pairs and can be excited for astigmatism correction. Chromatic aberrations can be subsidized by suitable stabilization of the high voltage. However spherical aberrations cannot be corrected easily. In general, spherical aberrations determine the resolution limit of a microscope [41].

1.6.2 Theory of formation of image and electron diffraction in TEM.

In case of crystalline material, the wave nature of the electron has to be considered. According to Huygen-Fresnel principle, all the atoms serve as a source of secondary waves radiating in all spatial directions. Due to the periodic arrangement in the crystal lattice, periodic path difference can occurred between the two consecutive scattering centers. The path differences produce the phase differences. When the phase differences between two neighboring waves are exactly one wavelength that results the maximum possible constructive interference, called *Bragg diffraction* [43]. Mathematically, the Bragg equation can be written as

$$n\lambda = 2d\sin\theta$$

where, nλ= path difference of an integral multiple of wavelength of first and second lattice planes and 2θ = angle between the incident ray and the diffracted ray.

When electrons incident on the lattice planes of the material are diffracted, the simple Bragg law applies. The diffracted beams through the angle 2θ are focused by the objective lens to a diffraction spot in the back focal plane and which is projected by a projected lens to the viewing screen. The ray diagram is shown in the Figure 1.9.

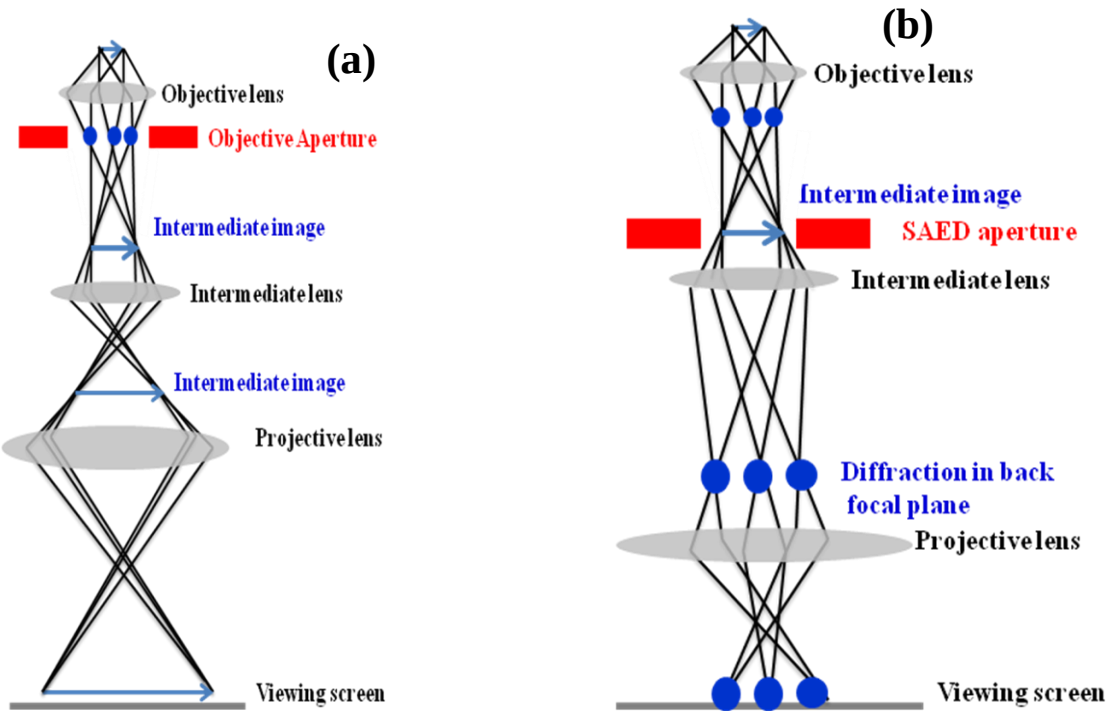

Figure 1.8 The ray diagram of (a) formation of image and (b) electron diffraction in TEM.

1.7 Magnetic properties of materials

Magnetic properties of inorganic compounds can be classified into many different categories. Six common ones are paramagnetic, ferromagnetic, diamagnetic, antiferromagnetic, ferrimagnetic and spin glass-type. Magnetic behavior is always present in the transition metal

ions which have unpaired d and f electrons. Depending upon the spin orientation of the unpaired electrons the magnetic behavior is changed. In case of paramagnetic materials, the spins of the unpaired electrons are randomly oriented in to different directions. Here the overall magnetic moment is zero. If the unpaired electrons are aligned parallel to a particular direction, the material is called ferromagnetic and it has magnetic moment which can be tuned by applying an external magnetic field. If the spins of the unpaired electrons are antiparallel then the material posses the antiferromagnetic behavior. Ferrimagnetic materials possess the unpaired electrons those are antiparallel to each other but with unequal numbers in the two directions. Spin glass-type magnetic behavior is seen in materials where the antiferromagnetic arrays is disrupted or frustrated by stronger ferromagnetic coupling. Different magnetic behavior is shown in the Figure 1.10.

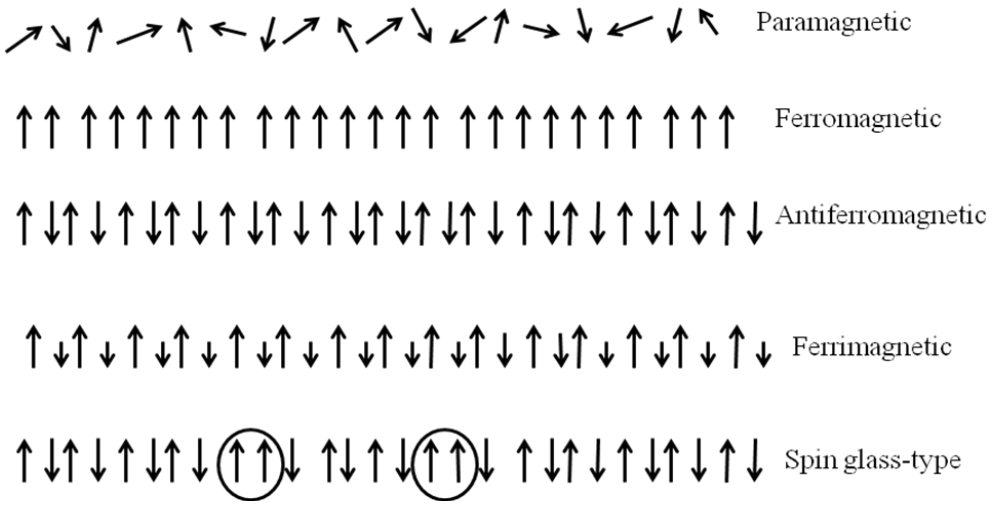

Figure 1.9 Schematic of different magnetic properties depending upon their spin orientation.

Magnetic properties of a material can be explained on the basis of the susceptibility value. The magnetic susceptibility is the ratio of magnetization to the magnetic field. The magnetic susceptibility is sometimes field dependent and temperature dependent which generally categorizes different magnetic materials.

The molar susceptibility of a paramagnetic material is always explained by Curie law which is

$$\chi = C/T, S$$

where C is the Curie constant and T is the absolute temperature. If the magnetic behavior is more complex compared to the simple paramagnetic system, then the Curie law is modified to the Curie-Weiss law and it is expressed as:

$$\chi = C/(T-\Theta),$$

where Θ is Weiss constant.

These equations can be used to determine the number of unpaired electron present in the particular paramagnetic transition metal ion species. From the linear fit on the plot of inverse magnetic susceptibility ($1/\chi$) vs. temperature (T) one can get the value of Curie constant and consequently the effective magnetic moment can be calculated by using the formula $\mu_{eff} = \sqrt{8 \times C}$. This effective magnetic moment can be compared to the theoretical effective magnetic moment by taking different number of unpaired electrons present in the transition metal ion species. Since the number of unpaired electron corresponds to the oxidation state of ions and spin value (S). The theoretical effective magnetic moment can be calculated by using the equation $\mu_{eff} = (g^2 S(S+1))^{1/2}$ where g has a value of 2 for the electron which has no spin orbit coupling.

1.8 Scope of this research

This dissertation presents the research on oxide materials for lithium-ion rechargeable batteries and oxide material which serves as a ferroelectric application in electronic devices. These are technically significant materials we are looking to investigate the structure-property-correlations by employing various characterization techniques. In chapter 2-4, the research focuses on the investigating the thermal stability and cation ordering in $LiMO_2$ (M=Co, Mn, Ni) cathode materials. We are interested in studying the structural degradation of these cathode materials after charging process in the fundamental level and monitoring the thermal stability. Thermal stability is an important aspect since this determines the safety of the lithium-ion batteries. We also study cation ordering in order to get the deeper understanding in microstructures of these oxide cathode materials after charge and discharge cycles. Studying cation ordering helps to determine the mechanism of capacity fading in cathodes and their degradation. In Chapter 5, which deals with the ferroelectric research, efforts are given to synthesize the ferroelectric nanoparticles of different shape to monitor the ferroelectricity as a function of shape. Determining the ferroelectric property of nanoparticles would give the idea of the critical size after which a ferroelectric material changes to paraelectric.

1.9 References

1. D. Linden and T.B. Reddy, *Handbook of Batteries*. 3rd ed, ed. MacGraw Hill Handbooks, **2002**.
2. *Lithium Ion Batteries - Fundamentals and Performance*; Wakihara, M.; Yamamoto, O., Eds.; Wiley-VCH, **1998**.
3. Dahn, J. R.; Fuller, E. W.; Obrovac, M.; Von Sacken, U. *Solid State Ionics* **1994**, *69*, 265-270.
4. B. Richter, D. Goldston, G. Crabtree. L. Glicksman, D. Goldstein, D. Greene, D. Kammen, M. Levine, M. Lubell, M. Savitz, D. Sperling, Energy Future: Think Efficiency; American Physical Society: College Park, MD, **2008**.
5. C. Daniel, Materials and Processing for Lithium-ion Batteries, JOM, **2008**, *60* ,43.
6. John B. Goodenough and Youngsik Kim, *Chemistry of Materials,* **2010**, *22,* 587.
7. Wang, L.; Maxisch, T.; Ceder, G. *Chemistry of Materials* **2007**, *19*, 543-552.
8. Mizushima, K.; Jones, P. C.; Wiseman, P. J.; Goodenough, J. B. *Materials Research Bulletin* **1980**, *15*, 783-789.
9. Reimers, J. N.; Dahn, J. R. *Journal of The Electrochemical Society*, **1992**, *139*, 2091.
10. Venkatraman, S.; Manthiram, A. *Chemistry of Materials,* **2002**, *14,* 3907-3912.
11. Rossen, E.; Reimers, J. N.; Dahn, J. R. *Solid State Ionics* **1993**, *62*, 53.
12. Mizushima, K.; Jones, P. C.; Wiseman, P. J.; Goodenough, J. B. *Materials Research Bulletin* **1980**, *15*, 783-789.
13. Czyzyk, M. T.; Potze, R.; Sawatzky, G. A. *Physical Review B* **1992**, *46*, 3729.
14. Dahn, J. R.; Fuller, E. W.; Obrovac, M.; Von Sacken, U. *Solid State Ionics* **1994**, *69*, 265.
15. T. Ohzuku; Y. Makimura, *Chemistry Letters* **2001**, *7*, 6423.
16. I. Belharouak; Y.K. Sun; J. Liu; K. Amine, *Journal of Power Sources* **2003**, *123*, 247.
17. J.W. Wen; H.J. Liu; H. Wu; C.H. Chen *Journal of Materials Science* **2007**, *42*, 7696.
18. N. Yabuuchi; Y. Koyama; N. Nakayama; T. Ohzuku *Journal of The Electrochemical Society* **2005**, *152*, A1434.
19. X. Luo; X. Wang; L. Liao; X. Wang; S. Gamboa; P.J. Sebastian *Journal of Power Sources* **2006**, *161*, 601.
20. R. D. Shannon *Acta Crystallographica A.* **1976**, *32*, 756.
21. J. M. Paulsen, C. L. Thomas, and J. R. Dahn, *Journal of The Electrochemical Society***1999,** *146,* 3560.
22. J. R. Dahn, U. v. Sacken, and M. C.A., *Solid State Ionics,***1990**, *44,* 87.
23. R. Kanno, H. Kubo, Y. Kawamoto, T. Kamiyama, F. Izumi, T. Y., and M. Takano, *Journal of Solid State Chemistry*, **1994,** *11,* 216.
24. A. Hirano, R. Kanno, Y. Kawamoto, T. Y., K. Yamaura, M. Takano, K. Ohyama, M. Ohashi, and Y. Yamaguchi, *Solid State Ionics*, **1995,** *78,* 123.
25. Y. Arachi, H. Kobayashi, S. Emura, Y. Nakata, M. Tanaka, and T. Asai, *Chemistry Letters*, **2003,** *32*, 60.
26. J. Reed and G. Ceder, *Electrochemical and Solid-State Letters* , **2002,** *5,* A145.
27. Y. S. Meng, G. Ceder, C. P. Grey, W.-S. Yoon, and Y. Shao-Horn, *Electrochemical and Solid-State Letters*, **2004,** *7,* A155.
28. Y. S. Meng, G. Ceder, C. P. Grey, W.-S. Yoon, M. Jiang, J. Breger, and Y. Shao-Horn, *Chemistry of Materials*, **2005**, *17*, 2386.
29. T. Ohzuku and Y. Makimura, *Chemistry Letters* **2001,** *8*, 744.

30. Wang. Y.; Hu. J.; Lin. Y.; Nan, C. W. *Nature Publishing Group Asia Materials* **2010**, *2*, 61.
31. Schmid, H. *Ferroelectrics* **1994**, *162*, 317.
32. Scott, J. F. *Nature Materials* **2007**, *6*, 256.
33. Hill, N. A. *Journal of Physical Chemistry B* **2000**, *104*, 6694.
34. Eerenstein, W.; Mathur, N. D.; Scott, J. F. *Nature* **2006**, *442*, 759.
35. Raidongia, K.; Nag, A.; Sundaresan, A.; Rao. C.N.R. *Applied Physics Letters* **2010**, *97*, 062904.
36. Inbar, I.; Cohen, R. E. *Phys. Rev. B* **1996**, *53*, 1193-1204.
37. Zhang, D. L.; Zhang, W. J.; Zhuang, Y. R.; Pun, E. Y. B. *Cryst. Growth Des.* **2007**, *7*, 1541-1546.
38. K. Rabe, C. H. Ahn, J.-M. Triscone (Eds.): *Physics of Ferroelectrics: A Modern Perspective, Topics Appl. Physics,* **2007,** *105*, 1–30.
39. Pockels, F. *Abh. Gott* **1894**, *39*, 1.
40. Valasek, J. *Phyics. Review.* **1921**, *17*, 475.
41. M. E. Lines, A. M. Glass: *Principles and Applications of Ferroelectrics and Related Materials* (Clarendon, Oxford 1977) 2.
42. D. B. Williams and C. B. Carter; Transmission *Electron Microscopy(Springer, New York, NY)* **1996**.

Chapter 2

Comparison of magnetic properties in Li_xCoO_2 and its decomposition products $LiCo_2O_4$ and Co_3O_4

Abstract

Thermal stability of cathode material in the charged state is an important aspect for the safety of rechargeable batteries. It is well known that layered Li_xCoO_2 decomposes to a mixture of $LiCoO_2$ and Co_3O_4 at elevated temperatures. However, not many experimental evidences exist on intermediate phases those may form during the decomposition. Using magnetic measurements we show that it is possible to distinguish between the spinels $LiCo_2O_4$ and Co_3O_4 and thereby follow the decomposition reaction of Li_xCoO_2. We characterize the magnetic behavior of thermally aged Li_xCoO_2 (x = 0.98, 0.76, 0.55) with increasing annealing time. Our results reveal the appearance of magnetic ordering in the thermally degraded products. The detailed analysis illustrates that the formation of Co_3O_4 is preceded by the formation of a metastable $LiCo_2O_4$ phase.

2.1 Introduction

Layered $LiCoO_2$ is extensively used as a positive electrode material for Li-ion batteries [1-2]. This compound crystallizes in the α-$NaFeO_2$ type structure described by space group $R\bar{3}m$ with lithium and cobalt ions in octahedral 3a and 3b sites, respectively, separated by layers of cubic close packed oxygen ions. In the fully lithiated state, $LiCoO_2$ behaves like an insulator with a wide band gap of 2.7 eV [3,4]. $LiCoO_2$ has a high operating voltage vs. a lithium electrode and a large specific capacity of 140 mAh/g [2]. Deintercalation and reinsertion of lithium during repeated cycling through the composition range $0.5 \leq x \leq 1$ in Li_xCoO_2 leaves the layered structure intact [5]. At elevated temperature, the under-stoichiometric phase Li_xCoO_2 converts to a mixture of layered $LiCoO_2$ and Co_3O_4 with evolution of oxygen [6]. Alternatively, the decomposition of layered Li_xCoO_2 can proceed via formation of the ideal $LiCo_2O_4$ spinel as suggested by First Principle Investigations [7]. This reaction in the technologically relevant Li concentration range takes place without oxygen release. In earlier studies by single crystal electron diffraction we observed the formation of the ideal spinel $LiCo_2O_4$ on the surface of aged Li_xCoO_2 particles and in Li_xCoO_2 after long term annealing [8,9]. Here we explore the application of magnetic measurements to distinguish between the two possible decomposition products Co_3O_4 and $LiCo_2O_4$ in thermally aged Li_xCoO_2.

The study begun with layered $LiCoO_2$ that was subjected to chemical delithiation before annealing at 350°C for increasing lengths of time. The magnetic behavior of perfectly stoichiometric $LiCoO_2$ is determined by Co^{+3} ions in low spin configuration ($t_{2g}^6\ e_g^0$; S= 0) as shown by magnetic susceptibility measurements, muon spin rotation spectroscopy (μ_+SR), X-ray absorption and X-ray emission spectroscopy [10-12] . Hence no local spin moment is expected in perfectly stoichiometric $LiCoO_2$. A slight increase in measured susceptibility is however

observed at temperatures below 60 K indicating spin state transitions in Co^{+3} ions [11]. Upon lithium deintercalation from $LiCoO_2$, the compound remains paramagnetic while Co^{+3} ions are oxidized to Co^{+4} for charge compensation introducing magnetic moment in Li_xCoO_2 ($x < 1$) [1,11]. Some authors have observed an anomaly in lithium deficient materials around 175 K where the linear increase in susceptibility with decreasing temperature is interrupted and a wide minimum begins before the susceptibility (χ) increases again at lower temperatures [1,10,11,13]. The origin of this phenomenon is not fully understood yet; spin dimerization of Co^{+4} ions, charge ordering, spin state transitions, or presence of small amounts of an impurity phase are considered to be the possible mechanisms [10,11,13].

The reaction products of thermal decomposition, $LiCo_2O_4$ and Co_3O_4, both belong to the family of AB_2O_4 spinels (Space group: $Fd\bar{3}m$) where the A and B ions occupy tetrahedral 8a and octahedral 16d interstitial sites respectively [14]. In $LiCo_2O_4$ the tetrahedral 8a sites are occupied by Li ions (Li^+) whereas in Co_3O_4 tetrahedral sites are occupied by Co^{+2} ions. The octahedral 16d sites are occupied by a mixture of $Co^{+3/+4}$ in $LiCo_2O_4$ and by Co^{+3} in case of Co_3O_4 [15-16]. The presence of nonmagnetic Li ions or magnetic Co^{+2} ions in A sites affects the magnetic behavior of these compounds and is used here to distinguish between $LiCo_2O_4$ and Co_3O_4. In Co_3O_4 the super-exchange interaction between Co^{+2} ions in tetrahedral sites separated by Co^{+3} ions in octahedral sites and oxygen results in antiferromagnetic (AFM) ordering at low temperature along the path A-O-B-O-A [15]. A similar superexchange interaction is not possible in $LiCo_2O_4$ where Co is in +3/+4 oxidation state. Here the tetrahedral site is occupied by an alkali metal ion and interactions between Co ions are either direct or via oxygen in the form of 90^o Co-O-Co bonding [16]. The magnetic behavior of AB_2O_4 systems, where A is a non-transition element and B is a transition element, has been classified as geometrically frustrated at

low temperatures reflecting short range ordering of magnetic ions [14,17,18]. Here the corner (vertex) sharing tetrahedral magnetic lattice sites (octahedral 16d sites) satisfy the condition of magnetic frustration as it is impossible to align the spins at the corners of a regular tetrahedron in a mutually antiparallel manner – hence two spins are always frustrated [19]. While the magnetic behavior of Co_3O_4 has been investigated in the past, no detailed reports could be found on $LiCo_2O_4$. The structure of $LiCo_2O_4$ and Co_3O_4 spinels are presented in Figure 2.1.

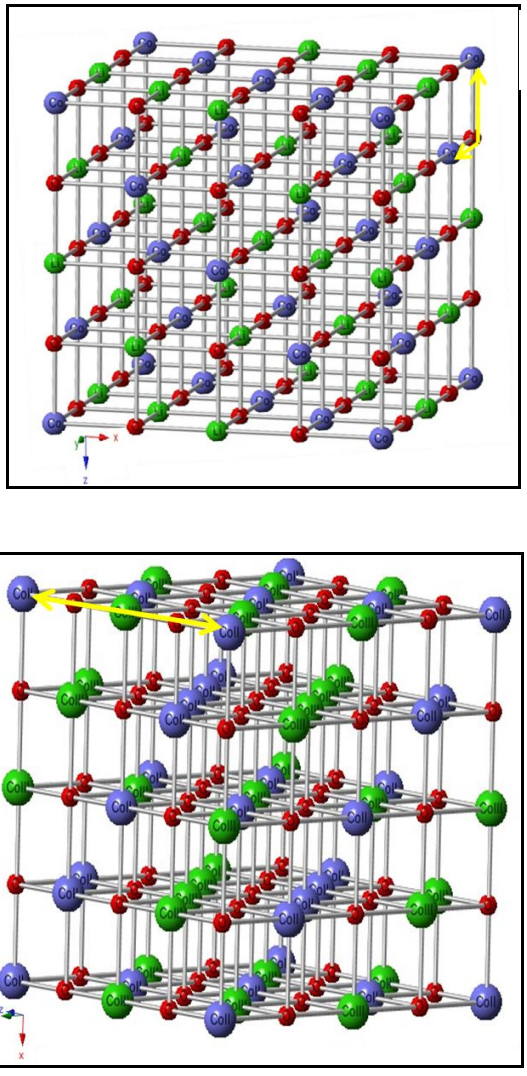

Figure 2.1 Structure of AB_2O_4 spinels: (a) $LiCo_2O_4$ and (b) Co_3O_4. The arrows show the nature of interaction (90 degree and 180 degree, respectively) between cobalt ions.

2.2 Experimental

$LiCoO_2$ was prepared following a poly acrylic acid (PAA) -assisted sol-gel method modified the procedure as described in this report [20]. The required amounts of lithium and cobalt nitrate salts were dissolved in distilled water at a cationic ratio of 1:1, PAA was added as a chelating agent. The pH of the aqueous solution was set to 1 - 2 by drop wise addition of HNO_3, and then the solution was stirred for 24 hours at room temperature before being evaporated to dryness at 70 $^{\circ}$C – 80 $^{\circ}$C. The obtained precursor was ground thoroughly and calcined in air at 750 $^{\circ}$C for 10h to form $LiCoO_2$ powder. Chemical delithiation was carried out under argon atmosphere at room temperature using solutions of NO_2BF_4 in acetonitrile in different concentrations. The reaction was carried out by adding NO_2BF_4 solution drop wise over 90 minutes to the $LiCoO_2$ suspensions followed by additional 90 minutes of stirring to obtain Li_xCoO_2 (x = 0.98, 0.76, 0.55). Portions of the delithiated products were annealed at 350 $^{\circ}$C in air for 40 minutes and for 24 hours.

2.3 Characterization

For the starting material and its delithiated compounds, quantitative analysis of Co and Li content was carried out through Inductive Coupled Plasma Mass Spectrometry (ICP-MS). For the starting material, the cobalt oxidation state was determined by idometric titration following the procedure published by Conder *et al.* [21]. X-ray diffraction (XRD) data were collected with an X'pert PRO diffractometer (Panalytical Instruments) operated at 40 kV voltage and 40 mA current using Cu-Kα radiation. Silicon powder was mixed into the Li_xCoO_2 powders as an internal standard. Phase determination was carried out by comparison between experimental and simulated powder diffraction patterns obtained with the software "Powder cell" and with unit cells published in the literature [5]. Magnetic measurements were performed under field cooling

(FC) and zero field cooling (ZFC) conditions with a superconducting quantum interface device (SQUID) magnetometer (MPMS-XL-7: Quantum Design) in the temperature range between 5 K - 300 K under magnetic field, H = 10 kOe. The Curie constant, the Weiss constant, and the effective magnetic moment, μ_{eff}, of all powders were determined from the plot of inverse susceptibility versus temperature in the temperature region 180 - 300 K.

2.4 Results and Discussion

2.4.1 Starting material and delithiated Li_xCoO_2

The composition of each sample was calculated from the amount of Li and Co measured by ICP and the total amount of dissolved specimen. The resulting chemical formulae are listed in the first column of Table 1. For simplicity we omit the slight discrepancy in Co content in the following text and refer to the specimens by their Li content only. X-ray powder diffraction pattern of the virgin and delithiated Li_xCoO_2 (x = 0.98, 0.76, 0.55) powders are shown in Figure 2.2. All spectra can be indexed completely in the α-$NaFeO_2$ type structure with $R\bar{3}m$ space group. The clear splitting of the (006)/(102) and (108)/(101) doublet peaks indicates that the synthesized material has layered character that is maintained after delithiation [5]. With decreasing lithium content in the delithiated material, the position of the (003) peak shifts to smaller angles, that is in agreement with an expansion of the lattice along the c axis caused by increased electrostatic repulsion between CoO_2 slabs [5,22]. The lattice parameters and c/a ratios are given in the Table 1. The value of c/a ratio is maintained in case of all delithiated materials (4.99) which indicates that the compounds have no spinel phase present as an impurity.

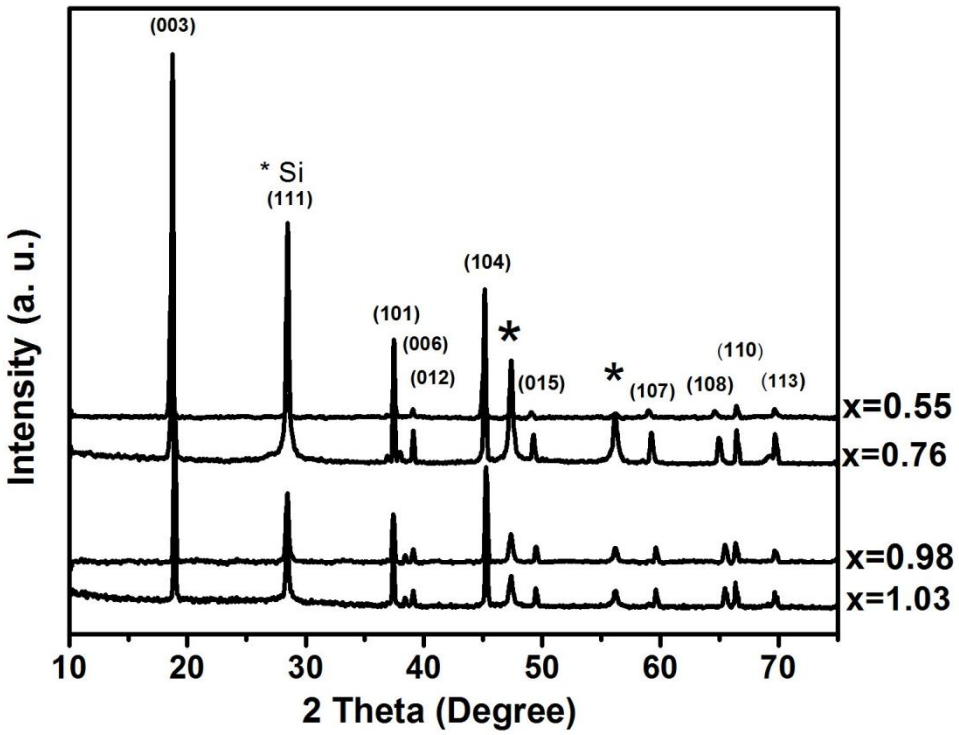

Figure 2.2 X-ray diffraction spectra of Li_xCoO_2 (x=1.03, 0.98, 0.76, 0.55) before heat treatment.

Table 2.1 Effective magnetic moment and Weiss constant of starting and delithiated materials.

Sample (ICP composition)	c-lattice parameter (A^o)	a-lattice parameter (Å)	c/a ratio	Effective magnetic moment (μ_B)	Weiss constant θ (K)
$Li_{1.03}Co_{1.02}O_2$	14.05	2.82	4.99	0.08 ± 0.03	-239
$Li_{0.98}Co_{1.02}O_2$	14.10	2.85	4.99	0.73 ± 0.08	-264
$Li_{0.76}Co_{1.01}O_2$	14.28	2.86	4.99	1.49 ± 0.03	-98
$Li_{0.55}Co_{1.01}O_2$	14.38	2.88	4.99	1.73 ± 0.02	-177

The temperature dependence of the magnetic susceptibility of the starting material and its delithiated products are shown in Figure 2.3. All samples show paramagnetic behavior at higher temperature ($T \geq 180$ K) consistent with Curie Weiss behavior, identical responses are observed under field cooling (FC) and under zero-field- cooling (ZFC) as we reported in the previous report [23]. The anomaly in magnetic susceptibility observed by other authors [1,10,11] in delithiated materials at 175 K is absent here. Below 50 K the magnetic susceptibility increases with decreasing the temperature in the delithiated powders. This trend is very small in $Li_{0.98}CoO_2$ but pronounced for lithium contents x = 0.76 and x = 0.55. A non-monotonic behavior is observed in the magnetic response upon cooling (χ of $Li_{0.76}CoO_2$ is less than χ of $Li_{0.55}CoO_2$ at T = 5 K, see Figure 2.3).

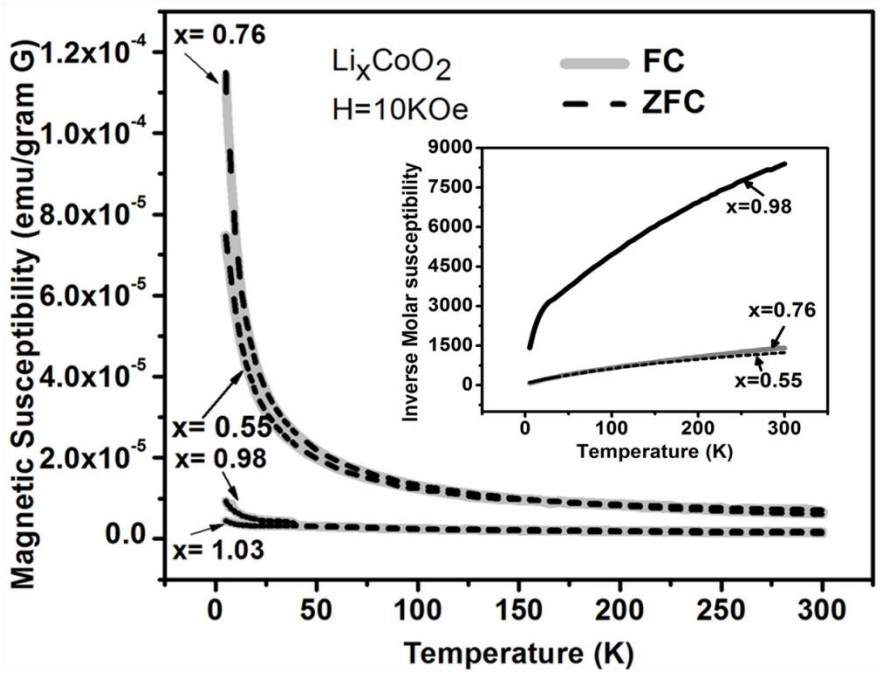

Figure 2.3 Temperature dependence of magnetic susceptibility χ of Li_xCoO_2 before heat treatment and inset shows the variation of inverse molar susceptibility with the temperature (FC mode).

This may be due to the presence of more antiferromagnetic character in $Li_{0.55}CoO_2$ as compared to $Li_{0.76}CoO_2$. Generally, the increased magnetic moment at low temperature in Li_xCoO_2 is attributed to spin state transitions in Co-ions [1,10,11,13]. Even in pure stoichiometric $LiCoO_2$, a small magnetic moment and an increase of magnetic susceptibility has been observed at low temperatures [24]. In Table 1, the effective magnetic moment values (along with the experimental uncertainties) of each specimen obtained from the linear plot of inverse molar magnetic susceptibility ($1/\chi$) vs. temperature (T) in the region of 180 K-300 K (plot of inverse molar magnetic susceptibility with temperature is given in inset of Figure 2.2) is listed together with the determined magnetic constants. Below we compare the experimental data to theoretical effective magnetic moments that were calculated for appropriate amounts of Co^{4+} in high spin (HS), low spin (LS) and intermediate spin (IS) state (S= $^5/_2$, $^1/_2$, $^3/_2$) with the goal to determine the spin states of cobalt ions at room temperature for each specimen composition.

The composition of the starting material is slightly over-stoichiometric ($Li_{1.03}CoO_2$) indicating an imbalance between the number of Co^{+3} ions and Li^+ ions that must be compensated for. Several models have been proposed for the distribution of cations and the resulting Co oxidation states in $Li_{1+x}CoO_2$. In the simplest approach, the overall charge balance of the compound requires the presence of some Co^{+2} ions [10]. In case excess Li occupies Co sites, nearby Co^{3+} ions could be oxidized to Co^{+4} for charge balance within the Co-O-slabs [10] or excess Li may be compensated for by the formation of Co and oxygen vacancies which can be described as $Li_{interslab}[Co_{1-t}\square_t][O_{2-\square}]$, where □ stands for vacancy. In the latter case the presence of Co^{2+} ions in low spin configuration has been suggested [25]. Alternatively, if excess lithium occupies cobalt sites, the oxidation state Co^{+3} could be maintained through formation of nearby oxygen vacancies [26]. Co^{+3} ions adjacent to oxygen vacancies could then experience shifts in

relative energy levels of the 3d electrons that enable spin state transitions from non magnetic low spin to magnetic intermediate spin state. In our case idometric titration of the starting material yields an average Co oxidation state to $Co^{+2.97}$, this is in agreement with the presence of Co^{+2} ions. Experimentally we determined an effective magnetic moment of $0.08\mu_B$ for the starting material, which is identical to the theoretical value of 0.05 μ_B resulting from the presence of 0.03 Co^{+2} in low spin state (μ_{theo}= 0.05 μ_B). The combined results of magnetic measurement and chemical composition confirm that Co^{+2} is present in overstoichiometric $Li_{1+x}CoO_2$ and support to the hypothesis that Co and oxygen vacancies form in the presence of excess lithium within the Co-O slabs.

Here it is reasonable to explain the spin state transitions in Co ions due to shifts in relative energy levels of the 3d electrons. In previous experiments by convergent beam electron diffraction (CBED) it was found that $LiCoO_2$ expands parallel to the c-direction when cooled with liquid N_2 (77 K) [27]. This expansion likely reduces the distortion of CoO_6 octahedra in the layered structure and thereby minders the crystal field splitting between t_{2g} and e_g orbitals [28]. Assuming the expansion continues with further decrease in temperature, spin state transitions of cobalt ions from nonmagnetic low spin to magnetic intermediate spin states can be facilitated.

During chemical delithiation, a maximum of 0.48 Li is removed in $Li_{0.55}CoO_2$. Formally the removal of lithium is compensated for by oxidation of Co^{+3} (LS) to Co^{+4} introducing unpaired spins those give rise to magnetic moments regardless of the spin state (Co^{+4} : high spin S = $^5/_2$, intermediate spin S = $^3/_2$, low spin S = $^1/_2$). In $Li_{0.76}CoO_2$ and $Li_{0.55}CoO_2$, the experimental determined effective magnetic moments are in close agreement with theoretical values obtained for appropriate amounts of Co^{4+}. Considering 0.24 Co^{+4} ions in high spin state in $Li_{0.76}CoO_2$ yields a theoretical value $\mu_{eff(\mathbf{theo})}$ of 1.48 μ_B which compares to an experimental value

of 1.49 μ_B. Similarly the experimental effective magnetic moment of 1.73 μ_B in $Li_{0.55}CoO_2$ is best described by 0.45 Co^{+4} ions in intermediate spin state that corresponds to a theoretical value $\mu_{eff(\mathbf{theo})}$ of 1.74 μ_B. In the literature, Co^{+4} ions in Li_xCoO_2 are reported to be HS for Li concentrations between x = 1.00 and 0.70 [11] or to change from high spin state at lithium concentrations above x > 0.9 to low spin state for Li concentrations between approximately 0.8 and 0.7 [10]. In the latter study, a further decrease in magnetic moments is measured below x = 0.65 which is attributed to a change in localization of unpaired spins.

The agreement between theoretical and experimental values is less satisfactory in the case of $Li_{0.98}CoO_2$. Here the experimentally determined effective magnetic moment is 0.731 μ_B while the highest possible theoretical effective moment caused by 0.02 Co^{+4} ions in high spin state is only $\mu_{eff(\mathbf{theo})}$ = 0.18 μ_B. The large discrepancy suggests that other effects contribute to the observed magnetic behavior in $Li_{0.98}CoO_2$, such as charge disproportionation of Co^{+3} or surface effects. Charge disproportionation is possible in $LiCoO_2$ with Li content is near 1 where Co should be in the +3 oxidation state but may be considered to fluctuate due to thermal vibrations or Li diffusion [11].

2.4.2. Short and long term annealed Li_xCoO_2

The XRD patterns of the annealed powders are shown in Figure 2.4. where the lithium concentrations Li_xCoO_2 (x = 0.98, 0.76, 0.55) of the delithiated powders are marked at the right side of the graphs and "(a)" or "(b)" stand for annealing times of 40 minutes and 24 hours respectively (T= 350 ºC). The c and a lattice parameter for annealed specimens are given in Table 2. A comparison between the graphs shows the appearance of the prominent spinel (220) peak at $2\theta \sim 31^o$ for the material which has low lithium content and after long time annealing. The positions of most spinel peaks partially overlap with those of the layered phase and therefore

are not easily detected. The (220) peak is unique to the cubic phase and is therefore used as an indicator for its presence. In Figures 2.4 and 2.6., the variation of magnetic susceptibility (χ) with temperature T is shown for 40 minutes annealing time and for 24 hours annealing time, respectively. In both figures the susceptibility values $\chi(T)$ are identical under FC and ZFC over most of the temperature range, but start to diverge below a transition temperature around 25 to 30 K. In the short term annealed powders, the FC curve continues to increase monotonously at a slightly lower rate below the transition temperature whereas a stronger decrease of slope is observed in the ZFC curve, indicating transitions in the arrangement of spin states in Co ions. In the literature, a comparable small hysteresis between FC and ZFC is associated with spin-glass-like behavior or with geometrically frustrated ordering of magnetic ions in the lattice [29]. In the present case we speculate that an intermediate ideal or inverse $LiCo_2O_4$ spinel phase forms during the transformation of the delithiated layered powders to a mixture of layered $LiCoO_2$ and Co_3O_4 [7]. In the ideal spinel octahedral 16 d sites are occupied by Co^{+3} and Co^{+4} ions, while Li is located on tetrahedral 8a sites. Thus clusters of unpaired spins of Co^{+4} ions may form that are frustrated geometrically in plane or between the planes. Anderson first proposed that weak interactions may result from a cation-anion-cation angle of 90^o [30]. In $LiCo_2O_4$ there is a 90° Co-O-Co interaction which may be the cause of short range ordering resulting in magnetic frustration in the lattice. In the case where a 40 minute annealing time is insufficient for complete ordering of Li and Co into tetrahedral and octahedral sites, short range magnetic interaction could be present between Co^{4+} ions in tetrahedral sites in adjacent layers or between Co^{4+} in tetrahedral and octahedral sites. In a study on the lithiated spinel $Li_2Co_2O_4$ and its delithiated product $LiCo_2O_4$, no diverging magnetic behavior has been reported in ZFC and in FC indicating a lack of magnetic ordering [16]. In that case the starting material was $Li_2Co_2O_4$

with Li in 16c and Co in 16d sites. Therefore a comparison of the present data to the literature gives rise to the speculation that, in the present study, Co ions occupy both tetrahedral and octahedral sites.

Table 2.2 Effective magnetic moment and Weiss constant of delithiated materials after heat treatment at 350^{o}C for (a) 40 min and (b) 24 hrs.

Sample	Effective magnetic moment ($\mu_{B)}$	Weiss constant θ (K)
$Li_{0.98}CoO_2$(a)	1.06 ± 0.07	-440
$Li_{0.98}CoO_2$(b)	1.08 ± 0.05	-301
$Li_{0.76}CoO_2$(a)	1.51 ± 0.02	-69
$Li_{0.76}CoO_2$(b)	1.56 ± 0.01	-78
$Li_{0.55}CoO_2$(a)	1.79 ± 0.01	-46
$Li_{0.55}CoO_2$(b)	1.90 ± 0.02	-78

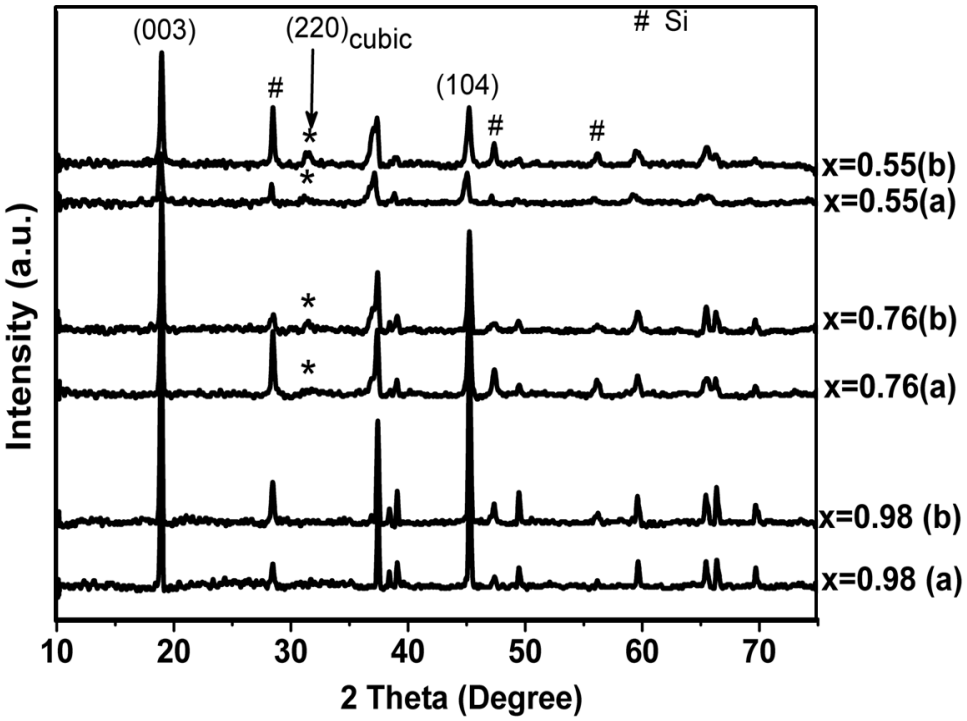

Figure 2.4 X-ray diffraction spectra of Li_XCoO_2 (x= 0.98, 0.76, 0.55) after heat treatment at 350^oC (a): 40 minutes, (b) 24 hours. The symbol # shows the Si peaks and * shows the (220) reflection from spinel phase.

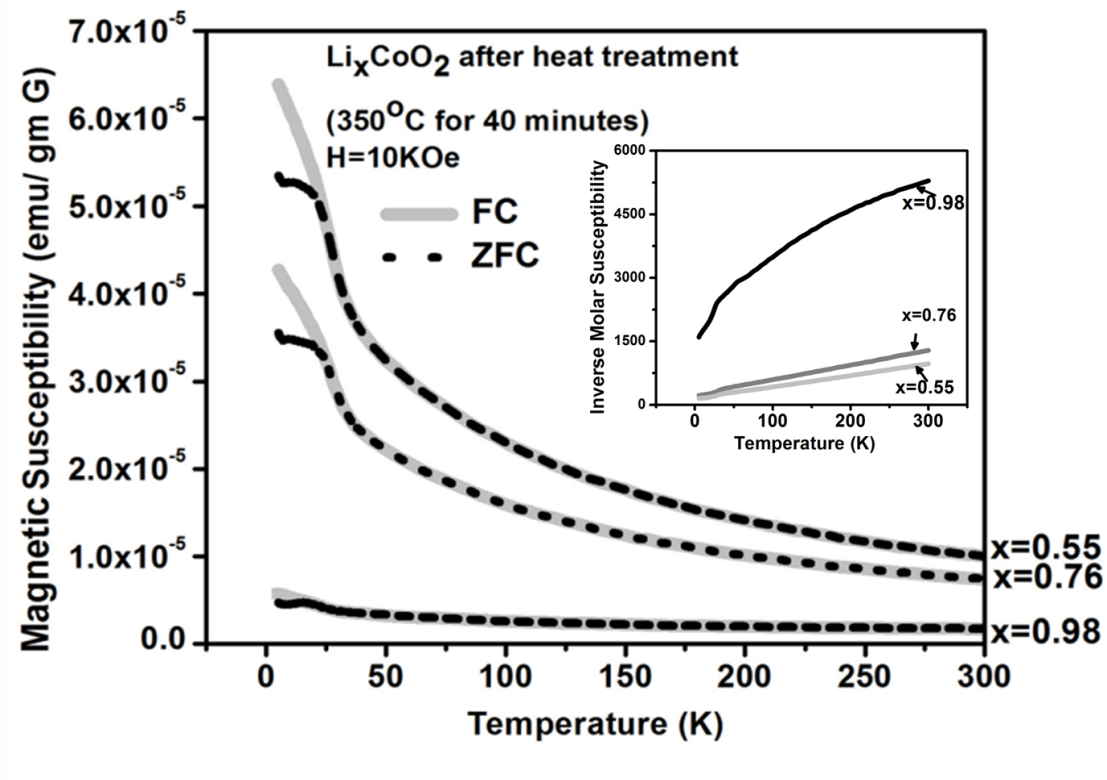

Figure 2.5 Temperature dependence of the magnetic susceptibility χ in Li_xCoO_2 subjected to heat treatment at 350 °C for 40 minutes; inset shows the variation of inverse molar susceptibility with the temperature (FC mode).

After 24 hours of annealing time the χ(T) curves, as shown in Figure 2.5, diverge more pronouncedly under FC and ZFC with the stronger effect observed under ZFC. In Figure 2.5 it can be seen clearly that below the transition temperature of about 30 K the χ_{FC} and χ_{ZFC} curves bifurcate strongly towards lower susceptibility values. This type of magnetic behavior can be referred to as AFM nature of a material below the Néel temperature T_N [31]. The experimentally determined effective magnetic moments μ_{eff} from the linear plot of inverse molar magnetic susceptibility vs. temperature in the region of T = 180 K - 300 K of the annealed powders are listed in Table 2.4 together with the obtained magnetic constants (plot of inverse molar magnetic susceptibility with temperature is given in the inset of Figure 2.4 and Figure 2.5). Comparison

shows that μ_{eff} increases as the lithium content decreases, or increases with annealing time for a given composition, indicating an increase in the number of magnetic ions. The effective magnetic moments (along with experimental uncertainties) and the Curie-Weiss temperatures reported in Table 2.4 are significantly different than the values reported by other authors [31,32]. This difference can be explained as follows. In the literature the effective magnetic moment and Curie-Weiss temperature values correspond to pure $LiCo_2O_4$ [32] or pure Co_3O_4 [31] materials.

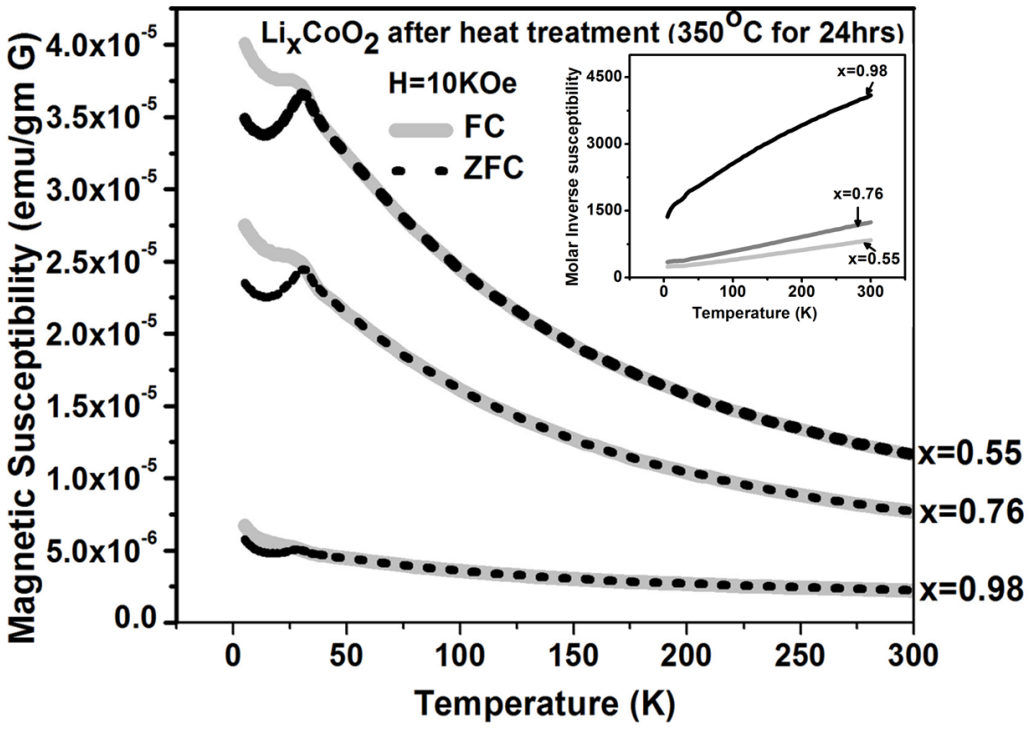

Figure 2.6 Temperature dependence of magnetic susceptibility χ of Li_xCoO_2 after heat treatment at 350 °C for 24 hours and inset shows the variation of inverse molar susceptibility with the temperature (FC mode).

But, in the present study, the materials contain both the spinel and layered $LiCoO_2$ phase. It is well known that the thermal decomposition of Li_xCoO_2 eventually leads to the formation of

Co_3O_4 thereby increasing the number of Co^{+2} ions that contribute to the observed magnetic behavior [7,6]. In the normal spinel Co_3O_4, Co^{+2} and Co^{+3} ions occupy tetrahedral 8a sites and octahedral 16d sites respectively. The role of the Jahn-Teller active Co^{+2} ion in the magnetic behavior of Co_3O_4 has been discussed in detail by Roth [15]. The spin state of Co^{+3} and Co^{+2} ions are low spin (S = 0) and high spin (S = $^3/_2$), respectively. During cooling, Co_3O_4 undergoes long-range antiferromagnetic ordering as spin states of Co^{+2} ions on A sites that are tetrahedrally surrounded by four nearest neighbors in A sites align in anti-parallel fashion. Additionally superexchange interaction between Co^{+2} ions on 8a sites through Co^{+3} ions on 16d sites and oxygen atoms via the path A-O-B-O-A contributes to the observed magnetic moment [15,29] . The T_N value for the AFM transition observed here is $T \sim 30$ K which is in agreement with value reported for Co_3O_4 spinel [31]. In an earlier investigation combining magnetic measurements and electron-energy-loss spectroscopy, we found evidence that during the continued decomposition of Li_xCoO_2 small amounts of CoO were formed that further add to the detected magnetic moment [9].

2.5. Conclusions

Magnetic studies of Li_xCoO_2 (x = 0.98, 0.76, 0.55) were conducted before and after heat treatment under zero field and field cooling to elucidate the nature of the spinel phase that forms in addition to the layered $LiCoO_2$ phase. The results show that the $LiCo_2O_4$ phase is formed before the end product Co_3O_4 is observed. Prior to heat treatment paramagnetic behavior is observed without indication of magnetic ordering down to 5 K. Heat treatment of delithiated materials progressively changes the magnetic nature within the compounds. After short term heat treatment of Li_xCoO_2 spin-glass-like or geometrically frustrated behavior is observed that suggests the formation of metastable spinel phase in the lattice. After long-term annealed

pronounced antiferromagnetic ordering is observed which is in agreement with the formation of Co_3O_4. At the same time the effective magnetic moment increases with annealing time due to introduction of Co^{+2} ions resulting from formation of Co_3O_4 phase.

2.6 References

(1) Mukai, K.; Sugiyama, J.; Ikedo, Y.; Andreica, D.; Amato, A.; Brewer, J. H.; Ansaldo, E. J.; Russo, P. L.; Chow, K. H.; Ariyoshi, K.; Ohzuku, T.; Pergamon-Elsevier Science Ltd, 2008; pp 1479.

(2) *Lithium Ion Batteries - Fundamentals and Performance*; Wakihara, M.; Yamamoto, O., Eds.; Wiley-VCH, 1998.

(3) Czyzyk, M. T.; Potze, R.; Sawatzky, G. A. *Physical Review B* **1992**, *46*, 3729.

(4) Van Elp, J.; Wieland, J. L.; Eskes, H.; Kuiper, P.; Sawatzky, G. A.; de Groot, F. M. F.; Turner, T. S. *Physical Review B* **1991**, *44*, 6090.

(5) Reimers, J. N.; Dahn, J. R. *Journal of Electrochemical Society* **1992**, *139*, 2091.

(6) Dahn, J. R.; Fuller, E. W.; Obrovac, M.; Von Sacken, U. *Solid State Ionics* **1994**, *69*, 265.

(7) Wang, L.; Maxisch, T.; Ceder, G. *Chemistry of Materials* **2007**, *19*, 543552.

(8) Gabrisch, H.; Yazami, R.; Flutz, B. *Journal of electrochemical society* **2004**, *151*, A891.

(9) Gabrisch, H.; Kombolias, M.; Mohanty, D. *Solid State Ionics* **2010** *181*, 71.

(10) Hertz, J. T.; Huang, Q.; McQueen, T.; Klimczuk, T.; Bos, J. W. G.; Viciu, L.; Cava, R. J. *Physical Review B* **2008**, *77*, 075119

(11) Sugiyama, J.; Nozaki, H.; Brewer, J. H.; Ansaldo, E. J.; Morris, G. D.; Delmas, C. *Physical Review B* **2005**, *72*, 144424.

(12) Galakhov, V. R.; Ovechkina, N. A.; Shkvarin, A. S.; Shamin, S. N.; Kurmaev, E. Z.; Kuepper, K.; Takács, A. F.; Raekers, M.; Robin, S.; Neumann, M.; Gavrila, G. N.; Semenova, A. S.; Kellerman , D. G.; and, K. T.; J., N. *Physical Review B* **2006**, *74*, 045120.

(13) Ito, A.; Tanaka, K.; Kawaji, H.; Atake, T.; Ando, N.; Hato, Y. *Journal of Thermal Analysis Calorimetry* **2008**, *92* 399.

(14) Anderson, P. W. *Physical Review* **1956**, *102*, 1008.

(15) Roth, W. L. *Journal of Physics and Chemistry of Solids* **1964**, *25*, 1.

(16) Choi, S.; Manthiram, A. *Journal of Solid State Chemistry* **2002**, *164*, 332.

(17) Greedan, J. E. *Journal of Materials Chemistry* **2001**, *11*, 37.

(18) Ramirez, A. P. *Annual Review of Materials Science* **1994**, *24*, 453.

(19) Greedan; J.E. Raju; N. P. Wills; A. S.Morin; C. Shaw; S.M. Reimers; J. N. *Chemistry of Materials* **1998**, *10*, 3058.

(20) Sun, Y. K. *Journal of Power Sources* **1999**, *83*, 223.

(21) Conder, K.; Pomjakushina, E.; Soldatov, A.; Mitberg, E. *Materials Research Bulletin* **2005**, *40*, 257.

(22) Amatucci, G. G.; Tarascon, J. M.; Klein, L. C. *Journal of Electrochemical Society* **1996**, *143*, 1114.

(23) Mohanty, D.; Gabrisch, H. *ECS Transactions* **2009**, *19*, 25.
(24) Ménétrier; M. Carlier; D. Blangero; M. Delmas; C. *Electrochemical and Solid-State Letters* **2008**, *11(11) A*, 779.
(25) Levasseur; S. Ménétrier; M. Suard; E. Delmas; C. *Solid State Ionics* **2000**, *128*, 11.
(26) Levasseur, S.; Menetrier, M.; Shao-Horn, Y.; Gautier, L.; Audemer, A.; Demazeau, G.; Largeteau, A.; Delmas, C. *Chemistry of Materials* **2003**, *15*, 348.
(27) Gabrisch, H.; Xing, Q. S*olid State Ionics* **2008**, *179*, 2104.
(28) Nekrasov, I. A.; Streltsov, S. V.; Korotin, M. A.; Anisimov, V. I. *Physical Review B* **2003**, *68*, 235113.
(29) Nagata, S.; Keesom, P. H.; Harrison, H. R. *Physical Review B* **1979**, *19*, 1633.
(30) Anderson, P. W. *Physical Review* **1950**, *79*, 350.
(31) Ikedo, Y.; Sugiyama, J.; Nozaki, H.; Itahara, H.; Brewer, J. H.; Ansaldo, E. J.; Morris, G. D.; Andreica, D.; Amato, A. *Physical Review B* **2007**, *75*, 054424.
(32) Pena, O.; Bodenez, V.; Guizouarn, T.; Meza, E.; Gautier, J. L. *Journal of Magnetism and Magnetic Materials* **2004**, *272*, E1579.

Chapter 3

Microstructure and Magnetic Behavior of Compounds in the Solid Solution System $Li[Ni_{1-x}Mn_x]O_2$ (x = 0.3, 0.5, 0.7)

Abstract

Layered transition metal oxides containing more than one transition element are considered for applications in electric vehicles. In these compounds new and improved properties may result from the combination of element specific properties. At the same time the arrangement of species within the transition metal layer is one aspect that may affect the Li intercalation behavior and hence the electrochemical properties. Here we present a microstructural study on a series of $Li[Ni_{1-x}Mn_x]O_2$ compounds where the oxidations state and arrangement of transition metal (TM) ions are characterized by SQUID magnetometry and selected area electron diffraction (SAED) Our results show that in-plane long-range ordering increases with Mn content and that Li/Ni interchange takes place in all powders but seems to be highest in Mn rich compositions. During chemical delithiation Li is removed from the TM layers leading to a decrease in percentage of long range ordering.

3.1 Introduction

The need for Li-insertion compounds with high power and energy density motivates efforts to replace the layered Li-insertion compounds $LiCoO_2$ and $LiNiO_2$ with layered compounds of the solid solution system $LiCoO_2$- $LiNiO_2$- $LiMnO_2$. It is known that $LiCoO_2$ is structurally instable when more than 0.5 Li is removed. And for $LiNiO_2$, with a high rechargeable capacity, is difficult to synthesize reliably without interchange of Li and Ni between their respective layers [1-5]. The presence of Ni ions in the Li layers lowers the electrochemical activity of $LiNiO_2$ and its poor thermal stability in the charged state prohibits its practical usage [1, 6, 7]. Substituting manganese ions for Ni in the parent $LiNiO_2$ dramatically increases the thermal stability making $LiNi_{0.5}Mn_{0.5}O_2$ a promising, inexpensive alternate positive electrode material to both $LiCoO_2$ and $LiNiO_2$ [8-10]. $LiNi_{0.5}Mn_{0.5}O_2$ is isostructural to $LiNiO_2$, it has $R\bar{3}m$ symmetry (space group 166), with Li in 3a sites and transition metal ions in 3b sites separated by cubic closed packed oxygen layers [11]. First principles calculations and X-ray absorption experiments (XANES) of $LiNi_{0.5}Mn_{0.5}O_2$ showed that Ni and Mn are in the +2 and +4 state respectively in the as synthesized state [12]. During electrochemical cycling Ni is the active ion while Mn remains in the +4 state contributing towards the stability of this compound. However due to the very similar ionic radii of Ni^{+2} and Li^{+} ions there is always the possibility of interchanging nickel and lithium ions between their crystallographic sites. This exchange has been linked to the formation of long range in-plane ordering in form of $\sqrt{3}a_{hex}$ x $\sqrt{3}a_{hex}$ supercells in the TM layer [13-15]. A variation of the nickel to manganese ratio will change the oxidation state of nickel or manganese ions which may affect the electrochemical behavior [16]. XANES experiments confirmed the presence of Ni^{+3} in the nickel rich compound $LiNi_{1-x}Mn_xO_2$ ($0 \leq x \leq 0.5$) [16]. At the same time different long range order schemes in the TM layer can be envisioned that do not require the exchange of Li and Ni ions between their respective layers. At Ni:Mn

ratios of 1:2, a honeycomb like long range order is feasible resulting in superlattice reflections corresponding to the $\sqrt{3}a_{hex}$ x $\sqrt{3}a_{hex}$ supercells observed in $LiNi_{0.5}Mn_{0.5}O_2$ (assuming a sufficient difference between the atomic scattering factors of the two elements). This arrangement is observed in the TM layer of Li_2MnO_3 where a monoclinic unit cell is used to describe ordering between Li and Mn ions (C2/m symmetry, but ABAB stacking along c-axis as compared to ABC in $LiCoO_2$) [17].

In this chapter, the microstructure of $LiNi_{1-x}Mn_xO_2$ having Ni to Mn ratios of 1:2, 1:1 and 2:1 (x = 0.3, 0.5, 0.7) are characterized to monitor the possible ordering mechanisms in the Ni rich and Mn rich compounds. Single crystal electron diffraction patterns were used to characterize long-range ordering and magnetic measurements to investigate the oxidation states of transition metal ions as well as magnetic interactions between them. While magnetic data is available on Ni-rich compositions $LiNi_{1-x}Mn_xO_2$ $(0 \leq x \leq 0.5)$ no information could be found on the Mn-rich side of the binary phase diagram $LiNiO_2$-$LiMnO_2$ [16]. In first part of this work, the pristine materials were characterized and in the second part, lithium deficient phases were studied in order to understand the structural changes after lithium deintercalation.

3.2 Experimental

$LiNi_{1-x}Mn_xO_2$ (x = 0.3, 0.5, 0.7) was prepared following a modified co-precipitation method reported in literature [11]. Appropriate amounts of $NiNO_3.6H_2O$ and $MnNO_3.4H_2O$ were weighed according to the respective molar ratios and dissolved in water to obtain clear solutions of 2 molar concentrations. After stirring for 10 - 15 minutes 100 ml of 2 M NaOH and 100 ml of 2 M NH_4OH were added and the mixtures were stirred in air for 24 hr at a temperature T ~ 40-50 ^oC. In the case of $LiNi_{0.3}Mn_{0.7}O_2$ the solutions were stirred under Ar atmosphere. The precipitates were filtered, dried over night, and ground to obtain precursors. The required amount

of $LiOH \cdot H_2O$ was added, the mixture was ground and pre-sintered at 873 °C for 12 hrs, followed by annealing at 1173 °C in air for 12 hrs. The as synthesized powders were chemically delithiated under Argon atmosphere at room temperature by using solutions of NO_2BF_4 (source: Sigma Aldrich, assay ≥ 95%) in acetonitrile as delithiating agent. The reaction was carried out by drop-wise addition of NO_2BF_4 solution over 90 minutes to $LiNi_{1-x}Mn_xO_2$ suspensions, followed by an additional 90 minutes of stirring.

3.3 Characterization

Quantitative analysis of Mn, Ni and Li content were carried through Inductive Coupled Plasma Mass Spectrometry (ICP-MS). The morphology of the obtained powders was observed by scanning electron microscopy (SEM) using a JEOL JSM Scanning Electron Microscope. X-ray diffraction spectra (XRD) were collected with an X'pert PRO diffractometer (Panalytical Instruments) operated at 40 kV and 40 mA current using Cu-Kα radiation. Silicon powder was used as an internal standard. Phase determination was carried out by comparing experimental spectra to simulated powder diffraction spectra obtained with the software "powder cell" and using unit cells published in literature [18]. Single crystal electron diffraction patterns were obtained using a JEOL 2010 Transmission Electron Microscope (TEM) operated at 200 kV. For comparison, electron diffraction patterns were simulated using the software desktop microscopist. Field cooled (FC) and zero field cooled (ZFC) magnetic measurements were performed on a superconducting quantum interface device (SQUID) magnetometer (MPMS-XL-7: Quantum Design) between 5 K and 300 K under a magnetic field H = 10 kOe. Magnetic moment versus magnetic field (M-H) curves were obtained at 5 K.

3.4 Results and discussion

3.4.1 Starting material

The compositions of the synthesized compounds obtained from ICP measurements are $Li_{1.02}Ni_{0.69}Mn_{0.29}O_2$, $Li_{0.99}Ni_{0.50}Mn_{0.52}O_2$ and $Li_{1.02}Ni_{0.30}Mn_{0.70}O_2$ confirming that the targeted Ni:Mn ratios have been realized. In Figure 3.1 comparison of the particle morphologies illustrates that large octahedral particles (≈ 2 μm) form in the Ni-rich material ($LiNi_{0.7}Mn_{0.3}O_2$) whereas smaller irregularly shaped particles are observed in $LiNi_{0.5}Mn_{0.5}O_2$ and $LiNi_{0.3}Mn_{0.7}O_2$. The X-ray diffraction spectra of the synthesized powders are shown in Figure 3.2. All materials can be indexed in the α-$NaFeO_2$ structure and exhibit typical characteristics of a layered material: clear splitting of (006)/(012) and (108)/(110) doublets and an intensity ratio I_{003} /I_{104} larger than one [3, 19]. The approximate *c* and *a* lattice parameter estimated from (003) and (110) peak positions take on the largest and smallest values in $LiNi_{0.5}Mn_{0.5}O_2$ and $LiNi_{0.3}Mn_{0.7}O_2$ respectively (a = 2.88 Å, c = 14.33 Å compared to a = 2.86 Å, c = 14.28 Å). The increase in lattice parameters with decreasing Ni-content observed between $LiNi_{0.7}Mn_{0.3}O_2$ and $LiNi_{0.5}Mn_{0.5}O_2$ is in agreement with observations published by Kobayashi et al. [16]. In the Mn rich small additional diffraction peaks are observed in the 2-theta range of 20^o - 35^o. In the Mn-rich compound, these are in agreement with superstructure peaks resulting from in plane ordering in a $\sqrt{3}a_{hex}$ x $\sqrt{3}a_{hex}$ supercell that can be indexed either in a monoclinic unit cell (C2/m) or in a trigonal unit cell ($P3_112$) [17,20]. The positions of the superstructure peaks are marked by dots in Figure 3.2. The presence of superstructure peaks were in agreement with the analysis of single crystal electron diffraction patterns where maximum long range ordering was observed for manganese-rich phase presented below. Before discussing the single crystal diffraction data the results of magnetic measurements are presented in order to assign the oxidation states of transition metal ions.

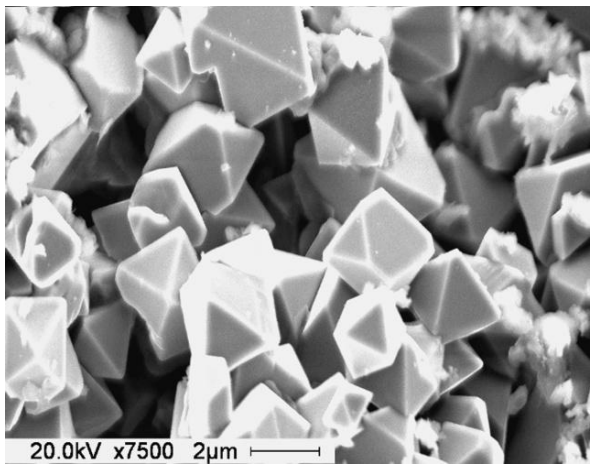

(a)

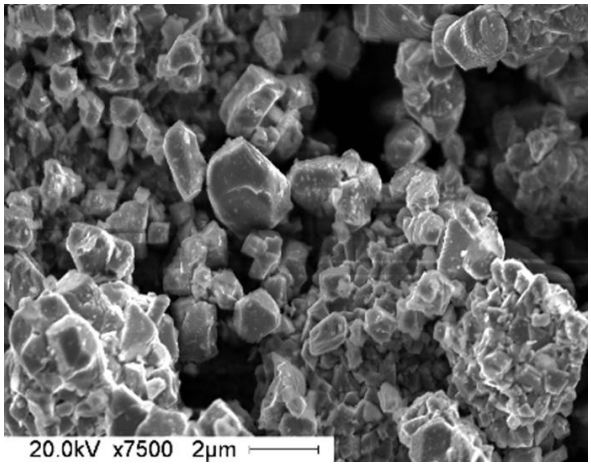

(b)

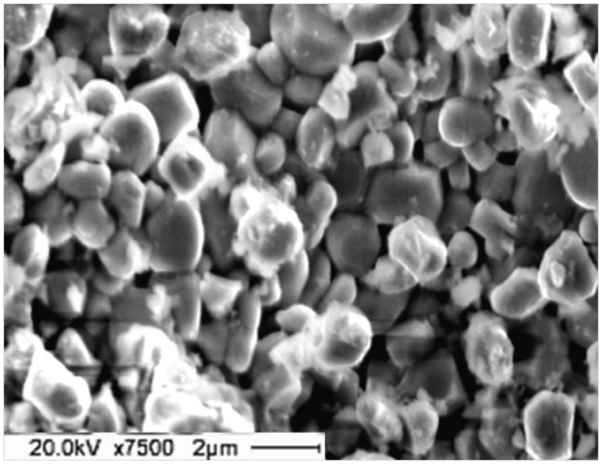

(c)

Figure 3.1 Scanning electron micrographs of $LiNi_{1-x}Mn_xO_2$: (a.) x = 0.3 (b), x = 0.5, (c) x = 0.7.

In Figure 3.3 temperature dependence of the molar magnetic susceptibility is shown for experiments under field cooling (FC) and zero field cooling (ZFC). All the materials show paramagnetic behavior at high temperatures ($T \geq 150$ K) and an increase in magnetic susceptibility in the lower temperature region. The FC and ZFC curves are identical for $LiNi_{0.5}Mn_{0.5}O_2$ and for the Mn-rich compound. In the case of the Ni-rich composition the FC and ZFC curves bifurcate at T = 30 K indicating the presence of magnetic frustration in the lattice which can be classified as

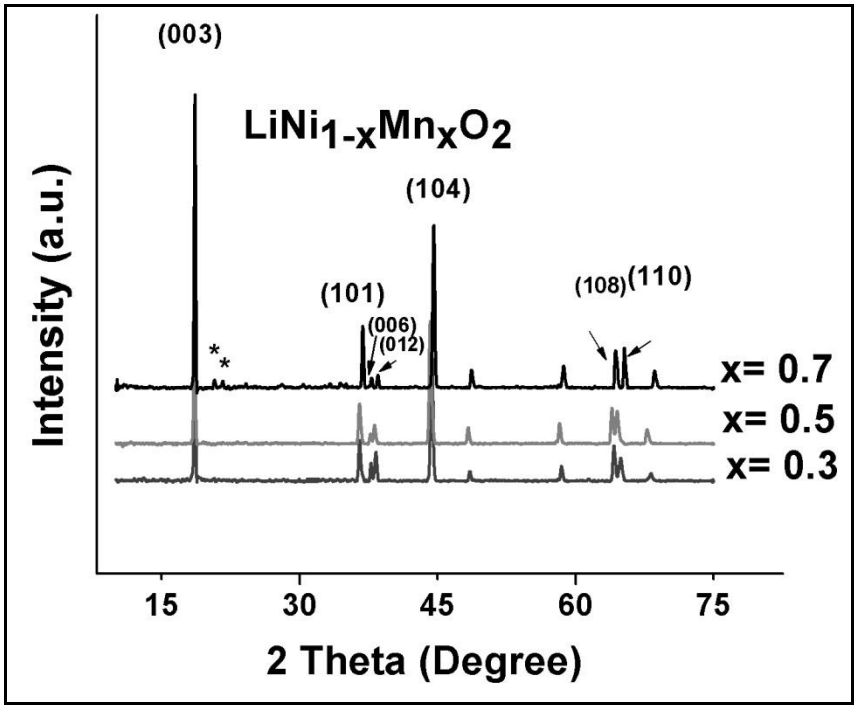

Figure 3.2 X-ray diffraction pattern of $LiNi_{1-x}Mn_xO_2$ (x = 0.3, 0.5, 0.7) before chemical delithiation

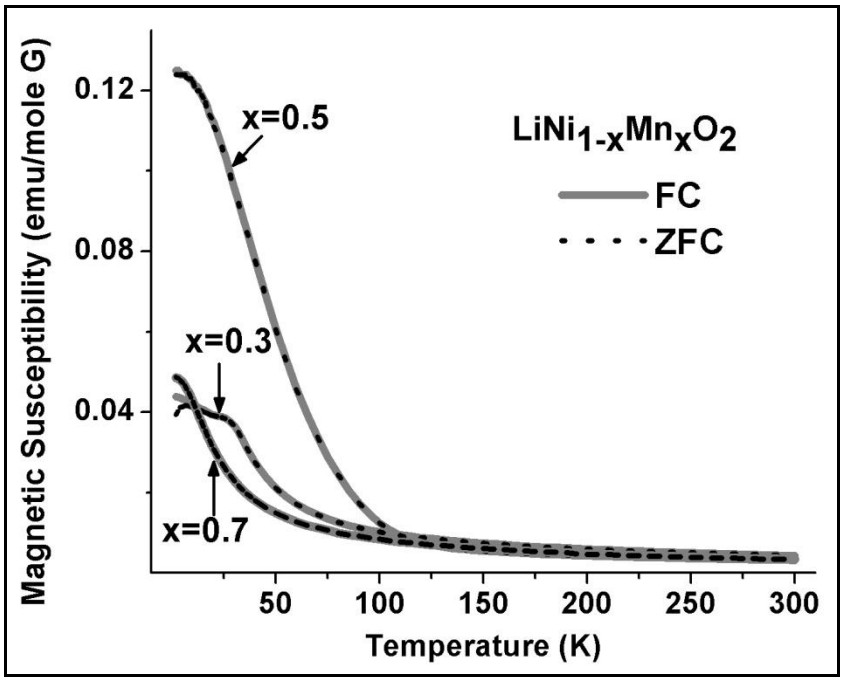

Figure 3.3 Variation of molar magnetic susceptibility versus temperature for $LiNi_{1-x}Mn_xO_2$ before chemical delithiation

spin-glass-like behavior or geometrical frustration [21]. Spin-glass-like behavior has been observed in $LiNiO_2$ has been linked to the presence of Ni^{+2} ions in the lithium layer [22]. The effective magnetic moments were calculated for each compound from a plot of inverse susceptibility versus temperature in the temperature region 150 - 300 K (see Table 1). The experimental values were compared to theoretical values based on combinations of Ni^{3+}/Mn^{3+} (all three compounds), $Ni^{+2}/Ni^{+3}/Mn^{+4}$ (Ni-rich) or $Ni^{+2}/Mn^{+3}/Mn^{+4}$ (Mn-rich) ions in high- and low-spin configurations. The best fit between experimental and theoretical effective magnetic moment for each composition is listed in Table 1. It can be seen that $LiNi_{0.5}Mn_{0.5}O_2$, $LiNi_{0.7}Mn_{0.3}O_2$, and $LiNi_{0.3}Mn_{0.7}O_2$ are best represented as $LiNi_{0.5}{}^{+2}Mn_{0.5}{}^{+4}O_2$, $LiNi_{0.3}{}^{+2}Ni_{0.4}{}^{+3}Mn_{0.3}{}^{+4}O_2$ and $LiNi_{0.3}{}^{+2}Mn_{0.4}{}^{+3}Mn_{0.3}{}^{+4}O_2$, respectively. In the case of $LiNi_{0.5}Mn_{0.5}O_2$ and the Ni-rich compound $LiNi_{0.7}Mn_{0.3}O_2$ the results are in agreement with

literature reports based on theoretical and EXAFS studies [15,16]. However no reports could be found for the Mn-rich material. The experimental effective magnetic moment for Mn-rich material is $3.06\mu_B$ which is close to the theoretical effective magnetic moment value resulting from 0.3 mol of Ni^{+2}, 0.3 mol of Mn^{+4} and 0.4 mol of Mn^{+3} (high spin). A model assuming 0.3 mol of Ni^{+3} (high spin) and 0.7 mol of Mn^{+3} (high spin) can be rejected as the X-ray diffraction and the electron diffraction analysis (below) reveal a high percentage of long range ordering involving among the Li^+ ions and Ni^{+2} ions and/or Mn^{+4} ions. Taking the assigned charges into account the magnetic frustration in the nickel rich material can be explained as follows. The nickel rich material contains Ni^{2+} and Ni^{3+} ions along with Mn^{4+} ions. The ionic radius of Ni^{2+} (0.69 Å) is very much similar to the Li^+ ion (0.76 Å) opening a possibility of interchange between Ni^{2+} ions present in the transition metal (TM) layer and Li^+ ion in lithium layer. Based on the Goodenough's theory, the presence of Ni^{2+} ions in the lithium layer then introduces antiferromagnetic coupling with Ni^{3+} ions in the TM layer via 180^o exchange interaction along the Ni^{2+}-O-Ni^{3+} path as well as ferromagnetic coupling with Mn^{4+} ions in the TM layer via a 180^o Ni^{2+}-O-Mn^{4+} path [23]. These interactions create magnetic frustration between Ni^{+2}, $Ni^{+3,}$ and Mn^{4+} in the triangular lattice among these ions (Figure 3.5) which is seen in magnetic susceptibility versus temperature curve (Figure 3.3). The effect of competing ferro- and anti-ferromagnetic interactions can also be seen the magnetization curves collected at 5 K where hysteresis behavior is observed for $LiNi_{0.5}Mn_{0.5}O_2$ and for the Ni rich material, see Figure 3.4.

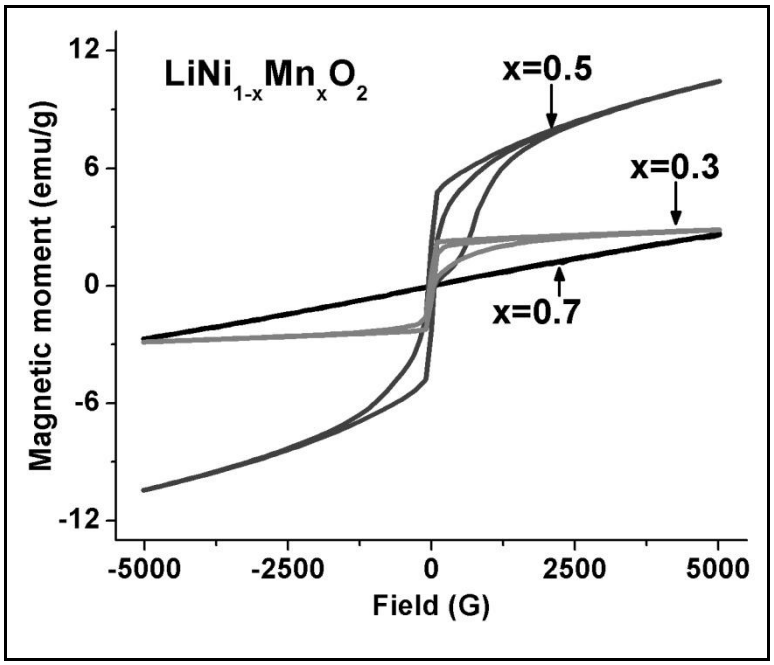

Figure 3.4 Magnetic moment (M) and Field (H) plots of $LiNi_{1-x}Mn_xO_2$

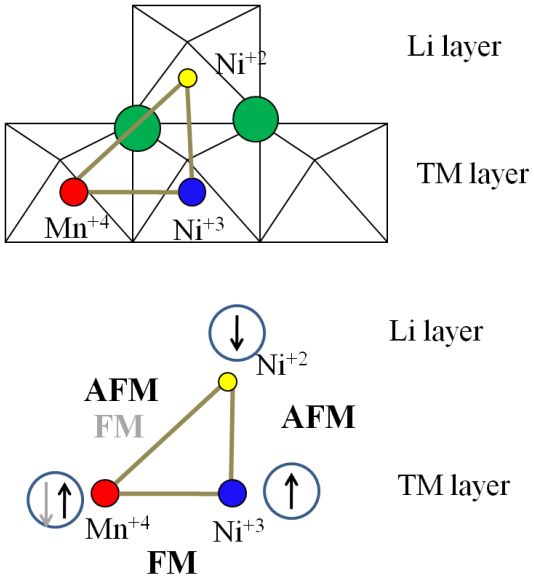

Figure 3.5 Magnetic model explaining the magnetic frustration in Ni rich compound.

The hysteresis behavior for $LiNi_{0.5}Mn_{0.5}O_2$ is due to the strong 180^o Ni^{+2} (lithium layer)-O-Ni^{+2} (TM layer) ferromagnetic coupling present in this material as reported by several authors [16, 24]. In the case of Ni-rich material the hysteresis is less pronounced than in $LiNi_{0.5}Mn_{0.5}O_2$ which indicates the presence of AFM interaction present in the lattice. In case of the Mn-rich compound ($LiNi_{0.3}Mn_{0.7}O_2$) purely paramagnetic behavior is observed without any hysteresis character.

Table3.1 Comparison between experimental and theoretical magnetic moment of starting material (best fit of theoretical values shown).

Starting material			
composition	**μ_{exp}**	**Model**	**μ_{theo}**
$Li_{1.02}Ni_{0.69}Mn_{0.29}O_2$	3.54 μ_B	$0.3Ni^{+2}$, $0.4Ni^{+3}$, $0.3Mn^{+4}$	3.56 μ_B
$Li_{0.99}Ni_{0.50}Mn_{0.52}O_2$	3.11 μ_B	$0.5Ni^{+2}$, $0.5Mn^{+4}$	3.35 μ_B
$Li_{1.02}Ni_{0.30}Mn_{0.70}O_2$	3.06 μ_B	$0.3Ni^{+2}$, $0.4Mn^{+3}$, $0.3Mn^{+4}$	3.14 μ_B

Single crystal electron diffraction patterns were taken from 15 particles of each material and were classified into the following categories:

O3 - Diffraction patterns showing no superlattice reflections are assumed to represent random TM arrangement and are labeled O3 type patterns following the notation for LiCoO2 in a trigonal unit cell (space group 166), an example is shown in Figure 3.6a. The reflections in these patterns are called fundamental reflections. When TM and Li ions are arranged in an ordered fashion within the oxygen framework additional (superlattice) reflections may appear.

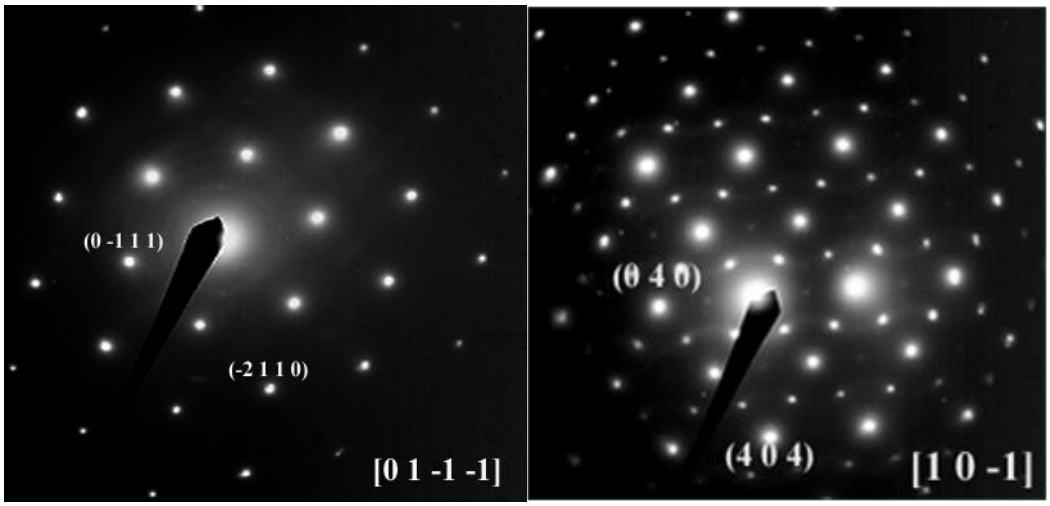

Figure 3.6 Example of electron diffraction pattern showing O3 (a) and spinel reflections (b).

Spinel - In a cubic spinel (space group 225) TM and Li ions occupy layers of interstitial sites in alternating ratios of 1:3 assigned to lattice sites 16d and 8a in superlattice reflections are observed halfway between fundamental reflections, an example is shown in Figure 3.6b.

$\sqrt{3}a_{hex}$ x $\sqrt{3}a_{hex}$ R30^{o} type of ordering and C2/m - Long range order within the TM layer can be observed when 2 or more species are present. In case of Li_2MnO_3 ($Li[Li_{1/3}Mn_{2/3}]O_2$) a honeycomb structure is formed that has been described in literature in a C2/m notation [25]. Here superlattice reflections divide the distance between fundamental reflections into three, corresponding to a threefold increase of the unit cell dimensions with respect to distances between oxygen atoms in the O3 structure. The large difference in atomic scattering factor between Li and Mn lends a strong intensity to the observed superlattice diffractions. Similarly superlattice reflections corresponding to a threefold increase of the in-plane unit cell can be observed when three species are ordered in a regular arrangement within the TM layer as

described by Ohzuku et al. in a trigonal lattice ($P3_112$) [20]. Here the small difference in atomic scattering factor should result in lower intensity of the observed superlattice reflections. In the case of $LiNi_{0.5}Mn_{0.5}O_2$ the $\sqrt{3}a_{hex}$ x $\sqrt{3}a_{hex}$ $R30^o$ in plane ordering results from Li/Ni exchange where the replacement of some Ni with Li in the TM layer introduces local variations of cations arrangement as described by Meng *et al.* [13]. The two crystal structures used to describe the cation's arrangement differ in the oxygen stacking that is cubic close packed in the trigonal model compared to hexagonal close packed (AB stacking) in the monoclinic structure. The oxygen lattice in the monoclinic structure is slightly distorted, which is accounted for by the monoclinic angle. Only patterns that unambiguously fit into the monoclinic category are labeled C2/m. Examples for the monoclinic structure and $\sqrt{3}a_{hex}$ x $\sqrt{3}a_{hex}$ $R30^o$ type ordering are shown in Figure 3.7 a,b.

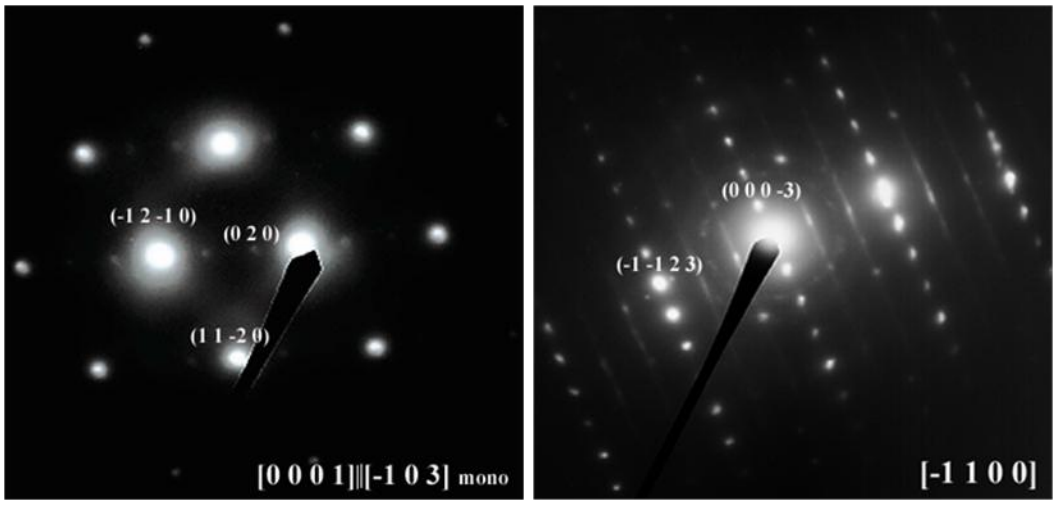

Figure 3.7 Example of electron diffraction pattern showing monoclinic (a) and $\sqrt{3}a_{hex}$ x $\sqrt{3}a_{hex}$ $R30^o$ type ordering reflections (b).

A summary of the analysis results is presented in Table 2. Comparison shows that the Ni-rich system does not show in-plane ordering (14 out of 15 particles indexed as O3) whereas the

highest percentage of in-plane ordering is observed in the Mn-rich compound (10 out of 15 particles). Small amounts of spinel phase and O3 type diffraction patterns are found in $LiNi_{0.5}Mn_{0.5}O_2$ and in the Mn-rich compound, and in $LiNi_{0.5}Mn_{0.5}O_2$ a small amount of the monoclinic phase was observed. The absence of long range order in the Ni-rich system is in contrast to the exchange of Ni^{2+} and Li^+ ions between their respective layers. It is concluded that the extent of Ni^+ /Li^+ exchange is minor and the number of Li-ions in the TM layer is insufficient to create a $\sqrt{3}a_{hex}$ x $\sqrt{3}a_{hex}$ R30^o type long range in-plane ordering. This argument is supported by results published by Kobayashi *et al*. who studied the Ni-rich side of the series $LiNi_{1-x}Mn_xO_2$ (x= 0.1-0.5). The authors confirmed that the least Ni/Li exchange is observed in nickel-rich material and that the amount of exchange increases with manganese ion content [16]. In $LiNi_{0.5}Mn_{0.5}O_2$ the interchange between Ni^{2+} in the TM layer and Li^+ in the lithium layer creates the ordering between (Li^+, Ni^{2+}) and Mn^{4+} in the TM layer which generates the $\sqrt{3}a_{hex}$ x $\sqrt{3}a_{hex}$ R30^o superstructure as

Table 3.2: Classification of diffraction patterns obtained from the as-synthesized powders (15 particles analyzed per sample).

Diffraction type	$LiNi_{0.7}Mn_{0.3}O_2$	$LiNi_{0.5}Mn_{0.5}O_2$	$LiNi_{0.3}Mn_{0.7}O_2$
O3	14 (93%)	3 (20%)	2 (13 %)
Spinel	1 (7%)	2 (13%)	3 (20%)
monoclinic		2 (13%)	
$\sqrt{3}a_{hex}$ x $\sqrt{3}a_{hex}$ R30^o		8 (54%)	10 (67%)

previously reported by other authors [13]. In the Mn-rich compound long range in-plane ordering may be the result of a honeycomb arrangement formed of Ni and Mn ions comparable to the ordering observed in Li_2MnO_3. Alternatively it may involve Li/Ni interchange as described above for $LiNi_{0.5}Mn_{0.5}O_2$. Assuming that superlattice reflections of sufficient intensity require the presence of Li in the TM layer it follows that the Li/Ni interchange is the highest in the Mn rich material where the largest percentage of in plane ordering is observed. This follows the trend mentioned above for a decrease in Li/Ni interchange in Ni-rich $LiNi_{1-x}Mn_xO_2$ (x = 0.1 - 0.5) [16]. A possible explanation for this behavior can be found from a comparison between electron densities around Ni^{3+} in Ni-rich compounds and Mn^{3+} in Mn compounds. The electron density of Mn^{3+} ions is higher than that of Ni^{3+} ions, resulting in higher repulsion between Mn^{3+} and Ni^{2+} ions in the TM layer of manganese rich material. This may be the driving force for the higher Ni^{2+} / Li^+ (lithium layer) exchange, which introduces the $\sqrt{3}a_{hex}$ x $\sqrt{3}a_{hex}$ R30^o in-plane ordering in $LiNi_{0.3}Mn_{0.7}O_2$ observed here. The assumption that Li/Ni exchange plays a role in long range

ordering observed in the manganese-rich composition is confirmed by the high intensity of superlattice reflections observed in $LiNi_{0.3}Mn_{0.7}O_2$ compared to those observed in $LiNi_{0.5}Mn_{0.5}O_2$ (compare Figure 3.8a to b).

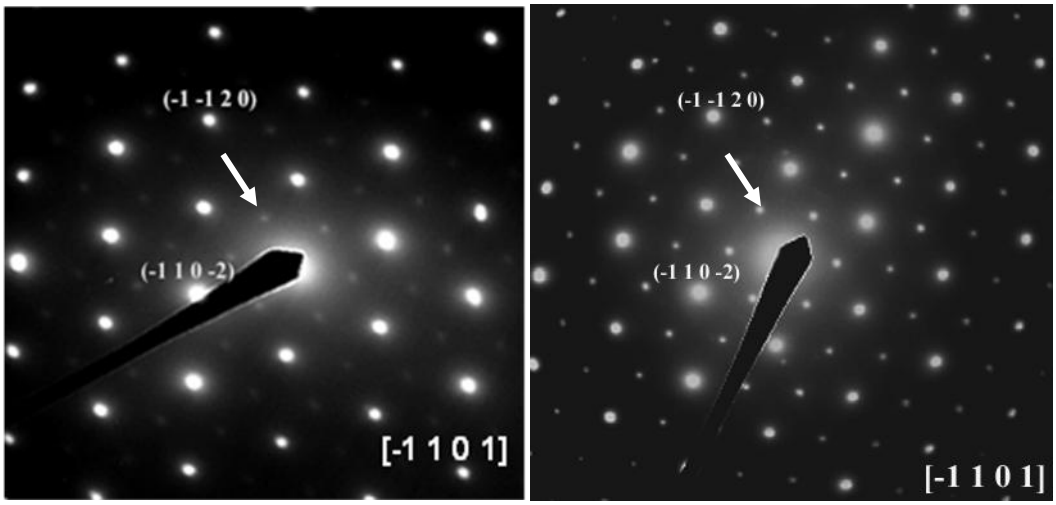

Figure 3.8 Example of electron diffraction pattern of starting material of $LiNi_{0.5}Mn_{0.5}O_2$ (a) and $LiNi_{0.3}Mn_{0.7}O_2$ (b) showing reflections having $\sqrt{3}a_{hex}$ x $\sqrt{3}a_{hex}$ type of ordering (highlighted by arrows)

3.4.2 Delithiated materials:

During chemical delithiation about 0.12 - 0.14 Li was extracted from the synthesized powders and the resulting compositions measured by ICP are $Li_{0.88}Ni_{0.68}Mn_{0.29}O_2$, $Li_{0.86}Ni_{0.48}Mn_{0.53}O_2$, and $Li_{0.87}Ni_{0.31}Mn_{0.65}O_2$. The corresponding X-ray diffraction patterns in Figure 3.9 show the following trends: The intensities of superlattice peaks for delithiated Mn rich material are lower than those observed in the Mn-rich starting material, indicating that lithium ions have been extracted from the transition metal layers thereby reducing in long range ordering. In the Ni-rich material the splitting between (110) and (018) doublet has decreased and the (006) peaks has disappeared, corresponding to formation of some spinel phase. No major change was observed in the X-ray diffraction spectrum $Li_{0.88}Ni_{0.5}Mn_{0.5}O_2$.

A summary of the analysis of electron diffraction pattern taken from 15 particles of the delithiated compounds is given in Table 3.3. A comparison to the relative amounts observed in the starting material shows that the percentage of in-plane ordering has decreased in the Mn-rich compound and in $Li_{0.87}Ni_{0.5}Mn_{0.5}O_2$. Furthermore the intensity of superlattice diffractions in the Mn-rich compound is weak compared to the intensity observed in the starting material. This

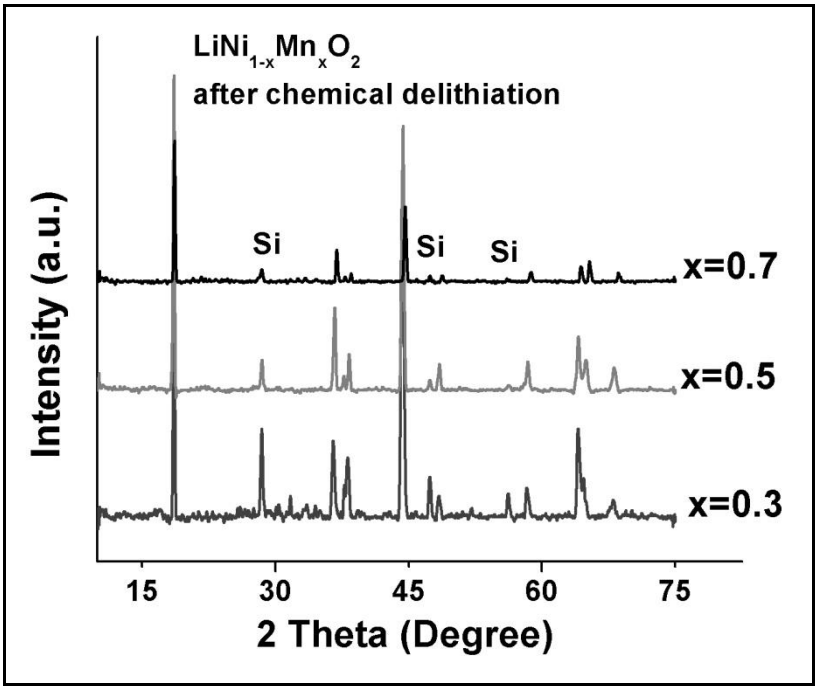

Figure 3.9 X-ray diffraction pattern of $LiNi_{1-x}Mn_xO_2$ (x = 0.3, 0.5, 0.7) after chemical delithiation

indicates that less lithium is present in the transition metal layers compared to the starting material and that during chemical delithiation lithium is extracted from the TM layers. In the Ni-rich material an increase in ordering is observed in the form of spinel formation and formation of a monoclinic phase.

Table 3.3 Classifications of diffraction patterns obtained from lithium deficient material in the series $LiNi_{1-x}Mn_xO_2$ (x = 0.3, 0.5, 0.7) [15 particles of each analyzed].

Diffraction type	$Li_{0.88}Ni_{0.68}Mn_{0.29}O_2$	$Li_{0.86}Ni_{0.48}Mn_{0.53}O_2$	$Li_{0.87}Ni_{0.31}Mn_{0.65}O_2$
O3	8 (53%)	4 (27%)	3 (20%)
O3+extra reflection	-	1(6%)	-
Spinel	4 (27%)	3 (20%)	2 (13%)
Monoclinic	3 (20%)	2 (13%)	3 (20%)
$\sqrt{3}a_{hex}$ x $\sqrt{3}a_{hex}$ R30^o	-	5 (33%)	7 (47%)

The magnetic behavior of the delithiated powders shows similar trends as the starting material, with the exception of the Ni-rich compound. Here the magnetic frustration behavior observed in the starting material has vanished after Li-extraction. In Figure 3.10 the variation of molar magnetic susceptibility values with the temperature is shown in FC and ZFC mode. The FC and ZFC curves are similar for all the materials showing paramagnetic behavior in the high temperature region ($T \geq 150$ K) and increased magnetic susceptibility at lower temperature. The effective magnetic moments calculated from the plot of inverse susceptibility over temperature are given in Table 3.4. The values are lower than those measured in the starting material, see Table 3.1. To decide which ion compensates the charge upon Li-extraction in each compound we calculated the theoretical effective magnetic moment considering oxidation of Ni^{2+}, Ni^{3+} or

Mn^{3+}. The removal of 0.12 Li from $LiNi^{2+}_{0.5}Mn^{4+}_{0.5}O_2$ requires either oxidization of (i) 0.12mol of Ni^{+2} to Ni^{+3} (HS/LS) or (ii) 0.06 mol Ni^{+2} are oxidized to Ni^{+4} (HS/LS).

Table 3.4 Comparison between experimental and theoretical magnetic moment of delithiated materials (best fit of theoretical values shown).

Delithiated material			
$Li_{0.88}Ni_{0.68}Mn_{0.29}O_2$	2.50 μ_B	$0.3Mn^{4+}$, $0.16Ni^{2+}$, $0.54Ni^{3+}$ (LS) $0.3\ Mn^{4+}$, $0.26Ni^{3+}$ (LS), $0.3Ni^{2+}$, Ni^{4+} (LS)	2.55 μ_B 2.46 μ_B
$Li_{0.86}Ni_{0.48}Mn_{0.53}O_2$	3.05 μ_B	$0.44Ni^{2+}$,$0.06Ni^{4+}$,$0.5Mn^{4+}$	3.08 μ_B
$Li_{0.87}Ni_{0.31}Mn_{0.65}O_2$	3.03 μ_B	$0.17Ni^{+2}$, $0.13Ni^{+3}$(LS), $0.4Mn^{+3}$(LS),$0.3Mn^{+4}$ $0.235Ni^{+2}$, $0.065Ni_{+4}$(LS), $0.3Mn^{+4}$, $0.4Mn^{+3}$(LS)	2.99 μ_B 2.96 μ_B

The resulting compositions are (i) $Li^{+}_{0.88}Ni^{2+}_{0.38}Ni^{3+}_{0.12}Mn^{4+}_{0.5}O_2$ and (ii) $Li^{+}_{0.88}Ni^{2+}_{0.44}Ni^{4+}_{0.06}Mn^{4+}_{0.5}O_2$. A comparison between the experimentally determined effective magnetic moment ($3.05\mu_B$) to the values determined for the two models shows that Ni^{+2} is oxidized to Ni^{+4} upon Li extraction from. Model (i) yields a theoretical effective magnetic moment of 3.22 μ_B compared to 3.08 μ_B for model (ii). Similar considerations for the Ni-rich and the Mn rich compounds do not yield unambiguous results. In the Ni-rich material an experimental effective magnetic moment of 2.50 μ_B is measured. This compares to a best theoretical value of 2.55 μ_B for oxidation of Ni^{2+} to Ni^{3+} (LS) or of 2.46 μ_B for oxidation of Ni^{3+} to Ni^{4+}. The oxidation of Ni^{2+} to Ni^{4+} can be excluded based on the larger discrepancies between

theoretical and experimental values (closest fit: 2.55 μ_B and 2.50 μ_B). For comparison in the Mn rich material the oxidation of Ni^{2+} to Ni^{3+} or to Ni^{4+} yields similar theoretical effective magnetic moments. 3.00 μ_B and 2.96 μ_B are calculated for Ni^{2+} (LS) $\rightarrow$ Ni^{3+} (LS) for Ni^{2+} (LS) $\rightarrow$ Ni^{4+} (LS) respectively compared to an experimental value of 3.03 μ_B. Here the oxidation of Mn^{3+} can be excluded.

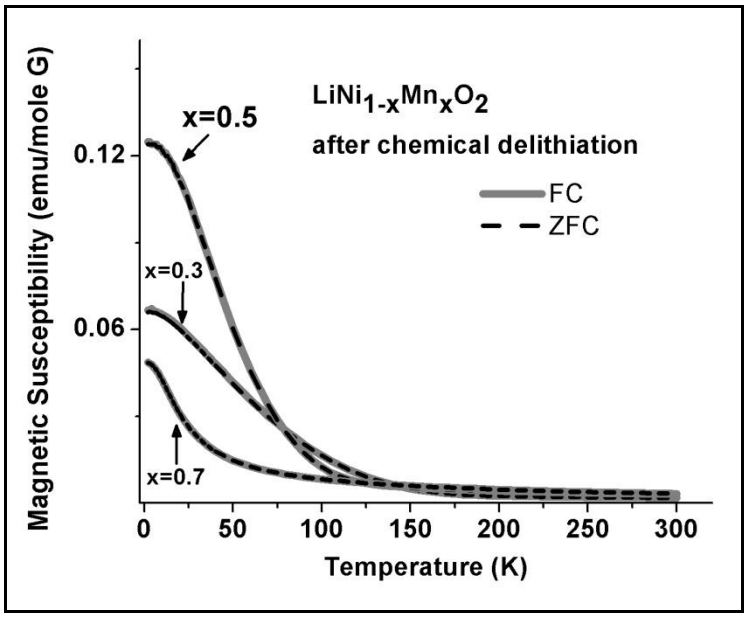

Figure 3.10 Variation of molar magnetic susceptibility versus temperature for $LiNi_{1-x}Mn_xO_2$ after chemical delithiation.

3.5 Conclusions

Compounds in the layered series $LiNi_{1-x}Mn_xO_2$ (x = 0.3, 0.5, 0.7) were synthesized and characterized by powder and single crystal diffraction methods as well as magnetic measurements with superstructure peaks were observed in the manganese rich phase. Comparison between theoretical models and experimentally determined effective magnetic moment indicates that Ni and Mn ions take on +2 and +4 oxidation states when present in a 1:1

ratio. In Ni-rich or Mn- rich compounds the extra Ni or Mn ions are observed in +3 oxidation states. Upon Li-extraction Ni^{2+} is oxidized to Ni^{4+} in $LiNi_{0.5}Mn_{0.5}O_2$. In all as synthesized materials exchange between Li^+ and Ni^{2+} is observed that results in in-plane $\sqrt{3}a_{hex}$ x $\sqrt{3}a_{hex}$ $R30^o$ long range order in $LiNi_{0.5}Mn_{0.5}O_2$ and in the Mn-rich compound but not in the Ni-rich compound. However the observed magnetic frustration in $LiNi_{0.7}Mn_{0.3}O_2$ indicates that Ni^{2+} ions are present in the Li layer here as well. After Li-extraction the magnetic frustration disappeared in the Ni-rich phase while the percentage of long range order decreased in $LiNi_{0.5}Mn_{0.5}O_2$ and in the Mn-rich phase indicating that Li has been extracted predominantly from the TM layer.

3.6 References

[1] O. J. Besenhard, "Handbook of Battery Materials." Wiley-VCH, New York, 1999.

[2] J. M. Paulsen, C. L. Thomas, and J. R. Dahn, Journal of Electrochemical Society **146**, 3560 (1999).

[3] J. R. Dahn, U. v. Sacken, and M. C.A., Solid State Ionics **44**, 87 (1990).

[4] R. Kanno, H. Kubo, Y. Kawamoto, T. Kamiyama, F. Izumi, T. Y., and M. Takano, Journal of Solid State Chemistry **11**, 216 (1994).

[5] H. Arai, S. Okada, H. Ohtsuka, M. Ichimura, and J. Yamaki, Solid State Ionics **8**, 261 (1995).

[6] A. Hirano, R. Kanno, Y. Kawamoto, T. Y., K. Yamaura, M. Takano, K. Ohyama, M. Ohashi, and Y. Yamaguchi, Solid State Ionics **78**, 123 (1995).

[7] L. Coguennec, C. Pouillerie, A. N. Masour, and C. Delmas, Journal of Materials Chemistry **11**, 131 (2001).

[8] N. Yabuuchi, Y. T. Kim, H. H. Li, and Y. Shao-Horn, Chemistry of Materials **20**, 4936 (2008).

[9] T. Ohzuku and Y. Makimura, Chemistry Letters **8**, 744 (2001).

[10] Z. Lu, D. D. Macneil, and J. R. Dahn, Electrochemical and Solid-State Letters **4**, A191 (2001).

[11] Y. Arachi, H. Kobayashi, S. Emura, Y. Nakata, M. Tanaka, and T. Asai, Chemistry Letters **32**, 60 (2003).

[12] J. Reed and G. Ceder, Electrochemical and Solid-State Letters **5**, A145 (2002).

[13] Y. S. Meng, G. Ceder, C. P. Grey, W.-S. Yoon, and Y. Shao-Horn, Electrochemical and Solid-State Letters **7**, A155 (2004).

[14] Y. S. Meng, G. Ceder, C. P. Grey, W.-S. Yoon, M. Jiang, J. Breger, and Y. Shao-Horn, Chemistry of Materials **17**, 2386 (2005).

[15] Y. Koyama, Y. Makimura, I. Tanaka, H. Adachi, and T. Ohzuku, Journal of Electrochemical Society **151**, A1499 (2004).

[16] H. Kobayashi, H. Sakaebe, H. Kageyeyama, K. Tatsumi, Y. Arachi, and T. Kamiyama, Journal of Materials Chemistry **13**, 590 (2003).
[17] J. Breger, M. Jiang, N. Dupre, Y. S. meng, Y. Shao-Horn, G. Ceder, and C. P. Grey, Journal of Solid State Chemistry **178**, 2575 (2005).
[18] H. Gabrisch, T. Yi, and R. Yazami, Electrochemical and Solid-State Letters **11**, A119 (2008).
[19] J. Morales, C. Perez-vicenet, and J. L. Tirado, Materials Research bulletin **623** (1990).
[20] Y. Koyama, N. Yabuuchi, I. Tanaka, H. Adachi, and T. Ohzuku, Journal of Electrochemical society **151**, A1545 (2004).
[21] S. Nagata, P. H. Keesom, and H. R. Harrison, Physical Review B **19**, 1633 (1979).
[22] A. Rougier, C. Delmas, and G. Chouteau, Journal of Physics and Chemistry of Solids **57**, 1101 (1996).
[23] J. B. Goodenough, Physical Review **117**, 1442 (1960).
[24] N. A. Chernova, M. MA, J. Xiao, M. S. Whittingham, J. Breger, and C. P. Grey, Chemistry of Materials **19**, 4682 (2007).
[25] C. H. Lei, J. G. Wen, M. Sardela, J. Bareno, I. Petrov, S.-H. Kang, and D. P. Abraham, Journal of Materials Science **44**, 5579 (2009).

Chapter 4

Magnetic properties and microstructural investigation of $LiNi_{1/3}Mn_{1/3}Co_{1/3}O_2$ and its aged products

Abstract

The performance of $LiNi_{1/3}Mn_{1/3}Co_{1/3}O_2$ depends largely on the distribution of transition metal ions over the available lattice sites within the layered rock salt structure. Despite of this, there is always a prediction that the Ni^{+2} ions and Li^{+} ions exchange their crystallographic sites due to very similar ionic radii which introduces in-plane ordering in the transition metal layers. This in-plane cation ordering generally decreases the electrochemical activity in the battery. Here By using magnetic measurements and selected area electron diffraction studies, the cationic ordering was investigated in the $LiNi_{1/3}Mn_{1/3}Co_{1/3}O_2$ which was synthesized at 850 °C and also in its lithium deficient product before and after thermal ageing with respect to time in order to monitor the microstructural changes in these materials. The result showed that the change in morphology of the particles including the significant microstructure changes in the samples which was aged for linger time. In all the materials in-plane ordering was not detected in both magnetic and electron diffraction studies.

4.1 Introduction

Over the last few years, the ternary transition metal oxide $LiNi_{1/3}Mn_{1/3}Co_{1/3}O_2$ has developed into a strong candidate for applications in high power rechargeable Li-ion batteries, due to its superior thermal stability and reversible capacity compared to its $LiCoO_2$ counterpart.[1-3] It has high reversible capacity of 160 mAh/g in the cut-off voltage range of 2.5 - 4.4 V and 200 mAh/g in 2.8 - 4.6 V which makes this material very promising cathode for high power and high energy Li-ion batteries to be used in hybrid electric vehicles (HEVs).[4] $LiNi_{1/3}Mn_{1/3}Co_{1/3}O_2$ adopts the typical-α-$NaFeO_2$ structure described by the $R\bar{3}m$ space group which is formed by edge sharing MO_6 octahedra [M= Co, Mn, Ni] separated by lithium ions occupying interstitial octahedral sites.[5] The transition metal ions play significant roles towards the stability and electrochemical activity in this compound. Nickel (Ni^{+2}) is the electrochemical active species, manganese (Mn^{+4}) provides structural stability whereas cobalt (Co^{+3}) supports ordering of lithium and nickel ions onto their respective lattice sites. However, due to the similar ionic radii of Ni^{+2} (0.67 Å) and Li^{+} (0.76 Å) there is always a chance to exchange the crystallographic sites between these two ions.[6] This is a significant drawback of this highly efficient cathode since this interchange between the lattice sites decreases the electrochemical activity[7] because the Ni^{+2} present in the lithium sites oxidized to Ni^{+3} early before lithium removal and the Ni^{+3} distorts the lithium layers impeding the lithium diffusion. The Li^{+}/Ni^{+2} lattice site interchange eventually initiates the possibility of different cation ordering schemes in the transition metal layers which also affects the structural stability. Experimental evidence for in-plane ordering has been observed by Yabuuchi et al. who reported superlattice reflections in pristine material corresponding to $\sqrt{3}$ x $\sqrt{3}$ $R30^o$ in plane unit cell.[4] On the other hand, neutron diffraction and X-ray powder diffraction data shows random distribution of Mn, Ni, Co over 3a sites in the $R\bar{3}m$

structure[8]. Furthermore the exchange of Li^{+} and Ni^{+2} ions between their respective crystallographic layers introduce local disorder that also decreases the electrochemical performance.[9] Therefore, the cation ordering plays an important role to determine the electrochemical activity as well as stability of $LiNi_{1/3}Mn_{1/3}Co_{1/3}O_2$ materials. Although the previous literatures which describe the cation ordering in this material, but there are, still open questions regarding the cationic ordering in this ternary cathode material which should be addressed in order to improve the structural stability as well as electrochemical activity. Previously, in one of our studies, we reported the systematic study on the cationic ordering in commercial $LiNi_{1/3}Mn_{1/3}Co_{1/3}O_2$ (ENAX Co, Japan, g*eneration -1*) which was produced at 1000 ^{o}C following the method described by Ohzuku et al.[1] and charged to a high voltage of 5.2 V.[10] By using electron diffraction studies, we have investigated the cationic ordering before and after long-term ageing of this oxide cathode material. based on our observation, large variations in cation ordering was indentified in the pristine material and indications for grain growth process within the examined particles (not the overall particle growth) after ageing was realized.[10] Also, this inhomogeneous cation distribution in the pristine material converted to a mixture of O3 phase and spinel phase after aging or charge to high voltage. Along with this some degree of $\sqrt{3}a_{hex}\times\sqrt{3}a_{hex}$ R30° in-plane ordering was observed in the starting material in the electron diffraction study. In our another study,[11] the commercial $LiNi_{1/3}Mn_{1/3}Co_{1/3}O_2$ (ENAX Co, Japan, *generation-2*) which was also synthesized at 1000 °C following the procedure reported elsewhere [4] and underwent 520 charge discharge cycles between 3.0 and 4.3 V, the long range ordering was detected in the starting material which was converted to the spinel phase after cycling . The mille feuille morphology was observed in the analyzed cycled particles which show the degradation of the cathode material after repeated cycling processes. To our speculation, the

synthesis procedures play an important factor to determine the microstructure of this $LiNi_{1/3}Mn_{1/3}Co_{1/3}O_2$ material. So, in the present study we want to investigate the $LiNi_{1/3}Mn_{1/3}Co_{1/3}O_2$ which is prepared by the sol- gel method at lower temperature compared to the starting material that we analyzed before in order to study the cation distribution in the stating material. Since studying thermal stability of $LiNi_{1/3}Mn_{1/3}Co_{1/3}O_2$ is another important aspect of this materials research, in next part, we analyze the cation ordering in the thermally aged products of lithium deficient material in order to understand how heat may affect the ordering of the transition metal ions in the lattice and changes the microstructure as well as particle morphology. We correlate the selected area electron diffraction studies and magnetic responses from these products to investigate the cation ordering as well as microstructural changes in these materials.

Moreover, the magnetic characterization technique is a versatile and one of the most powerful techniques to study the structural complexity of layered cathode materials.[12] The information on oxidation states of transition metal ions,[13] cation ordering,[14-15] stoichiometry of lithium ions[12] can be deduced from the magnetic data of these oxide cathode materials. Earlier, there are many reports could be found those clearly demonstrate the magnetic characterization of $LiCoO_2$ before and after lithium extraction since the lithium extraction changes the oxidation states of cobalt ions and hence, the magnetic response changes. [16-18] In one of our studies on Li_xCoO_2 the magnetic tool was used to identify its thermally decomposed products such as Co_3O_4 and $LiCo_2O_4$ (Chapter 2).[19] In our another study,[15] (Chapter 3) the Ni^{+2}/Li^{+} exchange was studied in the binary compounds $LiNi_{1-x}Mn_xO_2$ (x = 0.3,0.5,0.7) by using magnetic responses from these materials. Although there are several studies reported[13,20,14] describing the magnetic properties of the ternary $LiNi_{1/3}Mn_{1/3}Co_{1/3}O_2$ material, to our knowledge, no reports could be

found on the magnetic properties correlated to electron diffraction studies to study the cation ordering in this material and its aged products. Here we want to extend our studies on the magnetic behavior of ternary material $LiNi_{1/3}Mn_{1/3}Co_{1/3}O_2$ and also in lithium deficient material before and after ageing to study the cation ordering in these materials correlating the single crystal electron diffraction studies. In response of mixed transition material is strongly dependent on the cation ordering in the transition metal layers and small amount of Ni^{+2} ions from 3b sites when replaces the Li^+ in 3a site that generates the some degree of ferromagnetic ordering and can be detected by magnetic responses. Also, this Ni^{+2}/Li^+ exchange can be detected by the single crystal electron diffraction data where the superlattice reflection appears due to ordering in the transition metal layer.

4.2 Experimental

$LiNi_{1/3}Mn_{1/3}Co_{1/3}O_2$ was prepared by the hydroxide co-precipitation method following the modified procedure reported by Lue *et al.*[5] Briefly, stoichiometric amounts of $NiSO_4 \cdot 6H_2O$, $CoSO_4 \cdot 7H_2O$ and $MnSO_4 \cdot H_2O$ with a Ni:Co:Mn ratio of 1:1:1 were dissolved in the distilled water separately to prepare 2 M concentrated solutions. These solutions were mixed together and then stirred continuously for 1 h at 50 °C under argon atmosphere. 50 ml of aqueous NaOH and NH_4OH solution were added to get precipitates maintaining pH of 10-11. The solution was stirred in argon atmosphere for 24 h at 50 °C. Then the precipitate was filtered, washed with water and kept in oven at 50 °C overnight to dry. The obtained precursor was mixed with stoichiometric amount of $LiOH \cdot H_2O$ and thoroughly ground by a mortar. The powder was pressed into pellets and heated at 450 ^oC for 5 h followed by heated at 650 °C for 9 h. The disintegrated pellets were pressed again and calcined at 850 °C for 18 hrs and ground to obtain black $LiNi_{1/3}Mn_{1/3}Co_{1/3}O_2$ powder. Chemical delithiation was performed under argon atmosphere

at room temperature using the solution of NO_2BF_4 (source: Sigma Aldrich, assay ≥ 98%) in acetonitrile in a concentration ratio of oxide material: oxidant equal to 1:1.1. The reaction was carried out by drop wise addition of NO_2BF_4 for 90 minutes followed by additional stirring of 90 minutes to produce $Li_{1-x}Mn_{1/3}Co_{1/3}O_2$. Subsequently some portions of the delithiated powder were annealed in air at 70 °C for 30 days and 45 days.

4.3 Characterization

For the starting material and its delithiated compounds quantitative analysis of Co, Mn, Ni and Li content were carried out through Inductive Coupled Plasma Mass Spectrometry (ICP-MS). X-ray diffraction spectra (XRD) were collected with an X'pert PRO diffractometer (Panalytical) operated at 40 kV voltage and 40 mA current using Cu-Kα radiation. Silicon powder was mixed into the powders as diffraction standard. Phase determination was carried out by comparison between experimental and simulated powder diffraction spectra obtained with the software "Powder cell" and using unit cells published in literature. Magnetic measurements were performed under field cooling (FC) and zero field cooling (ZFC) using a superconducting quantum interface design (SQUID) magnetometer (MPMS-XL-7: Quantum Design) in the temperature range between T = 5 K – 300 K under magnetic field H = 10 kOe. The plot of magnetic moment and magnetic field (M-H) curves were obtained by using same instrument at T = 5 K. Transmission electron micrographs and selected area electron diffraction (SAED) patterns were obtained by using the JEOL 2010 Transmission Electron Microscope at the University of New Orleans operated at 200 kV. Experimental diffraction patterns were compared to patterns simulated with the software Desktop Microscopist.

4.4 Results and discussion

Figure 4.1 represents x-ray powder diffraction patterns of starting material along with its delithiated products before and after heat treatment at 70 °C for 30 days and 45 days. The clear splitting of (006)/(102) and (108)/(110) doublets in the starting material shows the characteristics of layered structure. The value of I_{003}/I_{104} is more than the value of 1.2 which indicates good layered structure of the starting material. According to Dahn et al.,[21] the *R*-factor ($R=(I_{102}+I_{006})/I_{101}$) indicates the hexagonal ordering in the layered cathode oxide materials, the lower the *R*- factor value the better the hexagonal ordering. The *R*-factor for the starting material was found out to be 0.391 which is significantly lower as compared to the values reported in the literature[5] that shows the good hexagonal ordering in the as synthesized material. The *c* and *a* lattice parameters are 14.135 Å and 2.84 Å, respectively, with c/a ratio of 4.97 which is in agreement with the values reported in literature.[5] All the peaks in the starting material can be well indexed with the rhombohedral symmetry with $R\bar{3}m$ space group (space group no. 166). After chemical delithiation the (003) peak shifts to the lower 2θ values resulting increasing in c lattice parameter compared to the starting material (see the inset of Figure 4.1). This is due to the induction of electrostatic

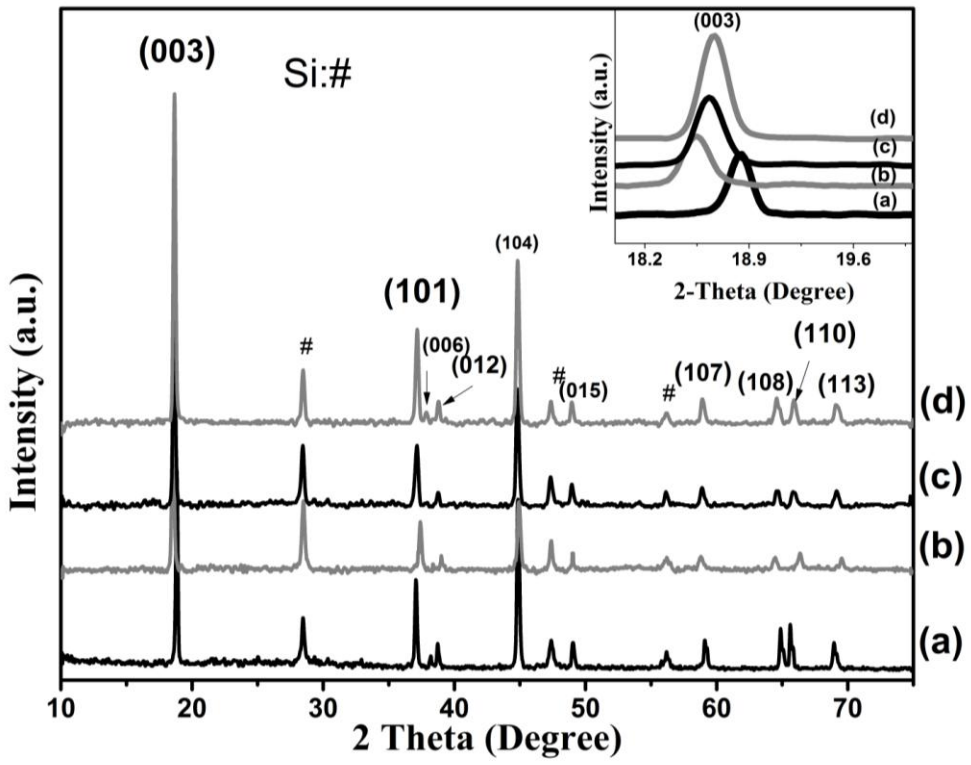

Figure 4.1 XRD of $LiNi_{1/3}Mn_{1/3}Co_{1/3}O_2$ (a) starting material, (b) delithiated material, (c) delithiated and aged at 70 °C for 30 days and (d) delithiated and aged at 70 °C for 45 days. The inset shows the shifts of (003) peaks for different materials.

repulsion among the MO_2 (M = Co, Mn, Ni) slabs along c direction of the unit cell as lithium is extracted from the parent layered structure. The XRD line spacing between (108)/(110) doublets increases after deintercalation of lithium ions. Overall, there is no phase change was observed after lithium extraction. After thermal treatment of lithium deficient (delithiated) materials, the (003) peak shifts back towards the higher angle resulting decreasing in c lattice parameter compared to the delithiated material and this tendency is seen to be increased over the time of aging process (see the inset of figure 4.1) and the line spacing between (108) and (110) decreases

after thermal treatment of lithium deficient material. Although the lattice parameters change in the materials before and after thermal aging of the lithium deficient material, the c/a ratios seem to be maintained for all the materials indicating that there is no major phase change has been occurred.

The variation of magnetic susceptibility with the temperature under filed cooling (FC) and zero filed cooling (ZFC) for starting material, delithiated materials are shown in Figure 4.2. At higher temperature region ($T \geq 100$ K), these materials show paramagnetic behavior obeying the Curie-Weiss law. The increase in magnetic susceptibility values were observed by cooling down the materials bellow 100 K. The maximum susceptibility value which was obtained at the low temperature ($T = 2$ K) region from the starting material is less than the value obtained from the lithium deficient material. This clearly suggests that the chemical delithiation process involves oxidation of Ni^{+2} (S = 1) to Ni^{+3} (S = 1/2) and/or Ni^{+4} (S = 0). To confirm the oxidation state of nickel ions after lithium extraction from the parent structures, the effective magnetic moments were calculated from the plot of inverse molar susceptibility vs. temperature in the temperature region 100 K - 300 K and those were compared with the theoretical effective magnetic moments calculated

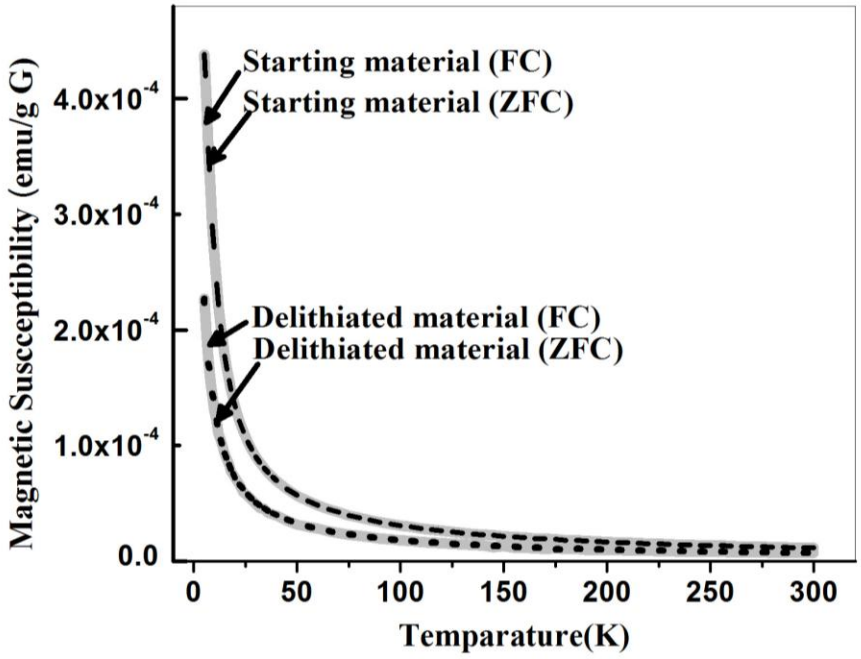

Figure 4.2 Variation of magnetic susceptibility vs. temperature of $LiNi_{1/3}Mn_{1/3}Co_{1/3}O_2$ and delithiated material $Li_{0.80}Ni_{1/3}Mn_{1/3}Co_{1/3}O_{2)}$.

by considering different oxidation states of transition metal ions. For the starting material the experimental effective magnetic moment was found to be 2.69 ± 0.01 μ_B where as, for the delithiated material it was 2.33 ± 0.10 μ_B. From the ICP measurement the actual composition of starting and lithium deficient material are found to be $Li_{1\pm02}Co_{0.33\pm02}Mn_{0.33\pm02}Ni_{0.33\pm02}O_2$ and $Li_{0.80\pm02}Co_{0.31\pm02}Mn_{0.34\pm02}Ni_{0.34\pm02}O_2$ respectively. For simplicity, while calculating for theoretical effective moments, the errors from ICP measurements were ignored. The experimental effective magnetic moment 2.69 μ_B for starting material was best explained by theoretical effective magnetic moment which was 2.77 μ_B by considering 0.33mols of Ni^{+2} (HS; S = 2), 0.33mols of Mn^{+4} (HS; S = 3) and 0.33 moles of Co^{+3} (HS; S = 0). Since delithiation process involves extraction of 20% lithium ion from the lattice, for charge compensation two processes may occur. First, the formation of 0.10 mol Ni^{+2} oxidizes to Ni^{+4} and the second one is, 0.14 mol of

Ni^{+2} oxidizes to Ni^{+3}. The theoretical effective magnetic moments were calculated by using Mn^{+4} (HS/LS), Co^{+3} (LS), Ni^{+2} (HS/LS), Ni^{+3} (HS/LS) and Ni^{+4} (HS/LS) and compared with the experimental effective magnetic moment. It has been found out that, the experimental effective magnetic moment is best described by the theoretical effective magnetic moment 1.76 μ_B which was obtained by the composition $Li_{0.80}Co_{0.33}{}^{+3(LS)}Mn_{0.34}{}^{+4(HS/LS)}$ $Ni_{0.23}{}^{+2(HS/LS)}$ $Ni_{0.10}{}^{+4(LS)}O_2$. This clearly suggests that delithiation process involves the oxidation of Ni^{+2} to Ni^{+4} ions. It is evident that, the experimental effective magnetic moment value is slightly more than the theoretical effective magnetic moment value. Eventually, there is an anticipation of some fraction of Ni^{+3} (HS/LS) is present in the lattice. The increase in the effective magnetic moment can also be due to the replacement of some amount of Li^+ with Ni^{+2} in 3a site which generates the 180° strong interlayer superexchange between Mn^{+4}(3b site)-O-Ni^{+2} (3a site) which is strong enough to generate a ferromagnetic ordering by Goodenough's rules.[22] To investigate this effect, the plot of magnetic field (H) vs. Magnetic moment (M) were collected at T = 5 K which is given in Figure 4.3. From this figure, it is observed that, the slope of the curve for the lithium deficient material is significantly different than the slope of the curve that obtained from the starting material. These observations may conclude that the saturation value for magnetic moment for the lithium deficient is more than the compared to the starting material. This indicates the presence of some degree of ferromagnetic interaction in the lithium deficient material. It is reasonable to argue that there is no hysteresis loop appears for this material to show the strong ferromagnetic ordering. Here we speculate that, in the present material the amount of Ni^{+2}-Li^+ interchange is not enough to create a strong ferromagnetic ordering despite the slope change of M-H curve. This model also supports the single crystal electron diffraction data (see below) where no particles with long range ordering was observed keeping in mind that, the interchange of Li and nickel ions in their

respective crystallographic sites creates the long range ordering in the transition metal layers. The Curie temperature calculated from the plot of inverse magnetic susceptibility vs. temperature can be related to the percentage of Ni^{+2} ions is replaced by lithium in the transition metal layer as described by Zhang *et al,*[20] The Curie temperature for the starting material and delithiated material was found to be -27K and -62K. The value of -27K for the starting material clearly confirms that the Ni^{+2}-Li^{+} interchange is very minimal. This is also in agreement with the data calculated by Zheg *et al.* According to the authors in that report, the minimum value of Curie temperature was found to be -67 K where 1.2% of Ni^{+2}-Li^{+} interchange was present in the starting material and it was increased with the increase in the interchange. In the present study, the Curie temperature obtained was lowest value suggesting the least Ni^{+2}-Li^{+} intermixing in the starting material. This is also in agreement with the single crystal selected area electron diffraction data (see below) where no long range ordering is observed. The increase in the Curie temperature in the delithiated material indicates the some percentage of Ni^{+2} is replaced Li^{+} in the transition metal layers.

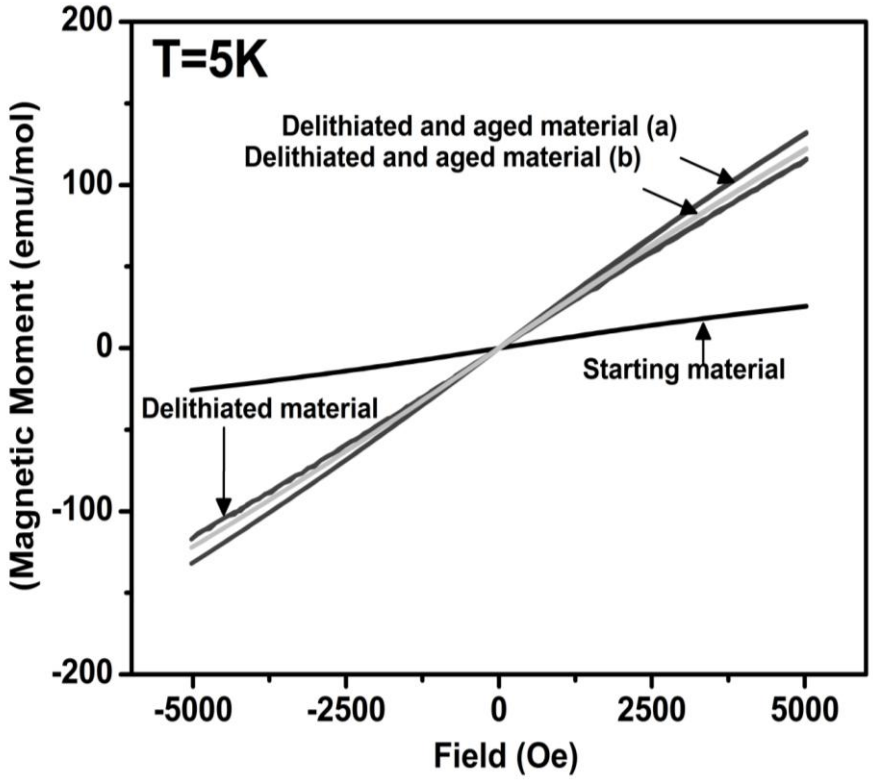

Figure 4.3 Magnetic moment (M) and magnetic field (H) of $LiNi_{1/3}Mn_{1/3}Co_{1/3}O_2$ materials

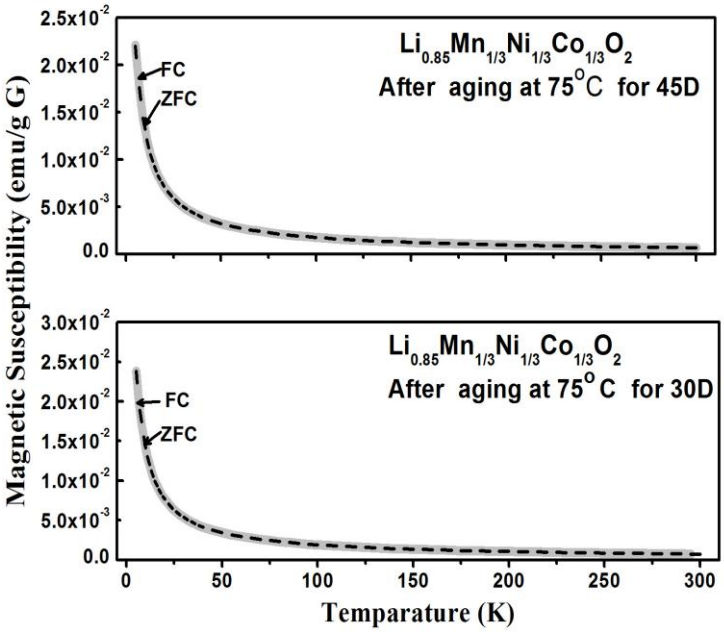

Figure 4.4 Variation of magnetic susceptibility vs. temperature of $Li_{0.80}Ni_{1/3}Mn_{1/3}Co_{1/3}O_2$ after heat treated.

The magnetic response from ternary $Li_xNi_{1/3}Mn_{1/3}Co_{1/3}O_2$ ($x \leq 1$) is different compared to the "mono" atomic system Li_xCoO_2 ($x \leq 1$) and binary $Li_yNi_{1-x}Mn_xO_2$ ($y \leq 1$; $x = 0.3, 0.5, 0.7$) that we reported previously (see chapter 2 and 3). Here we want to compare these results briefly in order to understand the magnetic responses of these oxide materials before and after lithium extraction. In case of Li_xCoO_2, the increase in magnetic susceptibility (and increase in effective magnetic moment) was observed at low temperature region ($T \leq 50$K) by continuous lithium extraction from the starting material which is apparently paramagnetic over the temperature region T = 5 K - 300 K.[19,23] Because, the lithium extraction process involves the change in oxidation state (increase in spin states) of Co^{+3}(LS, S = 0) to Co^{+4}(HS; S = 5/2 and/or LS; S = 1/2). Since there in only one magnetic ion present in the lattice, no magnetic exchange interaction is expected in the "mono" atomic Li_xCoO_2 system. However for binary and ternary

systems, the interaction between magnetic ions (Co, Mn and Ni) is expected and the nature and strength of interaction always depend upon the oxidation state and the way the magnetic cations are aligned through the oxygen anion (90 degrees or 180 degrees) based on Goodenough's rule.[22] In our study[15] of the binary system $Li_yNi_{1-x}Mn_xO_2$ ($y \leq 1$; x = 0.3, 0.5, 0.7), it was found that when the ratio of Mn ions to Ni ions are 1:1 there is a strong ferromagnetic coupling present due to the strong 180 ferromagnetic interaction between Ni^{+2} (in lithium layer)-O-Ni^{+2} (in TM layer), where as for Ni rich composition this ferromagnetic coupling was less pronounced and eventually for MN rich composition paramagnetic behavior is observed. The effective magnetic moments obtained in case of delithiated samples are less than as compared to the starting material since the lithium extraction process involves the change in oxidation state (decrease in oxidation states) of Ni^{+2} (LS/HS; S = 1) to Ni^{+3} (LS; S = 1/2) and/or Ni^{+4} (LS; S = 0). In case of ternary system $Li_xNi_{1/3}Mn_{1/3}Co_{1/3}O_2$ ($x \leq 1$), (in this present chapter), there are three transition metal ions present. The Mn^{+4} and Ni^{+2} ions are magnetically active where as Co^{+3} is not magnetically active in the fully lithiated state of the starting material. Here Ni^{+2}/Li^{+} exchange do not occur so that the compound is paramagnetic. The magnetic susceptibility of the delithiated specimen is less compared to the starting material since the lithium extraction changes the oxidation states of (decrease in oxidation states) of Ni^{+2} (LS/HS; S = 1) to Ni^{+3} (LS; S = 1/2) and/or Ni^{+4} (LS; S = 0). This is similar to binary system since in both of these systems the Ni^{+2} is electrochemically active ions unlike the Li_xCoO_2 systems where Co is electrochemically active ions.

The variation of magnetic susceptibility with the temperature under filed cooling (FC) and zero filed cooling (ZFC) for delithiated material before and after heat treatment are shown in Figure 4.4. The effective magnetic moment of delithiated material after thermal treatment at

70 °C 30 d and 70 °C 45 d were found to be 2.38 ± 0.01 μ_B and 2.35 ± 0.05 μ_B and the Curie temperature was found to be -54K and -50K respectively. The M-H curves for delithiated and aged materials follow the same trend in the slopes as in delithiated material. Over all there was no significant change in magnetic responses before and after thermal aging of lithium deficient material. This clearly suggests the better thermal stability of this material. In our earlier study[19,23] we found Co_3O_4 spinel formation after aging the $Li_{1-x}CoO_2$ product for longer time which was indentified from the magnetic data showing strong antiferromagnetic ordering at lower temperature. Here the strong antiferromagnetic ordering was not observed in the case of annealed samples. This is because; $LiNi_{1/3}Mn_{1/3}Co_{1/3}O_2$ material is more stable compared to the $LiCoO_2$ due to presence of Mn^{+4} ions present in the lattice. This prohibits the migration of magnetic ions to the tetrahedral sites which is the cause of the AFM ordering by 180° superexchange interaction among the magnetic ions.

In order to investigate the microstructural changes in these materials, single crystal selected area electron diffraction patterns were collected from randomly selected individual particles and each experimental pattern were simulated by theoretical pattern by considering O3, spinel and $\sqrt{3}a_{hex}\times\sqrt{3}a_{hex}$ R30° in-plane ordering lattice and the summary is given in Table 4.1. The explanations of these lattices can be found elsewhere[15]. 22 particles were analyzed for starting material; out of which 20 particles (90%) were indexed as O3 phase, which means the TM ions are randomly distributed over 3a sites. A small fraction of the analyzed particles (2 out of 22: 10%) showed spinel phase. The morphology of the all particles was smooth across the edge of the particle surfaces. In Figure 4.5, the bright field image of one representative particle and the

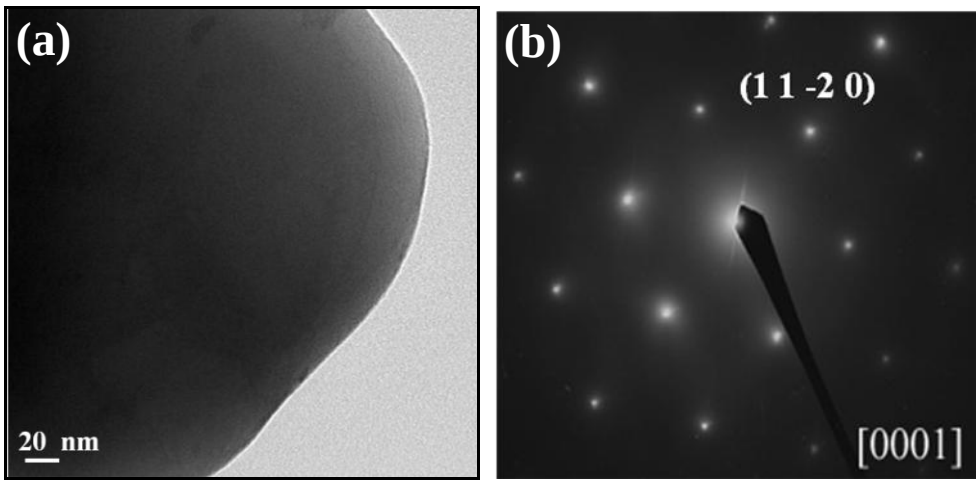

Figure 4.5 Example of (a) bright field TEM image and (b) the corresponding selected area diffraction of $LiNi_{1/3}Mn_{1/3}Co_{1/3}O_2$ starting material which shows O3 ordering.

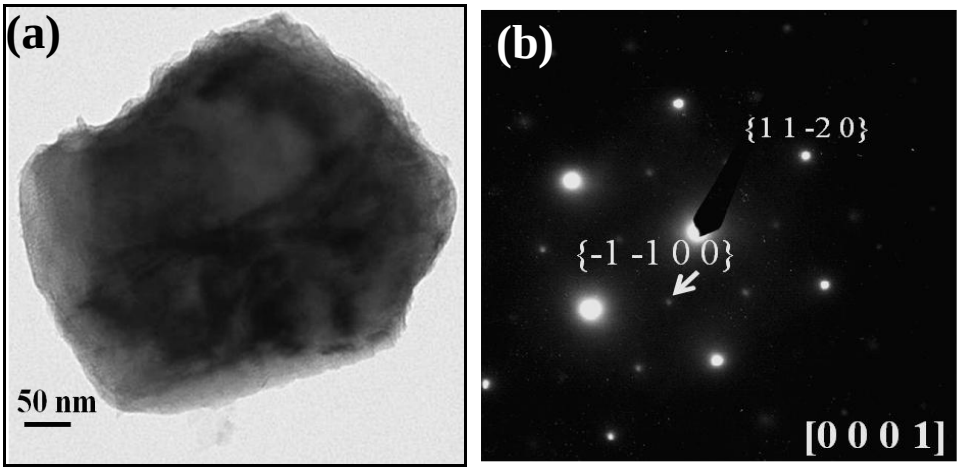

Figure 4.6: (a) Bright field TEM image showing the corroding edge and (b) the corresponding selected area electron diffraction of $Li_{0.80}Ni_{1/3}Mn_{1/3}Co_{1/3}O_2$ which shows the faint {1-100} reflection (showed by arrow).

corresponding electron diffraction showing O3 phase are given as an example. Here this has to be noted that, in-plane ordering was not observed in the starting material which clearly suggests that the transition metals are randomly oriented in the transition metal layer which would show better electrochemical activity. In our previous report,[10] some percent of particles those show the in plane

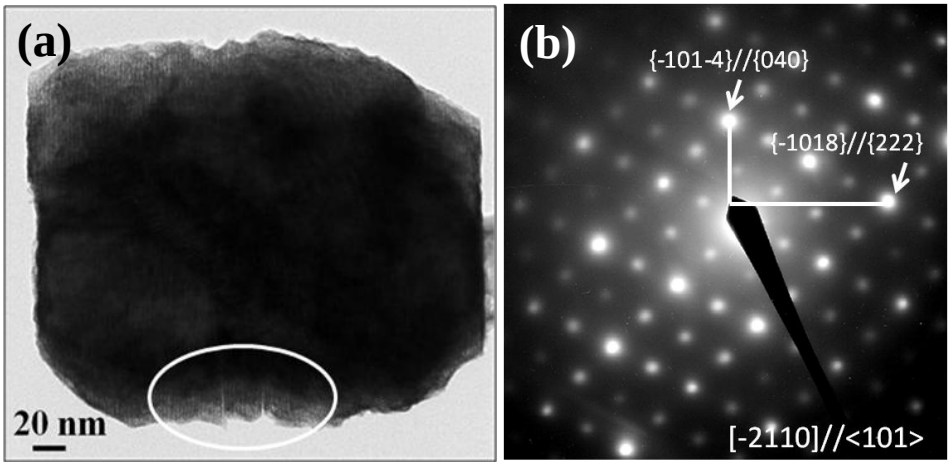

Figure 4.7 (a) Bright field TEM image showing mille feuille morphology and (b) corresponding selected area diffraction of $Li_{0.80}Ni_{1/3}Mn_{1/3}Co_{1/3}O_2$ after heat treatment for 70 °C 30 days.

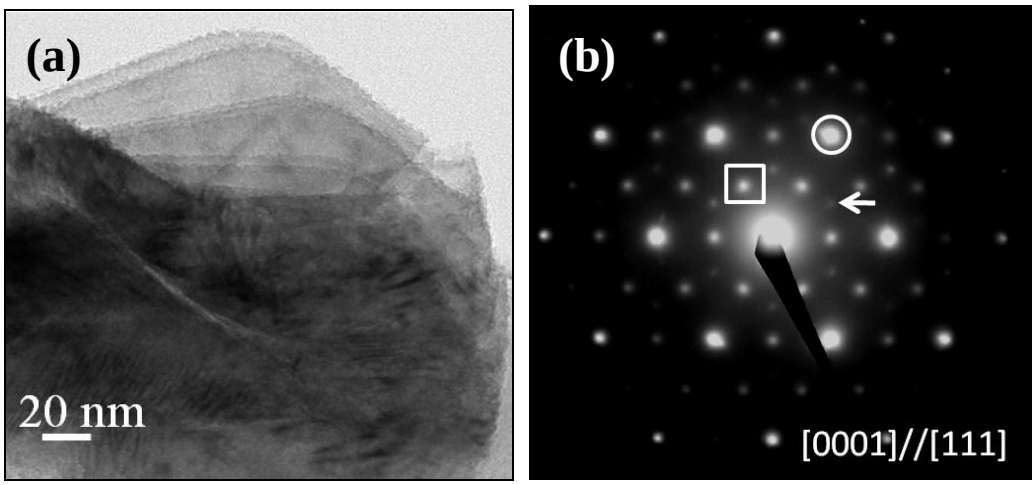

Figure 4.8 (a) Bright filed TEM image showing mille feuille morphology and (b) corresponding selected area diffraction of $Li_{0.80}Ni_{1/3}Mn_{1/3}Co_{1/3}O_2$ after heat treatment at 70 °C for 45 days. The O3 reflection (marked in a circle), spinel reflection (marked as square) and forbidden reflection (marked as arrow) are highlighted.

ordering with some degree of inhomogenety in the starting material was found out where in this present work, this ordering was not present in the examined particles. This clearly establishes the fact that the synthesis process is one of the important factors to produce homogeneous starting material of $LiNi_{1/3}Mn_{1/3}Co_{1/3}O_2$ without having the in- plane ordering that occurs due to Li^+ -Ni^{+2} interchange. Chemical extraction of lithium ion from the parent $LiNi_{1/3}Mn_{1/3}Co_{1/3}O_2$ structure produces more spinel phases in the expense of the O3 phase. Out of 20 particles analyzed 60% (12 out of 20) of particles were indexed as O3 phase whereas 20 % (4 out of 20) of the particles showed the spinel reflection. The chemical extraction did not introduce any significant microstructure changes. This observation differs from the observations in the chemically delithiated Li_xCoO_2 where the removal of small amounts of lithium results in the appearance of

strong forbidden {1-100} reflection along [0001] zone axis direction. In $LiCoO_2$, the Co-O-Co slabs glide in the (0001) plane upon lithium removal, which changes the stacking order and breaks the rhombohedral symmetry. In $LiNi_{1/3}Mn_{1/3}Co_{1/3}O_2$ very faint forbidden reflections were observed in 4 out of 22 particles (see Figure 4.6b) which clearly suggests the improved structural stability of the mixed TM compounds compared to the $LiCoO_2$. However, the morphology of the particle was changed after chemical delithiation. As chemical delithiation is etching process, some of the particles were represented with corroded edges (see the Figure 4.6a). The appearance of forbidden reflection in lithium deficient material is may be due to stacking fault of the material[10].

In case of aged materials the particles retains O3 phase. The percentage of spinel reflections were increased by the expense of the O3 phase. The material which was aged for shorter days show 40% (8 out of 20) of particles those show O3 reflection and 60% (12 out of 20) show spinel reflections. Over time, the O3 phase still remains almost similar that is 40% of the particles show O3 reflections. But, there were some percentage of particles (10%: 2 out of 20) which show the spinel reflection as well as forbidden reflections with O3 reflections (see Figure 4.8b). This is only seen for the particles which were annealed for longer time. The intensity of the forbidden reflections was brighter compared to the delithiated material. For the starting material morphology of all particles were homogeneous. After delithiation the particles were corroded at the edges and after annealed mille feuille morphology (see Figure 4.7a highlighted in circle) was obtained. In our earlier reports,[11,26] we also found the similar morphology changes for the particles obtained from cycled materials. So this type of morphology can take place during the aging of battery and do not require continuous lithium extraction. The

microstructural changes in the heat treated lithium deficient $LiNi_{1/3}Mn_{1/3}Co_{1/3}O_2$ material may trigger the capacity fade in this material and should be taken into consideration.

Table 4.1 Classification of diffraction patterns obtained from $LiNi_{1/3}Mn_{1/3}Co_{1/3}O_2$ materials

Materials	Starting	Delithiated	Delithiated and aged at70 °C for 30 days	Delithiated and aged at70 °C for 45 days
O3	20/22 (90%)	12/20 (60%)	8/20 (40%)	8/20 (40%)
Spinel	2/20 (10%)	4/20 (20 %)	12/20 (60%)	9/20 (45%)
O3+forbidden	0	4/20 (faint) (20%)		1/20 (5%)
O3+forbidden+Spinel	0	0		2/20 (10%)
Super lattice ordering	0	0		
Total no. particles	22	20	20	20

4.5 Conclusion

We investigated $LiNi_{1/3}Mn_{1/3}Co_{1/3}O_2$ material which was synthesized at 850 °C and found the absence of in-plane ordering increasing the homogeneity in the material. Lithium deficient material does not show any significant phase changes rather the morphology of the particle was

corroded. The aged product of thermal deficient material show least stable material among all the materials under investigation in this work since the prominent microstructure changes.

4.6 References

(1) T. Ohzuku; Y. Makimura *Chemistry Letters* **2001**, *7*, 6423.
(2) I. Belharouak; Y.K. Sun; J. Liu; K. Amine *Journal of Power Sources* **2003**, *123*, 247.
(3) J.W. Wen; H.J. Liu; H. Wu; C.H. Chen *Journal of Materials Science* **2007**, *42*, 7696.
(4) N. Yabuuchi; Y. Koyama; N. Nakayama; T. Ohzuku *Journal of The Electrochemical Society* **2005**, *152*, A1434.
(5) X. Luo; X. Wang; L. Liao; X. Wang; S. Gamboa; P.J. Sebastian *Journal of Power Sources* **2006**, *161*, 601.
(6) R. D. Shannon *Acta Crystallographica A.* **1976**, *32*, 756.
(7) K.-S. Lee; S.-T.Myung; J. Prakash; H.Yashiro; Y.-K.Sun *Electrochemica Acta* **2008**, *53*, 3065.
(8) P.S. Whitfield; I.J. Davidson; L.M.D. Cranswick; I.P. Swainson; P.W. Stephens *Solid State Ionics* **2005**, *176*, 463.
(9) T. Nedoseykina; S.-S. Kim; Y. Nitta *Electrochemica Acta* **2006**, *52*, 1467.
(10) H. Gabrisch; T. Yi; R. Yazami *Electrochemical and Solid-State Letter* **2008**, *11*, A119.
(11) H. Gabrisch; R. Yazami *Electrochemical and Solid-State Letter* **2010**, *13*, A88.
(12) Natasha A. Chernova; Gene M. Nolis; Fredrick O. Omenya; H. Zhou; and, Z. L.; Whittingham, M. S. *Journal of Materials Chemistry* **2011**, *DOI: 10.1039/c1jm00024a*.
(13) M.Ma; Natasha A. Chernova; Brian H. Toby; Peter Y. Zavalij; Whittingham, M. S. *Journal of Power Sources* **2007**, *165*, 517.
(14) Natasha A. Chernova; M.Ma; J. Xiao; M.S. Whittingham; J. Breger; Grey, C. P. *Chemistry of Materials* **2007**, *19*, 4682.
(15) D Mohanty; P. Paudel; H. Gabrisch *Solid State Ionics* **2010**, *181*, 914.
(16) Hertz, J. T.; Huang, Q.; McQueen, T.; Klimczuk, T.; Bos, J. W. G.; Viciu, L.; Cava, R. J. *Physical Review B* **2008**, *77*, 075119
(17) Mukai, K.; Sugiyama, J.; Ikedo, Y.; Andreica, D.; Amato, A.; Brewer, J. H.; Ansaldo, E. J.; Russo, P. L.; Chow, K. H.; Ariyoshi, K.; Ohzuku, T. *Journal of Physics and Chemistry of Solids* **2008**, *69*, 1479.
(18) Sugiyama, J.; Nozaki, H.; Brewer, J. H.; Ansaldo, E. J.; Morris, G. D.; Delmas, C. *Physical Review B* **2005**, *72*, 144424.
(19) D Mohanty; H. Gabrisch *Solid State Ionics* **2011**, *194*,41
(20) X. Zhang; A. Mauger; F.Gendron; L.Qi; H.Groult; Perriguad, L.; C.M.Julien *Electrochemical Society Transactions* **2009**, *16*, 11.
(21) J.R. Dhan; U.von Sacken; Michal, C. A. *Solid State Ionics* **1990**, *44*, 87.
(22) J.B. Goodenough *Physical Review* **1960**, *117*, 1442.
(23) D. Mohanty; H. Gabrisch *Electrochemical Society Transactions* **2009**, *19*, 25.

(24) Y. Koyama; N. Yabuuchi; I. Tanaka; H. Adachi; T. Ohzuku *Journal of the Electrochemical Society* **2004**, *151*, A1545.
(25) Y.S. Meng; G. Ceder; C.P. Grey; W.-S. Yoon; Y. Shao-Horn *Electrochemical and Solid-State Letters* **2004**, *7*, A155.
(26) H. Gabrisch; D. Mohanty *Electrochemical Society Transactions* **2009**, *16*, 1.

Chapter 5

Synthesis and ferroelectric response of cubic and spherical $LiNbO_3$ nanocrystals

Abstract

Methods have been developed for the shape-selective synthesis of ferroelectric $LiNbO_3$ nanoparticles. Decomposition of the single-source precursor, $LiNb(O\text{-}Et)_6$, in the absence of surfactants, can reproducibly lead to either cube- or sphere-like nanoparticles. X-ray diffraction shows that the $LiNbO_3$ nanoparticles are trigonal (*R*3*c*) with a = 5.145(3) Å, c = 13.867(3) Å for nanocubes and a = 5.139(3) Å, c = 13.855(3) Å for nanospheres. Sample properties were examined by piezoresponse force microscopy (PFM) and Raman where both sets of nanoparticles exhibit ferroelectricity. The longitudinal piezoelectric coefficients, d_{33}, varied with shape where the largest value was exhibited in the nanocubes (17 pm/V for the cubes versus 12 pm/V for spheres).

5.1 Introduction

For the past several decades, there has been considerable interest in the synthesis of ferroelectric materials due to their various applications in electronics, non-volatile memories, and thin film capacitors.[1-2] Lithium niobate ($LiNbO_3$, here after abbreviated as LN) is a well known ferroelectric material and due to its excellent piezoelectric and nonlinear optical properties, has been intensely studied for applications in holographic memories, second harmonic generation, and electrooptics.[3-6] Further, LN crystals show a strong room temperature spontaneous polarization of 70C/cm^2 that can persist up to the high ferroelectric transition temperature of 1483 K, making it a promising candidate for a number of other applications as sensor arrays, piezoelectric antenna arrays.[7-8]

A variety of synthetic methods have been used to prepare bulk LN including sol-gel,[9] molten salt synthesis,[10] hydrothermal methods,[11] combustion,[12] and solvothermal methods.[13] The physical properties of materials can be strongly dependent upon particle shape, size, and crystallinity as well as preparation methods and as such, there is always an interest in studying properties as a function of dimensions, morphology, and processing history. Recently nanoparticles of LN were prepared by using soft-chemical,[5] sugar-PVA matrix,[14] and solution-phase methods.[15] One report of the use of a single-source precursor, in combination with a surfactant, has been published and this method produced rod-like structures of aggregated LN nanoparticles.[15] Despite the use of these various methodologies to prepare nanoscale LN, there have been no reports demonstrating effective shape control in the production of single crystalline nanoparticles. In this chapter, we present our study on the controlled synthesis of both cube- and sphere-like LN nanoparticles via the single-source precursor, $LiNb(O\text{-}Et)_6$. Both morphologies exhibit ferroelectric response with the cubic crystal demonstrating a larger piezoamplitude.

5.2 Experimental

LN nanoparticles were readily synthesized by a simple solvothermal approach. $LiNb(O\text{-}Et)_6$ (Alfa Aesar, 5% w/v in ethanol), and 1,4-butanediol (Sigma-Aldrich, ≥ 99%), used without any further purification, were heated in an autoclave (Parr Instrument Model #4749). In typical syntheses, 3.5 mℓ (for cube-shaped particles) or 4.5 mℓ (for spherical particles) of $LiNb(O\text{-}Et)_6$ solution were placed in a ~23 mℓ Teflon sleeve along with 2.5 mℓ of 1,4-butanediol. The Teflon vessel was sealed in the stainless steel autoclave and heated in a furnace at 235 °C for 3d before being cooled down to room temperature naturally. The resulting white precipitate was collected by centrifugation, washed several times with ethanol, and dried in an oven at 70 °C.

5.3 Characterization

The X-ray diffraction (XRD) patterns of samples were collected on a Philips X-pert PW 3040 MPD X-ray powder diffractometer operated at 40kV and 40mA current with Cu Kα radiation. The transmission electron microscopy (TEM) was performed by using JEOL 2010 electron microscope at accelerating voltage of 200kV. Raman spectra were collected at room-temperature on a Thermo-Fisher DXR dispersive Raman spectrometer in a conventional backward geometry using the $\lambda = 532$ nm line with a spectral resolution of 3 cm^{-1}. The laser was focused with an X50 long-focal-length objective to a spot of about ~2 μm. Measurements were taken with the relatively low power of the incident laser beam (1 mW), to avoid the overheating of the sample from the laser source. An Asylum Research MFP-3D atomic force microscope was employed to collect piezoelectric properties in a capacitor geometry, where the conductive AFM tip and the conductive substrate are the top and bottom electrodes, respectively. Individual LN nanoparticles were imaged by applying a small ac voltage with a drive amplitude of 40 mV and a

contact resonance frequency of 270 kHz between the tip and the conductive substrate. To avoid measurement-related artefacts and to compare the piezoelectric properties of LNO nanoparticles with different shapes, all measurements were carried out with the same conductive AFM tip and laser spot on the micro-cantilever. Local amplitude and phase hysteresis loops were collected by applying 22 V ac-voltage between the tip (top electrode) and conductive substrate (bottom electrode).

5.4 Results and discussion

Figure 5.1 presents the transmission electron microscopy (TEM) images of LN nanoparticles. Both cube-shaped (a-d) and sphere- shaped (e-f) nanoparticles can be obtained by this method. The nanocubes typically have an edge length of 50-60 nm (based on ~100 particles, average length is 54.32$\pm$6.53nm), while the sphere-like particles have a sphere diameter of 40-60 nm (ave. dia ≈ 48.82$\pm$8.53nm). A high resolution TEM image (HRTEM) of a cube, along with its first Fourier transformation (FFT, see Figure 5.1d and its inset), show that it is highly crystalline with the facet oriented along (012) planes. Structural and phase characterization of LN nanoparticles were further performed by X-ray powder diffraction. From Figure 5.2, the nanoparticles can be seen to crystallize in the trigonal crystal system of the space group R3c (#161), this being the ferroelectric phase of LN. All the diffraction peaks are well matched with those from the reference (PDF file #20-0631).[16] The refined lattice parameters are in agreement with the values reported in the literature[15] and appear to be independent of nanoparticle shape (a = b = 5.145(3) Å, c = 13.867(3) Å for nanocubes; a = b = 5.139(3) Å, c = 13.855(3) Å for nanospheres). Raman spectra in the wavelength range of 100-1000 cm^{-1} are shown in Figure 5.3.

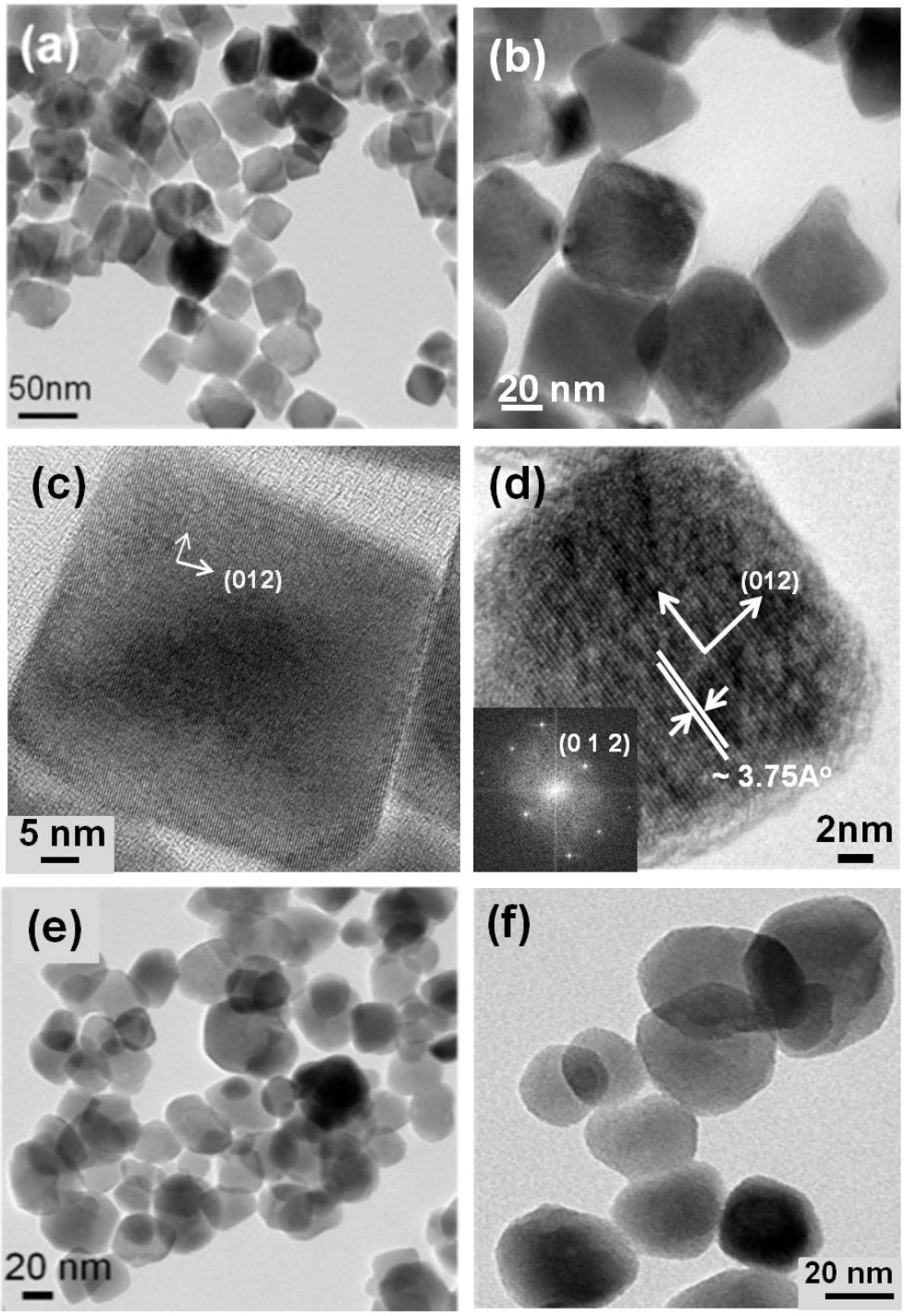

Figure 5.1 TEM images of $LiNbO_3$ nanoparticles. (a-d) cubic shaped particles (e-f) spherical shaped particles. (d) HRTEM of one single nanocube with its FFT transformation shown as inset.

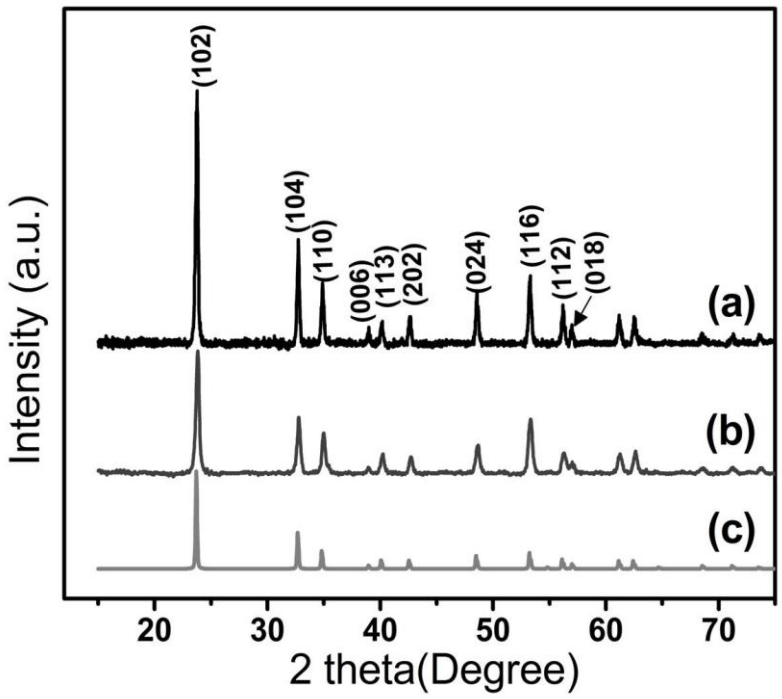

Figure 5.2 XRD patterns of $LiNbO_3$ nanoparticles (a) nanospheres and (b) nanocubes. The reference pattern (PDF file #20-0631) of $LiNbO_3$ (trigonal crystal system, space group *R*3*c*) is given in (c).

Peaks are observed at 156, 239, 370, and 433 cm^{-1} and are attributed to the E transverse optical (TO) phonon mode of LN. These peaks are also consistent with the hexagonal ferroelectric phase.[17] The fundamental A_1 TO modes were observed at 277 and 619 cm^{-1}, which also agree with values reported for ferroelectric LN single crystals.[18]

Piezoresponse force microscopy (PFM) was used to investigate the ferroelectric properties of LN nanoparticles. Standard PFM hysteresis (piezo-phase versus voltage, Figures 5.4a and 5.4c), and butterfly curves (piezo-amplitude versus voltage, Figures 5.4b and 5.4d), for both LN nanocubes and nanospheres are shown in Figure 5.4. In the phase response curves (Figures 5.4a and 5.4c), the existence of intrinsic lattice polarization in both LN nanocubes and

nanospheres and 180° switching can be observed, which indicates the existence of 180° domains in the lattice.[19] Such a domain change in voltage is generally associated with ferroelectric behavior.[20] The maximum piezo-amplitude signal measured was approximately 0.4 nm for the nanocubes and 0.25 nm for spherical nanoparticles (see Figures 5.4b and 5.4d). From the linear portion of the piezoresponse amplitude signal, the longitudinal piezoelectric coefficients, d_{33}, were calculated which are 17 pm/V for cube-like and 12 pm/V for spherical LN nanoparticles. ($A = QV_{ac}d_{33}$, where A is piezo-amplitude, Q is the quality factor which accounts for the amplitude enhancement at tip-bias resonance and V_{ac} is the voltage).

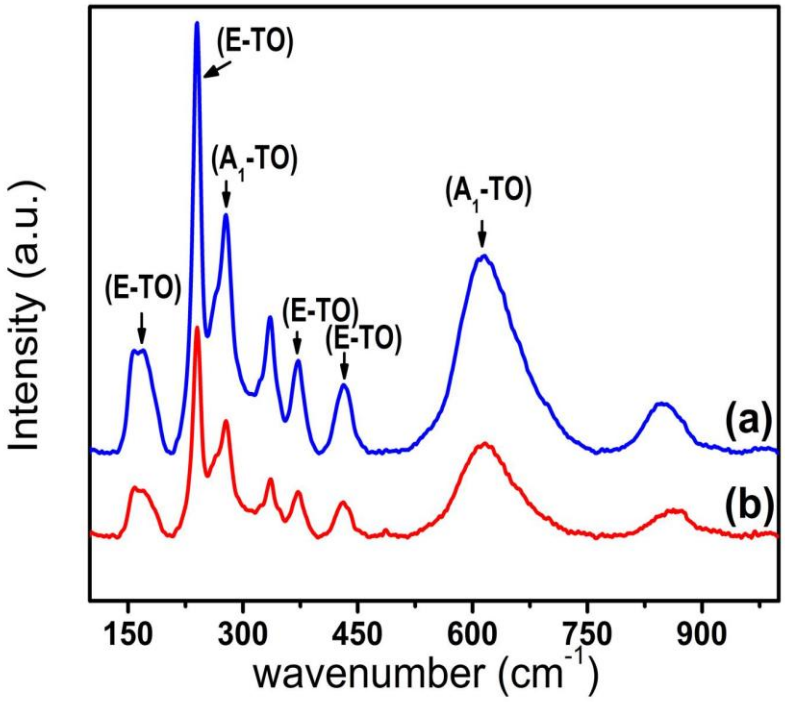

Figure 5.3 Raman spectra of $LiNbO_3$ nanoparticles. (a) nanospheres and (b) nanocubes. Transverse optical (TO) bands assignments, E TO and A_1 TO, are shown.

The solvothermal method is a versatile technique for the production of metal oxide nanoparticles at low temperatures. In this study it was found out that the particle shape could be tuned simply by changing the amount of precursor. For larger amounts of $LiNb(O\text{-}Et)_6$, the

particles attain nearly spherical shape while with smaller amounts, cubic morphologies with well-defined edges were obtained. In a solvothermal reaction, pressure is generated autogenously in the reaction vessel and is dependent on the total volume of the vessel, the filling factor of the vessel, and the molar volume of the liquids. When the volume of the liquid inside the vessel is increased, the pressure generated decreases according to the Peng-Robinson equation of state.[21] So by decreasing the amount of precursor, the pressure generated in the reaction vessel increases so as to facilitate the nucleation and growth of the particle along a particular direction, effectively favouring the cubic morphology. 1,4-butanediol also appears to be critical for this synthesis; syntheses attempted with other polyol solvents (ethylene glycol, triethylene glycol) were not successful and we found that only 1,4-butanediol leads to the production of the LN. It was also noted that three days reaction time was the minimum duration needed to form nanoparticles with definite shape. For example, the TEM image taken from a sample containing nanoparticles obtained after two days of reaction (Figure 5.5) showed only agglomerations of nanoparticles – those particles eventually grow during the aging time to produce nanocubes (Figure 5.1a). The reaction temperature (T = 235 °C) also has an impact on the stabilization of LN. If the reaction is

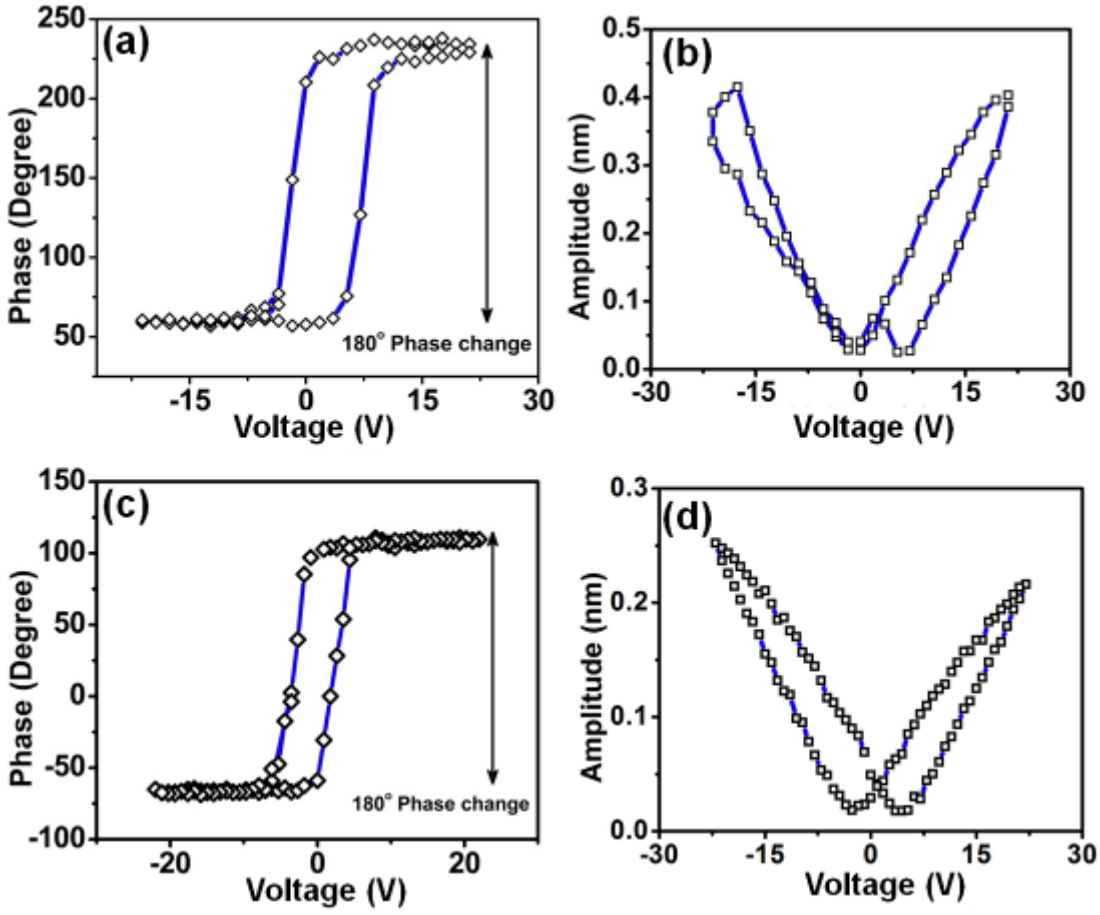

Figure 5.4 (a) Phase and (b) amplitude responses from LN nanocubes, (c) phase and (d) amplitude responses from LN nanospheres. The double arrows in (a) and (c) highlight the 180^{o} phase change with voltage.

carried out at T = 250 °C, for three days the secondary phase, $LiNb_3O_8$, is formed along with LN (Figure 5.6) and if the reaction temperature is 220 °C, then crystallization does not occur.

To investigate whether the LN nanoparticles were passivated with solvent species after their growth, FT-IR spectra were collected from neat 1,4-butanediol and then compared to that obtained from a solid sample containing LN nanocubes (Figure 5.7). No evidence of 1,4-butanediol can be observed in the spectrum. This is also consistent with the surfactant-free approach targeted in this synthesis. The possible route to produce LN nanoparticles may be thermal decomposition of $LiNb(O\text{-}et)_6$ in the presence of 1,4-butanediol. During thermal decomposition, intermolecular rearrangement occurs to introduce the metal-oxide linkage (figure 5.7I and II). Apparently removal of alcohol regulates the nucleation and growth of the particle to form seed like particles. This was confirmed by TEM image which was taken after two days of reaction shows the formation of seed like particles which eventually grow over the aging time to produce cubic shaped particles. This process is represented in Figure 5.8. So, the thermal temperature and the nature of solvent are the key to form LN nanocubes in this particular reaction.

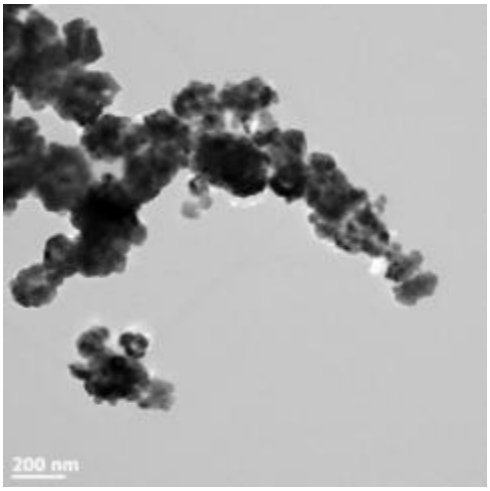

Figure 5. 5 Bright field TEM image of LN particles taken after synthesis for 2 d at 235 °C.

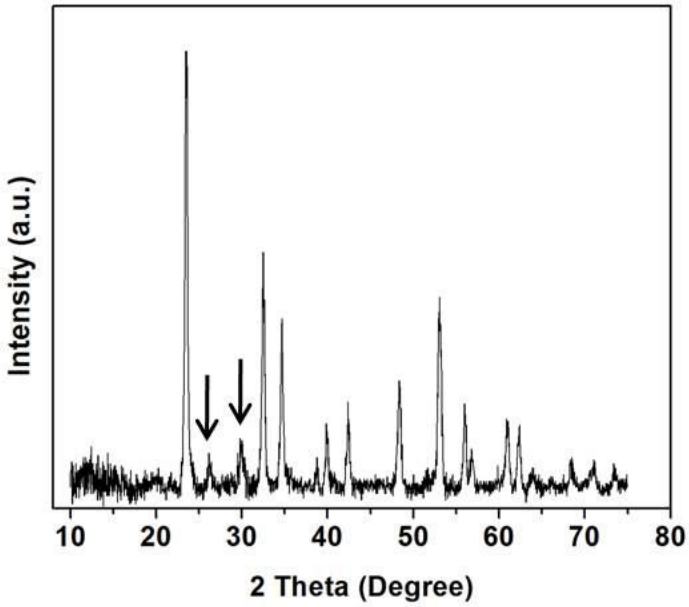

Figure 5.6 XRD pattern of LN nanoparticles after synthesis at 250 ^{o}C for 3 d shows formation of $LiNb_3O_8$ (highlighted by arrow mark).

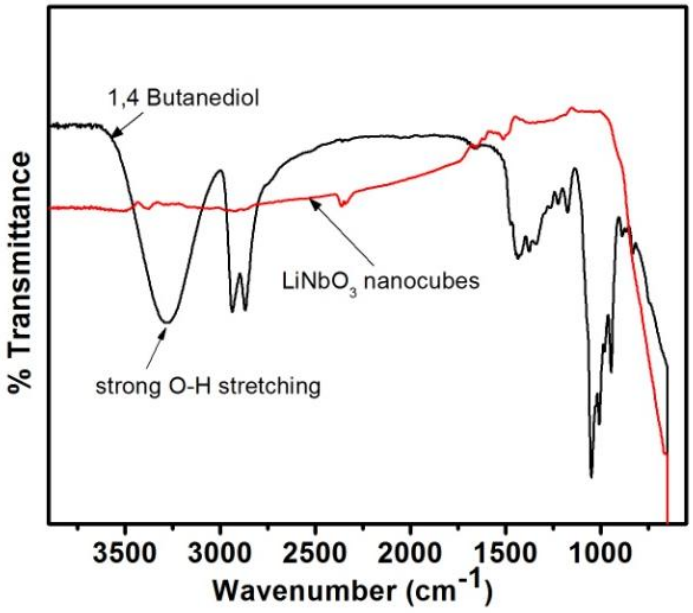

Figure 5.7 IR spectrum of LN nanocubes compared with 1,4-butanediol.

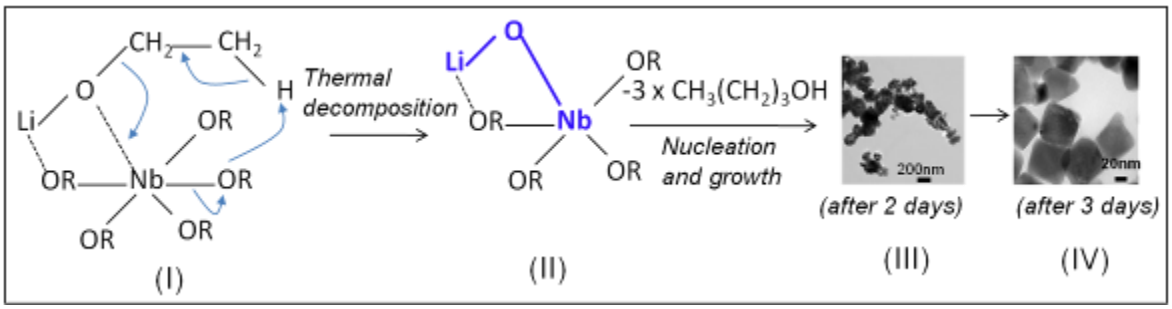

Figure 5.8 Mechanism of formation of LN nanoparticles.

LN is a ferroelectric material with a high Curie temperature (T_c = 1483 K). Below the Curie temperature, the material is rhombohedral with the *R*3*c* space group, and at higher temperature (> T_c), changes to $R\bar{3}c$ and $R\bar{3}$.[22] In the *R*3*c* ferroelectric phase, the cations are displaced along the [111] crystallographic direction, which breaks the mirror symmetry plane present in high temperature paraelectric phase to induce the spontaneous polarization in the lattice. The XRD patterns of the synthesized nanoparticles show that the materials crystallize in *R*3*c* phase, and

this was further confirmed by Raman phonon bands. The optical phonon modes obtained from Raman scattering are very sensitive to stoichiometry, strain, impurities as well as the crystal system of the materials[17]. The phonon modes observed for the LN cube-shaped nanoparticles are very similar to those of the spherical nanoparticles both in terms of position and relative intensity (Figure 5.3). The characteristic phonon peaks convincingly suggest that the ferroelectric phase (*R*3*c*) is stable in these nanoparticles,[17] results which are consistent with the PFM response curves. Close examination of the local piezoelectric response in individual nanoparticles evidenced that the displacement observed in nanocubes is slightly higher than that measured in nanospheres. This difference could be attributed to a greater crystallinity in nanocubes in tandem with the presence of better-defined facets in nanocubes than in spherical nanoparticles.[23] This is consistent with previous studies where researchers found that piezoelectric properties of nanostructured materials can depend on the crystallite size,[23] crystal orientation,[24] and geometry.[25,26]

5.5 Conclusions

Lithium niobate nanoparticles with different morphologies were synthesized under solvothermal conditions by a simple surfactant-free route using a single-source precursor. The shapes of the nanoparticles, nanocubes versus nanospheres, were tuned by simply changing the concentration of the precursor. Both sets of particles exhibit polarization switching at room temperature with static d_{33} coefficient values of 17 pm/V for cube-like and 12 pm/V for spherical LN nanoparticles. Work is ongoing to study ferroelectricity in these nanostructures, including the stability of the ferroelectric phase and the kinetics of the local polarization switching in individual nanocrystals. With controlled size and shape and predictable ferroelectric properties, these nanostructures will be attractive as building blocks for the design of complex structures,

such as in multiferroic nanoparticulate composites.

5.6 References

(1) Hennings, D.; Klee, M.; Waser, R. *Adv. Mater.* **1991**, *3*, 334-340.
(2) Zhang, Z. B.; Sun, X. Z.; Dresselhaus, M. S.; Ying, J. Y.; Heremans, J. *Phys. Rev. B* **2000**, *61*, 4850-4861.
(3) Guarino, A.; Poberaj, G.; Rezzonico, D.; Degl'Innocenti, R.; Gunter, P. *Nat. Photonics* **2007**, *1*, 407-410.
(4) Xue, D. F.; He, X. K. *Phys. Rev. B* **2006**, *73*, 64113.
(5) Niederberger, M.; Pinna, N.; Polleux, J.; Antonietti, M. *Angew. Chem.-Int. Edit.* **2004**, *43*, 2270-2273.
(6) Xue, D. F.; Kitamura, K. *J. Cryst. Growth* **2003**, *249*, 507-513.
(7) Inbar, I.; Cohen, R. E. *Phys. Rev. B* **1996**, *53*, 1193-1204.
(8) Zhang, D. L.; Zhang, W. J.; Zhuang, Y. R.; Pun, E. Y. B. *Cryst. Growth Des.* **2007**, *7*, 1541-1546.
(9) Pitcher, M. W.; He, Y. N.; Bianconi, P. A. *Mater. Chem. Phys.* **2005**, *90*, 57-61.
(10) Afanasiev, P. *Mater. Lett.* **1998**, *34*, 253-256.
(11) Dey, D.; Kakihana, M. *J. Ceram. Soc. Jpn.* **2004**, *112*, 368-372.
(12) Liu, M. N.; Xue, D. F.; Luo, C. *J. Am. Ceram. Soc.* **2006**, *89*, 1551-1556.
(13) Liu, M. N.; Xue, D. F. *Mater. Lett.* **2005**, *59*, 2908-2910.
(14) Wohlrab, S.; Weiss, M.; Du, H. C.; Kaskel, S. *Chem. Mat.* **2006**, *18*, 4227-4230.
(15) Wood, B. D.; Mocanu, V.; Gates, B. D. *Adv. Mater.* **2008**, *20*, 4552-4556.
(16) *National Bureau of Standards (U.S.) Monograph* **1968**, *6*, 22.
(17) Barker, A. S.; Loudon, R. *Physical Review* **1967**, *158*, 433.
(18) Schaufele, R. F.; Weber, M. J. *Physical Review* **1966**, *152*, 705.
(19) Kalinin, S. V.; Morozovska, A. N.; Chen, L. Q.; Rodriguez, B. J. *Rep. Prog. Phys.* **2010**, *73*, 056502.
(20) Jesse, S.; Baddorf, A. P.; Kalinin, S. V. *Appl. Phys. Lett.* **2006**, *88*, 062908.
(21) Rajamathi, M.; Seshadri, R. *Current Opinion in Solid State and Materials Science* **2002**, *6*, 337-345.
(22) Abrahams, C.; Levinstein, H. J.; Reddy, J. M. *Journal of Physics and Chemistry of Solids* **1966**, *27*, 1019.
(23) Rudiger, A.; Schneller, T.; Roelofs, A.; Tiedke, S.; Schmitz, T.; Waser, R. *Appl. Phys. A-Mater. Sci. Process.* **2005**, *80*, 1247-1255.
(24) Cheng, Z. X.; Kannan, C. V.; Ozawa, K.; Kimura, H.; Wang, X. L. *Appl. Phys. Lett.* **2006**, *89*, 032901
(25) Wang, Z. Y.; Hu, J.; Suryavanshi, A. P.; Yum, K.; Yu, M. F. *Nano Lett.* **2007**, *7*, 2966-2969.
(26) Zheng, Y.; Woo, C. H.; Wang, B. *J. Phys.-Condes. Matter* **2008**, *20*, 135216.

Chapter 6

Conclusions

The basic objective of this work was to identify structural instabilities and study the microstructure of layered cathode materials upon lithium deintercalation (charging) to obtain a deeper understanding of the change in crystal structure and particle morphology of these materials before and after charging. Heating experiments of the lithium deficient phases were performed to investigate thermal stability. Powder X-ray diffraction, single crystal electron diffraction, and imaging techniques in the transmission electron microscope were used to study the microstructure of these materials whereas magnetic measurements were used to investigate variations in cation ordering for $LiMO_2$ (M = Co, Mn, Ni) cathode materials.

Different spinels phases, such as $LiCo_2O_4$ and Co_3O_4, were identified by using magnetic measurements and XRD and thereby it was possible to follow the decomposition of $Li_{1-x}CoO_2$ cathode material. Magnetic studies of Li_xCoO_2 (x = 0.98, 0.76, 0.55) were conducted before and after heat treatment under zero field (ZFC) and field cooling (FC) to elucidate the nature and pathways of the spinel phase that forms in addition to the layered $LiCoO_2$ phase. The results showed that the $LiCo_2O_4$ phase is formed before the end product Co_3O_4 is observed. Prior to heat treatment paramagnetic behavior was observed without indication of magnetic ordering down to 5 K. Heat treatment of delithiated materials progressively changed the magnetic nature within the compounds. After short term heat treatment of Li_xCoO_2, spin glass-like or geometrically frustrated behavior was observed that suggested the formation of metastable spinel phase $LiCo_2O_4$ in the lattice. After long-term annealing, pronounced strong antiferromagnetic (AFM) ordering was observed which was in agreement with the formation of Co_3O_4. At the same time an increase in the effective magnetic moment occurred with annealing time due to introduction

of Co^{+2} ions resulting from formation of Co_3O_4 phase.

Homogeneous $LiNi_{1/3}Mn_{1/3}Co_{1/3}O_2$ was synthesized at 850 °C to avoid the cation ordering in the starting material. Also, we studied the behavior of lithium deficient products of this material before and after thermal ageing with respect to time. Our result showed that the change in morphology of the particles in long term aged product including the significant microstructure changes. The lithium deficient material did not show any prominent phase changes, rather the morphology of the particle was corroded. The aged products of thermal deficient material show prominent microstructure changes among all the materials under investigation here. From magnetic data and XRD data, no cubic spinel phase were detected in this material even after long term ageing; leading to the important conclusion that $LiNi_{1/3}Mn_{1/3}Co_{1/3}O_2$ is more stable compared to $LiCoO_2$. Our speculation is that, the morphology changes in the lithium deficient material and aged products may be what leads to the capacity fading in this material.

In another project we have performed microstructural studies on a series of $Li[Ni_{1-x}Mn_x]O_2$ compounds where the oxidation states and arrangement of transition metal ions are characterized by SQUID magnetometry and single crystal electron diffraction, respectively. Compounds in the series $LiNi_{1-x}Mn_xO_2$ (x = 0.3, 0.5, 0.7) were synthesized in the layered structure (they form in different particle morphology) and characterized by powder and single crystal diffraction methods as well as magnetic measurements. Superstructure peaks were observed in the manganese-rich phase. Comparison between theoretical models and experimentally determined effective magnetic moments indicates that Ni and Mn ions take on +2 and +4 oxidation states when present in a 1:1 ratio. In Ni-rich or Mn-rich compounds the extra Ni or Mn ions are observed in +3 oxidation states. Upon Li extraction, Ni^{2+} is oxidized to Ni^{4+} in

$LiNi_{0.5}Mn_{0.5}O_2$. From SAED studies, exchange between Li^+ and Ni^{+2} is observed that results in in-plane $\sqrt{3}a_{hex}\times\sqrt{3}a_{hex}$ R30° long range order in $LiNi_{0.5}Mn_{0.5}O_2$ and in the Mn-rich compound but not in the Ni-rich compound. However, the observed magnetic frustration in $LiNi_{0.7}Mn_{0.3}O_2$ indicates that Ni^{+2} ions are present in the Li layer here as well by applying Goodenough rules of magnetic interaction among the transition metal ions. After Li-extraction, the magnetic frustration disappeared in the Ni-rich phase while the percentage of long range order decreased in $LiNi_{0.5}Mn_{0.5}O_2$ and in the Mn-rich phase indicating that Li has been extracted predominantly from the transition metal layer. This project reveals the correlation of magnetic properties with the selected area electron diffraction studies in order to interpret the ordering among the transition metal ions in binary oxide cathode materials.

Shape dependent ferroelectric properties of $LiNbO_3$ nanoparticles were studied. Nanoparticles with different morphologies were synthesized under solvothermal conditions by a simple surfactant-free route using $LiNb(O\text{-}Et)_6$ as a single-source precursor. The shapes of the nanoparticles, nanocubes versus nanospheres, were tuned by simply changing the concentration of the precursor. X-ray diffraction showed that the $LiNbO_3$ nanoparticles were trigonal (*R*3*c*) with a = 5.145(3) Å, c = 13.867(3) Å for nanocubes and a = 5.139(3) Å, c = 13.855(3) Å for nanospheres. Ferroelectric properties for these nanoparticles were confirmed by piezoresponse force microscopy (PFM). Both sets of particles exhibited polarization switching at room temperature with static d_{33} coefficient values of 17 pm/V for cube-like and 12 pm/V for spherical LN nanoparticles. With controlled size and shape and predictable ferroelectric properties, these nanostructures will be attractive as building blocks for the design of complex structures, such as in multiferroic nanoparticulate composites.

Appendix 1
Synthesis and Ferroelectric properties of $LiNbO_3$ hollow spheres.

This project involved the exploration of novel synthetic techniques to produce ferroelectric $LiNbO_3$ hollow spheres. The spheres were synthesized by a solvothermal method. The detailed synthesis procedure is given as follows.

For the synthesis of $LiNbO_3$ hollow spheres 2 mmol of lithium acetate dehydrate and 2 mmol of niobium ethoxide and 9 ml 1,4-butanediol were placed in a 23 ml of Teflon vessel and 2.5 mL of 1,4 butanediol was added as a solvent. The Teflon vessel was sealed in an autoclave (Parr Instrument Model #4749) and heated in a furnace at 220 °C for 5 days and subsequently cooled down to the room temperature naturally. The white precipitates were collected and washed with ethanol several times followed by drying in an oven at 70 °C overnight to get the white powder of lithium niobate.

The FESEM and TEM images for hollow spheres are presented in Figure A1.1a and A1.1b respectively. The hollow nature of the all particles can be confirmed from TEM image, as the core of the spheres is brighter as compared to outer shell. From these images it was found that the diameters of hollow spheres were about 1.5 μm. From TEM images it can be seen that the hollow spheres are formed by nanoparticles of different sizes. The selected area electron diffraction (Figure A1.2b) taken from the corresponding particle (Figure A1.2a) shows the spot pattern corresponding to rhombohedral symmetry. The present work deals with surfactant free synthesis of LN hollow spheres which make the better accessibility of the surface of hollow spheres to enhance the property of these materials. The formation of LN phases most likely proceeds by ester elimination which occurs between acetate ligand of lithium acetate and

ethoxide ligand of niobium ethoxide to form the oxo-ligand. The ferroelectric response of $LiNbO_3$ hollow spheres is confirmed by PFM (Figure A1.3) and Raman measurement (Figure A1.4). In PFM, the hysteresis behavior of phase vs. amplitude curve shows that the materials have ferroelectric behavior. The maximum amplitude obtained for these materials is 2.5 nm (Figure A1.5). In the Raman measurement all the TO modes corresponds to the R3c phase of $LiNbO_3$ which is ferroelectric.

.

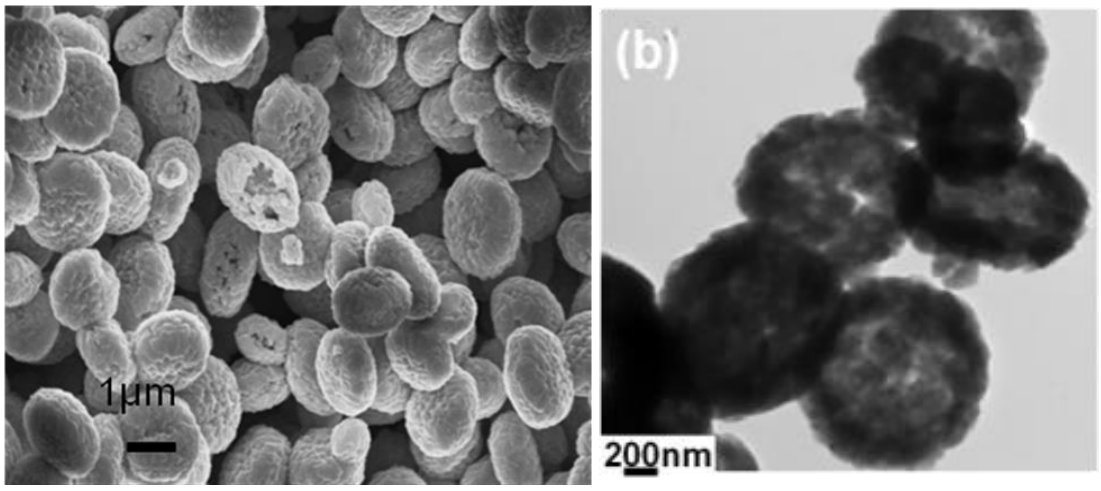

Figure A1.1 (a) FESEM image and (b) TEM image of $LiNbO_3$ hollow spheres.

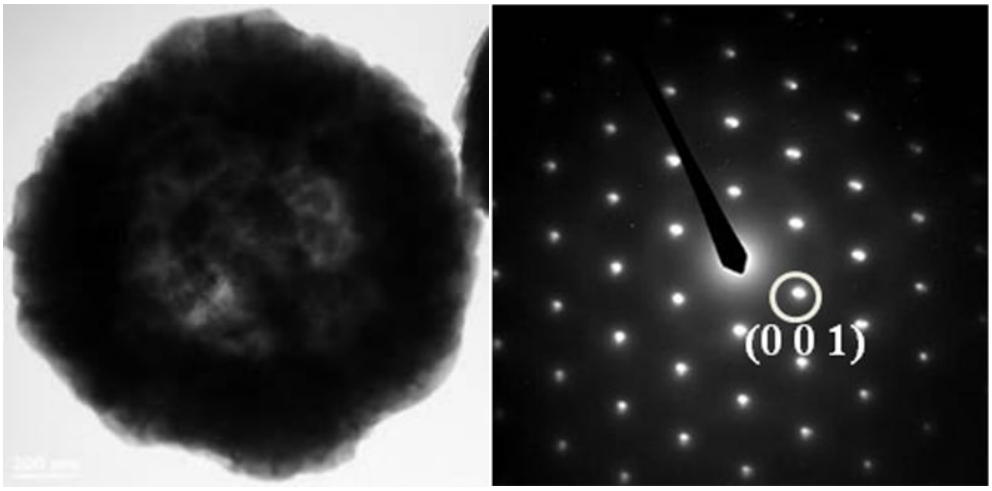

Figure A1.2 (a) TEM image and (b) corresponding SAED pattern of $LiNbO_3$ hollow spheres.

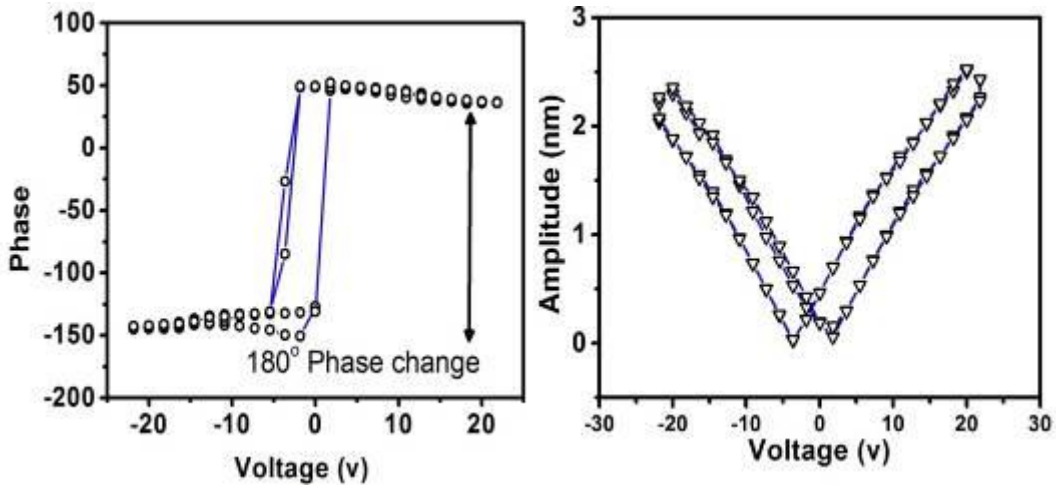

Figure A1.3 (a) Phase response and (b) amplitude response of $LiNbO_3$ hollow sphere to the applied voltage in PFM measurement.

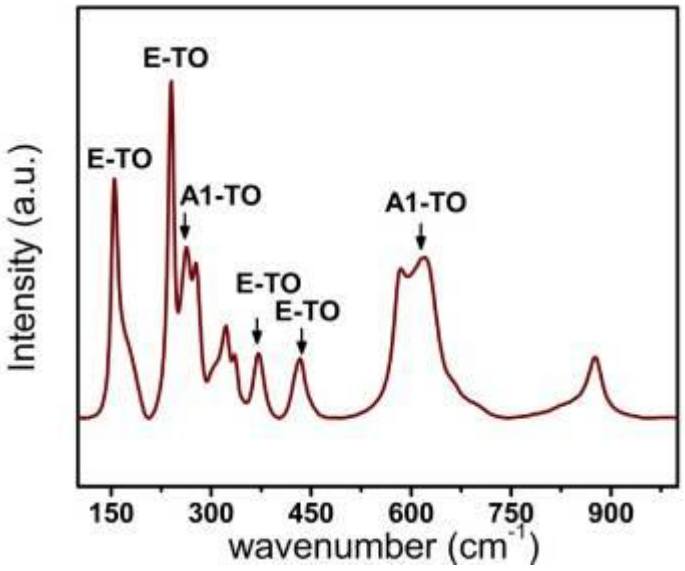

Figure A1.4 Raman measurements of $LiNbO_3$ hollow spheres.

Vita

The author was born in Cuttack, Orissa District, India in July, 1982. After finishing his early college career in 1999 from “Rayagada College”, Orissa, India, he started studying Chemistry. He obtained his Bachelor of Science (B.Sc.) and Masters of Science (M.Sc.) in the year of 2002 and 2005 respectively from Berhampur University, Orissa, India. During his M.Sc., he chose “Materials Science” as special paper. Then he entered to Pondicherry University, India as a “research fellow” in Dr. Bidhu Bhushan Das’s laboratory. There he devoted his time (2005-2007) to study the structure- property-relationships in nanocomposite materials. In the fall of 2007, he came to University of New Orleans and joined the PhD program in Chemistry under the direction of Dr. Heike B. Gabrisch and latter on, he joined Prof. John B. Wiley’s research group in spring of 2010. During his study in the University of New Orleans, he has also received his MS degree in Chemistry in the spring of 2011.